

AD-A093 881

MASSACHUSETTS INST OF TECH CAMBRIDGE DEPT OF AERONAUTICS P/O 7/4  
THE INTERACTION OF MONATOMIC AND DIATOMIC MOLECULES WITH SOLID --ETC(U)  
NOV 80 D D DREYFUSS, L TRILLING, H Y WACHMAN P44620-76-C-0036

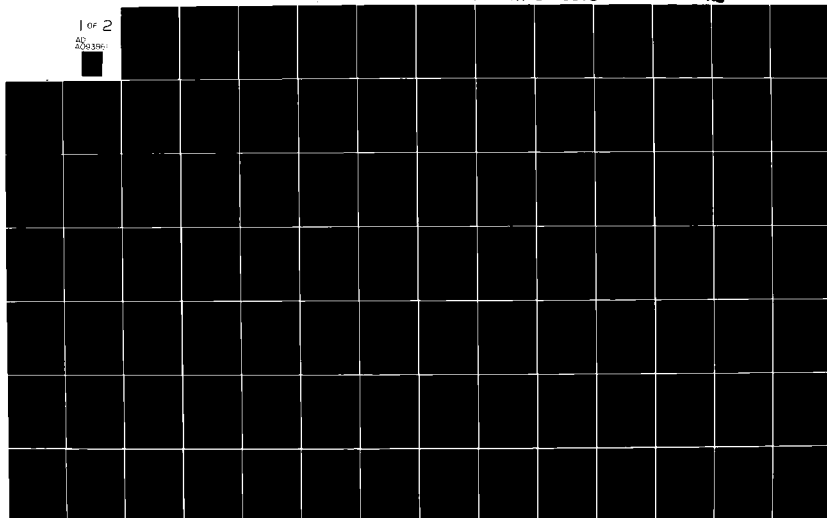
UNCLASSIFIED

AFOSR-TR-80-1365

NL

1 of 2

200 396



AD A093881

**AFOSR-TR-80-1365**

AFOSR-TR-80-

**LEVEL**

AUG 27 84

THE INTERACTION OF MONATOMIC AND DIATOMIC  
MOLECULES WITH SOLID SURFACES:

THE STRUCTURE OF WATER CLUSTER BEAMS  
AND THEIR SCATTERING FROM SURFACES,

MASSACHUSETTS INSTITUTE OF TECHNOLOGY  
DEPARTMENT OF AERONAUTICS AND ASTRONAUTICS  
CAMBRIDGE, MASSACHUSETTS 02139

NOVEMBER 1980

Final Report for Period of October 1978 to 30 September 1980

Approved for public release; distribution unlimited

Prepared for

AIR FORCE OFFICE OF SCIENTIFIC RESEARCH  
AIR FORCE SYSTEMS COMMAND  
BOLLING AIR FORCE BASE, D C 20332

DDC FILE COPY.

81 1 16 016

UNCLASSIFIED

SECURITY CLASSIFICATION OF THIS PAGE (When Data Entered)

| REPORT DOCUMENTATION PAGE  |  | READ INSTRUCTIONS<br>BEFORE COMPLETING FORM   |
|--|--|---|
| 1. REPORT NUMBER<br><b>AFOSR-TR- 90 - 1365</b>   | 2. GOVT ACCESSION NO.<br><b>AD-A693881</b> | 3. RECIPIENT'S CATALOG NUMBER   |
| 4. TITLE (and Subtitle)<br><b>THE INTERACTION OF MONATOMIC AND DIATOMIC MOLECULES WITH SOLID SURFACES: The Structure of Water Cluster Beams and their Scattering from Surfaces</b>   |  | 5. TYPE OF REPORT & PERIOD COVERED<br><b>FINAL</b><br><b>1 Oct 78 - 30 Sep 80</b>             |
| 7. AUTHOR(s)<br><b>DAVID D DREYFUSS</b><br><b>LEON TRILLING</b><br><b>HAROLD Y WACHMAN</b>   |  | 6. PERFORMING ORG. REPORT NUMBER  |
| 9. PERFORMING ORGANIZATION NAME AND ADDRESS<br><b>MASSACHUSETTS INSTITUTE OF TECHNOLOGY</b><br><b>DEPARTMENT OF AERONAUTICS &amp; ASTRONAUTICS</b><br><b>CAMBRIDGE, MA 02139</b>   |  | 8. CONTRACT OR GRANT NUMBER(s)<br><b>✓ F44620-76-C-0036</b>                                   |
| 11. CONTROLLING OFFICE NAME AND ADDRESS<br><b>AIR FORCE OFFICE OF SCIENTIFIC RESEARCH / NA</b><br><b>BLDG 410</b><br><b>BOLLING AIR FORCE BASE, D C 20332</b>  |  | 10. PROGRAM ELEMENT, PROJECT, TASK AREA & WORK UNIT NUMBERS<br><b>2307A3</b><br><b>61102F</b> |
| 14. MONITORING AGENCY NAME & ADDRESS (if different from Controlling Office)  |  | 12. REPORT DATE<br><b>November 1980</b>   |
|  |  | 13. NUMBER OF PAGES<br><b>182</b>   |
|  |  | 15. SECURITY CLASS. (of this report)<br><b>UNCLASSIFIED</b>                                   |
|  |  | 15a. DECLASSIFICATION/DOWNGRADING SCHEDULE  |
| 16. DISTRIBUTION STATEMENT (of this Report)<br><br><b>Approved for public release; distribution unlimited.</b>   |  |   |
| 17. DISTRIBUTION STATEMENT (of the abstract entered in Block 20, if different from Report)   |  |   |
| 18. SUPPLEMENTARY NOTES  |  |   |
| 19. KEY WORDS (Continue on reverse side if necessary and identify by block number)<br><b>MONATOMIC MOLECULES                      SCATTERING</b><br><b>DIATOMIC MOLECULES                      TIME-OF-FLIGHT</b><br><b>SOLID SURFACES</b><br><b>CLUSTERS</b><br><b>NUCLEATION</b>   |  |   |
| 20. ABSTRACT (Continue on reverse side if necessary and identify by block number)<br><b>An experimental study of homogeneous and heterogeneous nucleation was conducted, using molecular beam techniques: mass spectrometry and time-of-flight velocity spectrometry, with and without mass filtering. Both the clustered beam itself and the scattering of the clusters from surfaces were studied. The beam was found to consist of a broad spectrum of clusters all having approximately the same velocity distribution. Small clusters were found to have a binding energy much less than that of bulk ice. Measurements of a beam scattered from a surface using a time-of-flight velocity spectrometer show four distinct patterns. These are:</b> |  |   |

DD FORM 1473  
1 JAN 73

UNCLASSIFIED

SECURITY CLASSIFICATION OF THIS PAGE (When Data Entered)

UNCLASSIFIED

SECURITY CLASSIFICATION OF THIS PAGE(When Data Entered)

(1) a diffuse scattering channel (monomers, Maxwellian/cosine at the target temperature), (2) a direct inelastic channel for monomers characterized by a small loss of incident velocity with a broad spatial distribution peaked at the tangent for all incident angles,  $\theta_i$ , (3) a well-defined specular directed lobe ( $\theta_s = \theta_i > 50^\circ$ ) with particle velocity much slower than (1) or (2) and a velocity distribution narrower than a stationary Maxwellian, and (4) another slow peak with a slightly broader velocity distribution into a sharp intensity peak near the tangent for all  $\theta_i > 50^\circ$ . The amplitude of the specularly directed slow peak (3) appears to give a sensitive indication of surface coverage.

|                    |  |
|--------------------|--|
| Accession For      |  |
| NTIS GTR           | <input checked="checked" type="checkbox"/> |
| DTIC F             | <input type="checkbox"/>                   |
| Unannounced        | <input type="checkbox"/>                   |
| Justification      |  |
| By                 |  |
| Distribution       |  |
| Availability Codes |  |
| Dist               | Special                                    |
| A                  |  |

UNCLASSIFIED

SECURITY CLASSIFICATION OF THIS PAGE(When Data Entered)

## FOREWORD

This report was prepared by the Massachusetts Institute of Technology Department of Aeronautics and Astronautics, for the Air Force Office of Scientific Research, AFSC, under contract F44620-76-C-0036.

The report describes the research performed during the period October 1, 1978 to September 30, 1980, under the supervision of Profs. Harold Y. Wachman and Leon Trilling, co-principal investigators.

AIR FORCE OFFICE OF SCIENTIFIC RESEARCH (AFSC)  
NOTICE OF TRANSMITTAL TO DDC  
This technical report has been reviewed and is  
approved for public release IAW AFR 190-12 (7b).  
Distribution is unlimited.  
A. D. BLOSE  
Technical Information Officer

# TABLE OF CONTENTS

| Section   | Page |
|---|------|
| I INTRODUCTION  | 1    |
| 1.1 Ice Nucleation from a Molecular Point of View           | 2    |
| 1.1.1 Theoretical Work                                      | 2    |
| 1.1.2 Experimental Work                                     | 4    |
| 1.2 Condensation in Beams                                   | 5    |
| 1.3 Cluster Scattering                                      | 7    |
| II EXPERIMENTAL APPARATUS AND DATA HANDLING TECHNIQUES      | 9    |
| 2.1 Primary Vacuum Facilities                               | 9    |
| 2.2 Source Systems  | 9    |
| 2.3 Targets   | 14   |
| 2.3.1 Target Mount  | 14   |
| 2.3.2 Targets   | 15   |
| 2.4 Detection Equipment                                     | 18   |
| 2.4.1 Velocity Spectrometer                                 | 18   |
| 2.4.2 Stagnation Gauge                                      | 19   |
| 2.4.3 Mass Spectrometer                                     | 19   |
| 2.5 Time-of-Flight Signal Processing                        | 20   |
| 2.6 Software  | 22   |
| III DATA  | 24   |
| 3.1 Calibrations and Elimination of Artifacts               | 24   |
| 3.1.1 Mass Spectrometer                                     | 24   |
| 3.1.2 Time-of-Flight Apparatus without Mass-Filtering       | 26   |
| 3.1.3 Time-of-Flight Apparatus with Mass-Filtering          | 30   |
| 3.2 Source Studies  | 33   |
| 3.2.1 Argon   | 34   |
| 3.2.2 Water - General Characteristics and Velocity Analysis | 34   |
| 3.2.3 Mass Analysis   | 35   |
| 3.2.4 Mass-Filtered Velocity Analysis                       | 37   |
| 3.3 Evaporation   | 40   |

| Section   | Page |
|---|------|
| 3.4 Scattering Data   | 43   |
| 3.4.1 Early Studies   | 43   |
| 3.4.2 The Water Scattering Data   | 44   |
| 3.4.2.1 Experimental Conditions Tested  | 44   |
| 3.4.2.2 Features Observed   | 45   |
| 3.4.2.2.1 The Maxwellian Peak   | 46   |
| 3.4.2.2.2 The Fast Peak   | 48   |
| 3.4.2.2.3 The Specularly Directed<br>Slow Peak  | 49   |
| 3.4.2.2.4 The Non-Specular Slow Peak  | 52   |
| 3.4.2.3 Scattering from Ice   | 54   |
| 3.4.2.4 Mass-Filtered Velocity Analysis   | 54   |
| IV DISCUSSION AND GUIDELINES FOR FUTURE WORK  | 56   |
| 4.1 Homogeneous Nucleation in the Beam  | 56   |
| 4.2 Evaporation and Detailed Balancing  | 66   |
| 4.3 Monomer Scattering  | 67   |
| 4.3.1 The Fast Peak   | 68   |
| 4.3.2 The Slow Peaks  | 70   |
| 4.4 Cluster Scattering  | 71   |
| Appendix  |      |
| A TIME-OF-FLIGHT ANALYSIS BY THE PSEUDORANDOM CHOPPING TECHNIQUE:<br>CALIBRATION AND APPLICATION TO MASS SPECTROMETRY | 75   |
| B DATA PROCESSING PROGRAMS AND DOCUMENTATION  | 88   |
| C SOME THOUGHTS ON FITTING THEORY TO TIME-OF-FLIGHT DATA  | 113  |
| D SAMPLE EXPERIMENTAL PROCEDURE   | 117  |
| E EFFECTS OF MASS SPECTROMETER AMPLITUDE CORRECTIONS ON<br>DETERMINATION OF SURFACE AND BULK ENERGIES OF CLUSTERS     | 119  |
| FIGURES   | 121  |
| REFERENCES  | 167  |

# LIST OF FIGURES

|  | Page |
|--|------|
| 1. Schematic Diagram of Apparatus . . . . .  | 121  |
| 2. Early Nozzle Source Assembly . . . . .  | 122  |
| 3. Flow Through Cylindrical Nozzle. . . . .  | 123  |
| 4. Final Source Assembly. . . . .  | 124  |
| 5. Target Assembly. . . . .  | 125  |
| 6. Important Dimensions of Beam System, Target<br>and Time-of-Flight Apparatus . . . . .                         | 126  |
| 7. Time-of-Flight Signal Processing . . . . .  | 127  |
| 8. Examples of Mass-Filtered Time-of-Flight Spectra<br>for Background Species . . . . .                          | 128  |
| 9. Mass-Filtered Time-of-Flight Spectra for Mixed<br>Ar/He Beam with $N_2/O_2/H_2O/CO_2$ Background . . . . .    | 129  |
| 10. Time-of-Flight Spectra of Argon Beam . . . . .   | 130  |
| 11. Time-of-Flight Spectra of Water Beam for<br>Varying Source Pressure. . . . .                                 | 131  |
| 12. Mass Spectrum of a Highly-Clustered Water Beam . . . . .   | 132  |
| 13. Stagnation Gauge Intensity versus Source Pressure. . . . .   | 133  |
| 14. Time-of-Flight Peak Amplitude versus Beam Intensity. . . . .   | 134  |
| 15. Mass-Filtered Time-of-Flight Spectra of a Clustered Beam . . .   | 135  |
| 16. Peak Amplitude versus Cluster Size from Mass-Filtered<br>Time-of-Flight Spectra of Beam . . . . .            | 139  |
| 17. Translational Velocity versus Cluster Size from Mass-<br>Filtered Time-of-Flight Spectra of Beam. . . . .    | 140  |
| 18. Translational Temperature versus Cluster Size from<br>Mass-Filtered Time-of-Flight Spectra of Beam . . . . . | 141  |
| 19. Mass 18 Time-of-Flight Spectra of Beam versus Source<br>Temperature ( $T_0$ ) . . . . .                      | 142  |
| 20. Peak Amplitude versus Emission Angle for Evaporation<br>from Covellite . . . . .                             | 143  |



|  | Page |
|--|------|
| 21. Time-of-Flight Spectra versus Emission Angle<br>for Evaporation from Covellite. . . . .  | 144  |
| 22. Time-of-Flight Spectra for Evaporation from Single<br>Crystal Ice . . . . .  | 145  |
| 23. Sample Time-of-Flight Spectrum with Resolved Fast<br>Peak and Maxwellian Peak. . . . .   | 146  |
| 24. Time-of-Flight Spectrum for Backscattering and<br>Amplitude versus Scattering Angle . . . . .  | 147  |
| 25. Comparison of Time-of-Flight Spectra Chopping<br>Incident Beam versus Chopping Scattered Stream<br>When Most of Beam Sticks to Target. . . . . | 149  |
| 26. Fast Peak Amplitude . . . . .  | 150  |
| 27. Velocities at Maximum Amplitudes for the Fast Peak. . . . .  | 151  |
| 28. Examples of Time-of-Flight Spectra for the Specularly<br>Directed Slow Peak. . . . .   | 152  |
| 29. Amplitudes of the Specularly Directed Slow Peak . . . . .  | 153  |
| 30. Stagnation Gauge Amplitudes for Specularly<br>Directed Slow Peak. . . . .  | 154  |
| 31. Fitting of Translating Maxwellian to Specularly Directed<br>Slow Peak . . . . .  | 155  |
| 32. Peak Positions in Time-of-Flight Space for the Specularly<br>Directed Slow Peak. . . . .   | 156  |
| 33. Peak Amplitudes versus Beam Intensity . . . . .  | 157  |
| 34. Amplitudes of the Non-Specular Slow Peak. . . . .  | 158  |
| 35. Fitting of Translating Maxwellian to Non-Specular<br>Slow Peak . . . . .   | 159  |
| 36. Peak Positions for the Non-Specular Slow Peak . . . . .  | 160  |
| 37. Velocity Spectra of the Only Three Water Species<br>Found in Scattering from Si . . . . .  | 161  |
| 38. Time-of-Flight Spectrum without Mass-Filtering for<br>Conditions of Figure 37 . . . . .  | 162  |
| 39. Components of Fast Peak Velocity. . . . .  | 163  |
| 40. Examples of Hermite Polynomial Fitting to Data. . . . .  | 165  |
| 41. Examples of Modified Gram Polynomial Fitting to Data. . . . .  | 166  |

# LIST OF TABLES

|   | Page |
|---|------|
| 1 Evaporation Data . . . . .  | 40   |
| 2 Surface Temperature Range for Observed Features. . . .  | 45   |
| 3 Source Pressure Thresholds for the Appearance<br>of the Specularly Directed Slow Peak . . . . . | 51   |
| 4 Values of $(E_i + E_f)/n$ . . . . .   | 62   |

## LIST OF SYMBOLS & ABBREVIATIONS

|          |   |
|----------|---|
| $A$      | surface energy per particle                               |
| $A_n$    | mass spectrum peak amplitudes                             |
| A/D      | analogue-to-digital                                       |
| $B$      | bulk energy per particle                                  |
| $c_p$    | heat capacity at constant pressure                        |
| $d$      | length  |
| $E_i$    | energy of internal modes                                  |
| $E_f$    | energy of formation                                       |
| $E_{tr}$ | translational thermal energy                              |
| $f(v)$   | velocity distribution                                     |
| $h$      | enthalpy per molecule                                     |
| $k$      | Boltzmann's constant                                      |
| $L$      | length  |
| LEED     | low energy electron diffraction                           |
| $m$      | mass  |
| $m_d$    | decay constant for quadrupole transmission                |
| $m^{th}$ | threshold mass above which quadrupole transmission decays |
| $n$      | number of molecules                                       |
| $n_c$    | critical cluster size                                     |
| $N_n$    | number of clusters of $n$ molecules                       |
| O.D.     | outside diameter  |
| $P$      | pressure  |
| $P_o$    | source pressure   |
| rf       | radio frequency   |
| $t$      | time  |

$T$  temperature  
 $T_0$  source temperature  
 $T_s$  surface (target) temperature  
 $T_c$  cluster temperature  
 $T_{tr}$  translational temperature  
 $TOF$  time-of-flight  
 $u$  translational velocity  
 $u$  internal energy  
 $v$  velocity  
 $v$  volume per molecule  
 $Z$  number of electrons per molecule  
 $\epsilon$  ionization efficiency  
 $\theta_i$  incident angle (measured from target normal)  
 $\theta_s$  scattering or emission angle (measured from target normal)  
 $\lambda$  mean free path

## SECTION I

### INTRODUCTION

The study of ice nucleation has been a topic of interest for many years [1-4]. Most experimental work to date has involved measurements of bulk macroscopic properties (such as temperature and pressure). Controversy arose among proponents of competing theories designed to explain the results of these measurements [5]. At the root of the controversy is the disagreement over the microscopic details on which the macroscopic models are based. The wide discrepancy among the predictions of these models suggests the need for experiments from a microscopic (molecular) point of view. The original goal of the present study was to design and perform such experiments to study heterogeneous ice nucleation (nucleation on a substrate other than ice itself).

A molecular beam scattering system seemed the ideal sort of tool to use in such a study. The fate of molecules with particular incident velocities and directions can be studied, and one can approach the conditions for the creation of stable nuclei arbitrarily slowly by controlling beam intensity and substrate temperature. Some progress has been made, but thus far, we are still unable to correlate microscopic observations with macroscopic observations in any detail. Along the way, there have been some interesting additions to the knowledge of homogeneous nucleation in nozzle beams, evaporation from surfaces, and, perhaps most importantly, the interaction of ice clusters with surfaces.

It is not practical to give a complete survey of work on ice nucleation; to do so could fill a sizeable book. Substantial portions of books by Mason [1], Hobbs [2], and Abraham [3], for example, are devoted to ice nucleation. These books are already aging by modern scientific

standards, but no major breakthroughs have occurred; Hobbs [2] can still be used for a reasonable picture of the current state of knowledge about all aspects of the physics of ice, and Abraham [3] gives a good survey of homogeneous nucleation in general. A more recent survey of homogeneous nucleation has been written by Springer [4], which includes 140 references to work in the field. We restrict discussion here to work which takes a molecular point of view, and review, in addition, some work on the experimental methods involved and some closely related work involving species other than water.

#### 1.1. ICE NUCLEATION FROM A MOLECULAR POINT OF VIEW

To date relatively little work on ice nucleation has been done from a molecular point of view, and a large share of what has been done is theoretical. Most of this work has been concentrated in a single location: the Center for Cloud Physics at the University of Missouri at Rolla. Numerous theoretical papers by Kassner, Plummer, Hale and others and some experimental papers by Levenson and others have appeared and are discussed below.

##### 1.1.1. THEORETICAL WORK

Several sorts of calculations have been performed. Hale and Plummer first constructed molecular models of small clusters of molecules of water [6] for comparison with the liquid drop theory of nucleation, which is built up from consideration of surface and bulk energies of individual clusters. Such a theory is suspect for small clusters since the extension of the concept of surface energy down to clusters of a few molecules is unrealistic. (See the controversy over the "replacement free energy" term necessary (?) to correct the model to agree with

experimentally observed nucleation rates [5]. In the theory of Hale and Plummer, free energy of formation of the clusters was calculated, and from that, macroscopic quantities (critical supersaturation ratio, critical nucleus size, nucleation rates) could be calculated. Most notable in the results, besides the small but significant deviations from the results of the liquid drop theory, was the increased stability of clathrate structures (see Section 4.1) over structures like bulk ice.

Statistical mechanics has been applied to various model systems which include models of growing clusters [7-10]. There are problems with such an approach at both ends of the size scale. First, a satisfactory statistical model requires accurate knowledge of the possible microscopic configurations and the formation energies involved. Such knowledge is still actively being sought. Boundary conditions at the edges of a system must be established though the choices made with convenience of calculation in mind may be unrealistic. A kinetic approach is necessary to handle such situations as the loss of mass as particles grow big enough to fall out of a system (snow). Statistical mechanics is most suited to the calculation of equilibrium distributions, which for the case of a system allowing cluster growth generally ends up with all the mass in a single large cluster. The fact that such a state may not be achieved in finite time or that other vastly different states may be nearly as favorable is ignored. Quantum statistical mechanics shows some promise of getting closer to first principles, since it does not require any ad hoc input of microscopic details [11].

Simulation of a nucleating system by "Molecular Dynamics"

calculations has recently been performed for a two-dimensional 100 molecule system by Zurek [12, 13]. McGinty has performed a molecular dynamics study on argon clusters [14], and Abraham, Binder and others [15-18] have performed some Monte Carlo simulations of water clusters. The approach provides useful insight into the processes which may occur in a nucleating system but with current computer technology, computing costs are prohibitive for all but the simplest systems. This situation may be expected to improve rapidly for at least a couple of decades, and simulation of more and more realistic systems should become possible.

All the calculations mentioned thus far have been for homogeneous nucleation systems typically containing only a single molecular species. Work has begun on theoretical modeling of heterogeneous nucleation. Statistical mechanics has been applied to a system including a surface, clusters on the surface, and clusters and monomers in a vapor above the surface [19]. Results which compare satisfactorily with experiments have not yet been achieved, but the method shows promise. Again it is the microscopic details which cause problems. Quantum mechanical modeling of the interaction of a monomer with a simulated surface (restricted to 10 atoms to make the calculation manageable) [20] has begun to shed some light on exactly where bonding is favorable. Such an approach may shed light on microscopic details, though as yet calculations for anything but the simplest systems are formidable.

#### 1.1.2. EXPERIMENTAL WORK

It is not possible by current experimental techniques to measure the state of individual water clusters, but one can infer the behavior of



single clusters more readily from molecular beam measurements than from any others now available. Measurements on beams themselves are described in Section 1.2. Very little work on heterogeneous nucleation has been attempted to date. The few exceptions include the work of Bentley and Hands, who studied condensation of argon, nitrogen, and carbon-dioxide on gold by monitoring reflected flux with a quadrupole mass spectrometer [21]. They found no nucleation barrier for the condensation of argon and nitrogen, and a barrier corresponding to a critical nucleus size of about 9 molecules for carbon dioxide. Nucleation apparently took place on an adsorbed layer rather than on the bare gold surface. Similar studies were performed by Levenson et al [22, 23] using a water beam, gold and silver-iodide surfaces and a quartz crystal microbalance as a flux detector. Activation energies for adsorption and desorption were obtained, and a critical cluster size of only one or two molecules was found. They also studied carbon dioxide nucleation on ice [24] finding a critical nucleus size of about 4 molecules. Such small critical nucleus sizes (compared to that for homogeneous nucleation) is surprising, but agrees with that calculated for the epitaxial growth of metals from the vapor [25].

## 1.2. CONDENSATION IN BEAMS

Condensation (clustering) in beams has become a widely studied topic. In many situations, such as the initially envisioned plan for the present study, it is desirable to avoid condensation in the beam and to have only a high intensity monomer beam. In high pressure nozzle sources of all types (whether "sonic" ("free jet"; converging nozzle

or small hole) or "supersonic" (converging-diverging nozzle)), condensation occurs readily for most species because of the extreme cooling which takes place during the expansion. Applications of condensed beams include fusion devices [26], film deposition [27], and the study of homogeneous nucleation (see below). A good general picture of condensation beams can be had by referring to recent proceedings from symposia on Rarefied Gas Dynamics [28] which included sessions devoted to "Condensation in Expansions".

Condensation has been observed in beams of Ar, N<sub>2</sub>, CO<sub>2</sub> [28, 29], H<sub>2</sub>, D<sub>2</sub>, O<sub>2</sub>, CO, SF<sub>6</sub>, UF<sub>6</sub>, [28], NO<sub>2</sub>, Kr [29], C<sub>6</sub>H<sub>6</sub>, CHCl<sub>3</sub>, CCl<sub>3</sub>F, C<sub>2</sub>H<sub>5</sub>OH [30], CH<sub>3</sub>OH [31], H<sub>2</sub>O [28, 31-37]. Some of these studies used free jet expansions and some used supersonic nozzles. Obert and Hagena [38, 39] have studied extensively the effects of various parameters of supersonic nozzles on clustering. Dankert and Koppenwallner [40] have studied the properties of clustering in free jet expansions. These results are of interest from the point of view of designing new sources (see Section 2.2), but unless a source can be exactly duplicated, it is necessary to determine the properties of each new source to the extent that those properties are relevant to any particular experiment. The theory of nozzle expansion is not sufficiently developed to predict accurately the behavior of an arbitrary nozzle, especially if there is the possibility of condensation.

A variety of techniques have been developed for the study of clusters in beams. The simplest measurements to make are measurements of pressure (density) or flux [39]. Discontinuities in these measurements

as a function of, say, source pressure have been interpreted [39] as an indication of massive condensation in the beam. Similar but more sensitive results can be obtained by scattering laser light [41]. The laser axis is along the beam axis, and the scattered light is measured perpendicular to the beam. It is also possible to scatter an atomic beam from a cluster beam [42], but the results are more difficult to interpret. Mass spectrometer techniques (quadrupole [32-34], retarding field [39] or ion time-of-flight [43]) show the most promise for actually measuring cluster size distributions, but instruments with sufficient mass range to study clusters of thousands of molecules generally have very poor mass resolution and severe amplitude calibration problems (see Section 3.1.1.). High energy (50 keV) electron diffraction measurements have been used [35-37] to determine crystalline structure and cluster size (from diffraction line widths). Electron diffraction is at present limited to the study of clusters of more than ~300 molecules.

### 1.3. CLUSTER SCATTERING

As yet there have been only a few experiments on the scattering of clusters from surfaces. Gspann and Krieg [44] have studied the scattering of helium, hydrogen, and nitrogen clusters from a stainless steel surface. The surface was carefully polished (the measured roughness depth was less than 500 Å and cleaned by baking to 450° K. Their measurements included mass spectrometry and crude velocity analysis. The beams were highly clustered consisting of clusters of  $10^4$  to  $10^5$  molecules. A grazing incident angle (84.3°) was used. Two sorts of scattering were observed. For hydrogen on a target above 215° K and

and for helium at all target temperatures tested ( $30^\circ \text{K} < T < 550^\circ \text{K}$ ) clusters gained velocity by a few per cent and lost mass. The reverse was true for hydrogen at a lower target temperature and for nitrogen. Superspecular scattering occurred for  $\text{H}_2$  and  $\text{N}_2$ , subspecular occurred for He. Nitrogen clusters apparently partially fragmented on collision, breaking into two pieces. Reflection coefficients (fraction of clusters surviving collision) were around 0-0.6 for He, 0.4-1.0 for  $\text{H}_2$ , and 0-0.1 for  $\text{N}_2$ . (The monomers resulting from destruction of clusters were not studied.) The exceptionally high reflection coefficient for  $\text{H}_2$  occurred at the so-called "optimal reflector temperature" which divided the two regions of scattering behavior.

No previous experiments (to our knowledge) have studied the scattering of water clusters from surfaces. We describe here the design and construction of a system for such a study, and give a report on experiments which we have performed thus far. Detailed theoretical modeling is incomplete, and will require some additional experimental work.

## SECTION II

### EXPERIMENTAL APPARATUS AND DATA HANDLING TECHNIQUES

#### 2.1. PRIMARY VACUUM FACILITIES

The experimental chamber was a 1.2 m diameter viton-sealed stainless steel vacuum chamber pumped by a 61 cm oil diffusion pump with a freon-cooled baffle. Additional pumping for water and other condensables was achieved with strategically located liquid-nitrogen-cooled surfaces. Pumping speed for water was more than  $10^6$  l/s versus between  $10^3$  and  $10^4$  l/s for most gases. This system has been described in some detail elsewhere [45]. The base pressure achievable was about  $5 \times 10^{-7}$  Pa with a typical operating base pressure of around  $4 \times 10^{-6}$  Pa (there were no provisions for bake-out, so pumpdown to  $5 \times 10^{-7}$  Pa took weeks).

In a typical scattering experiment, a rotatable and moveable target was mounted in the middle of the chamber with other equipment mounted in various positions around it (see Figure 1). Other equipment included a source system, a time-of-flight detection system, a stagnation gauge, and a quadrupole mass spectrometer. These are described separately below.

#### 2.2. SOURCE SYSTEMS

Early measurements were made using the source assembly shown in Figure 2. There was a brass nozzle with a cylindrical hole, .08 cm in diameter by .66 cm long. The gas was supplied either from an external manifold system or an internal water reservoir. A motor driven needle valve between the reservoir and the nozzle functioned primarily as a shutoff valve. The nozzle was located 3 cm from a collimating plate in the wall of a small liquid nitrogen cryopumped collimating chamber.

This source provided the beam for most of the calibration work on the time-of-flight detection system. It proved unsatisfactory for scattering experiments for several reasons. The liquid nitrogen pumped collimating chamber functioned satisfactorily only for a water beam (other gases used were not condensable). Even for a water beam, the geometry was such that insufficient pumping speeds were achieved, especially at higher beam intensities. As a result, achievable beam intensities were only marginally satisfactory for scattering measurements. Source pressure and temperature were often poorly controlled.

A new source system was designed and built to overcome these difficulties. The major design criteria were to be able to achieve a stream of high intensity consistent with the available pumping to direct the beam so that most of it strikes the target, to have independent control over source temperature and pressure, and to make the source readily adaptable to use with non-condensable gases in addition to water.

A nozzle/single collimator system was selected as simplest to build and adequate for the task. There appeared to be no substantial advantage to carefully designed skimmers as long as the collimator was located well downstream of the Mach disk [45]. A single stage collimation system was adequate, provided the pumping speed in the collimating chamber was high enough to render scattering in the collimating chamber unimportant. In the present system this condition was achieved for water, but probably not for argon.

The properties of flows through nozzles are not yet well understood in any detail, especially if condensation occurs. The only "nozzle" for

which detailed calculations can be made is the effusive source. Define  $d$  as a characteristic linear nozzle dimension perpendicular to the beam direction and  $\ell$  as a characteristic dimension along the beam. An effusive beam occurs for  $\ell \ll d \ll \lambda$ , where  $\lambda$  is the mean free path for molecules in the source. Rough calculations show that for practical scattering systems, it is not possible to achieve a sufficient intensity with such a source. With a nozzle source, on the other hand, one can achieve arbitrarily high intensity by increasing the source pressure. In addition the flow tends to be more directional, and, if high pressure ratios can be maintained across the nozzle, the width of the velocity distribution of the beam becomes very narrow.

Several shapes are possible for nozzles: cylindrical holes, converging ("sonic"), and converging-diverging ("supersonic") (either straight-edge or curved). The effect of some of these configurations has been studied in some detail by Obert and Hagen [38, 39]. Clustering and beam intensity were enhanced in "supersonic" nozzles. Among supersonic nozzles, larger throat diameters promoted clustering at the expense of centerline beam intensity. Large  $\ell/d$  promoted directionality (hence centerline intensity) and clustering (by extending the high pressure supersaturated region in the flow). Narrow divergence angles also promoted directionality, and a growing boundary layer made the effective divergence angle smaller than the actual physical angle.

At the time we designed the source nozzle, we were not interested in or much concerned about clusters. We chose a cylindrical nozzle with the smallest easily available hole size and  $\ell/d = 20$ . This nozzle was expected to give high intensity and good directionality. Boundary

layer effects probably give a flow pattern of the type shown in Figure 3. This is not an ideal supersonic flow profile, but experiments indicated that clustering of water molecules was very probable and actually difficult to avoid. It is not clear where in the nozzle sufficient supersaturation occurred for condensation to begin, and we have not studied the source in detail. Our primary interest was in scattering, and for that purpose, the detailed behavior of the flow through the nozzle was of secondary interest. As long as pumping speed limitations were not reached, the beam intensity and clustering could be controlled over a wide range by adjusting source pressure and nozzle temperature. The only unfortunate consequence of our choice of nozzle shape was that there was not a body of data on performance to draw on.

The nozzle diameter was chosen as .1 mm, which was the smallest readily available hypodermic tubing. We considered drilling methods, but the technology for drilling holes at reasonable cost less than about .25 mm was mostly limited to very shallow holes. Electroplating on mandrels and etching out of the mandrel is possible [38] but more difficult.

The source as constructed is shown in Figure 4. The nozzle opening was .1 mm in diameter by 2 mm long. It was stainless steel hypodermic tubing brazed into solid copper. A thermocouple (Cu/CuNi) was mounted in the copper to monitor source temperature. A 50 watt oven surrounded the copper. This oven consisted of a coil of nichrome wire mounted in grooves cut on the inside of a cylinder of lava. The nozzle was connected to a boiler outside the vacuum system via a 1.27 cm O.D. stainless steel tube. This tube was installed so that the path



from the nozzle to the boiler was unobstructed and downhill. There was a radiation shield around the tube and the source oven. The assembly functioned as a heat pipe. With no added heat at the source oven, the source temperature rose and stabilized a few degrees below the boiler temperature.

The boiler was a 7.5 cm stainless steel T holding approximately 1.5 l of water. Heat was supplied by a 1000 watt cartridge immersion heater and temperature was monitored by a thermocouple (Cu/CuNi). Temperature controllers on the boiler and source oven controlled the source pressure and temperature. These were specially built to hold temperatures to within  $\pm 1/2^\circ$  C. An overpressure relief valve was set at about 1.3 MPa. A fill tube was provided. To add water to the boiler, the temperature was reduced to below  $100^\circ$  C, a valve was opened, and water was driven in by atmospheric pressure.

The inside of the source system was almost entirely stainless steel. Exceptions were the copper at the nozzle, some silver solder, and viton O-rings at the flanges of the boiler. The viton, in fact, caused some problems; some fragments which came loose were transported through the source system and ended up plugging the nozzle. It was possible to clear the nozzle, but a future design should include copper or teflon seals, or, perhaps, a screen between the boiler and nozzle.

The collimating chamber was a rectangular region of welded stainless steel about 20 cm square extending about 50 cm into the main chamber. The region was pumped by a 45 cm oil diffusion pump connected to the collimating region by a large T. In addition there was a complete

inner wall of liquid nitrogen cooled copper which accomplished most of the pumping for water. A large access port was provided in the side of the collimating chamber and a mounting platform was put in the bottom. The front of the chamber had the top and side corners cut back at an angle of about  $30^\circ$  to provide additional manoeuvring room for the chopper. Several different collimating openings could be installed. These were circular openings in 76 micron stainless steel foil. For all the scattering experiments, a .76 cm diameter opening was selected for a nozzle located 12.4 cm away.

A solenoid-controlled beam flag was installed in front of the collimator to make it possible to turn the beam on and off quickly.

## 2.3. TARGETS

### 2.3.1. TARGET MOUNT

The target mount is shown in Figure 5. Originally it was designed to fit into a glass enclosure so that ice crystals could be grown with the assembly in place in the main vacuum system. This feature was not used in the present work. Motor drives allowed the target to be rotated and moved up and down (out of the path of the beam). Calibrated potentiometers were used to keep track of target position. Temperature control was provided by resistive heating and liquid nitrogen cooling. An early attempt to use a thermoelectric device proved unsatisfactory for the temperature range of interest. The final design described here is the third or fourth generation. It worked well over a temperature range of about  $200^\circ \text{K} < T < 700^\circ \text{K}$ . Temperature control to about  $\pm 1/2^\circ \text{K}$ . was provided by feedback control to the heater. A thermocouple (Cu/CuNi)

clamped to the target surface provided the temperature measurement, and it was this temperature which was controlled.

The assembly was very compact. Starting from the copper mounting surface, there was a sheet of mica, a coil of nichrome wire (the heater), a sheet of mica, and another sheet of copper. Four stainless steel screws with alumina spacers held this assembly to a liquid nitrogen cooled copper block. This liquid was supplied via flexible metal tubing from a reservoir. The two lines both connected to the bottom of the reservoir, and the liquid self-circulated. (No pump is necessary; there are two stable flow patterns: the liquid can flow in either direction but cannot stay still; warm fluid rising on one side pulls more cold fluid down on the other.)

The target itself was clamped to the mount, and a thermocouple clamped to the face of the target measured the temperature which was read and controlled as the target temperature. A thin film of a heat sink compound (zinc oxide loaded silicone grease) provided thermal contact for all but the ice surfaces, which were simply frozen on (in practice, "glued" with water).

#### 2.3.2. TARGETS

Several targets were used. Their preparation and characteristics are described separately.

Aluminum: a standard alloy (2024-T4) whose surface was rough-polished by a dry polishing technique developed for covellite [46, 47] was blown clean with compressed air and installed. This is a rough dirty ("engineering") surface from the point of view of a molecular beam.

Silicon: a (111) cleaved surface was used. The sample had been stored in air for about ten years. It had been used by Lewis [48], who had obtained diffraction of a He beam from the surface. The surface should be quite smooth, but may well be oxidized.

Platinum: a polycrystalline block (whose detailed history is unknown) was cleaned in trichloroethylene, acetone, and distilled water.

Glass: a pyrex cover slip (for microscope slides) was placed over an aluminum block to provide the standard target thickness. The surface was cleaned by the process used for platinum. Thermal conducting grease was put between glass and aluminum and between aluminum and target mount.

Covellite: no practical laboratory methods for preparing large single crystals of CuS are available: high pressure and long time seem to be necessary. Hence it was found necessary to use the natural mineral as it comes from a copper mine in Butte, Montana. This material is known to provide a favorable nucleating surface for ice [2, 46, 47], because it has a very similar lattice structure and size. A piece was selected which was reasonably strain free and free of iron pyrite inclusions. A surface was dry-polished parallel to the cleavage planes (readily visible). The dry polishing technique [46, 47] was developed because it appeared that water changes the surface in a way which affected the growth of macroscopic ice crystals from the vapor. Auger spectroscopy indicated that the surface was indeed copper and sulphur with no significant impurities.

Ice: single crystal ice was obtained from the Athabasca glacier

in Alaska.\* Thermal shock induced by plunging in liquid nitrogen caused cracks which indicated crystal orientation. A sample could then be cleaved or cut.† It is not easy to characterize the surface used, and samples were not saved. Cleaving ice is difficult. Best results were achieved for temperature near the melting point, but even then results were inconsistent. No attempts were made with any of the samples to obtain atomically clean surfaces.

At  $10^{-6}$  Pa, a monolayer forms on a surface in a few seconds. There was therefore no point in using conventional high vacuum surface cleaning techniques (such as argon ion bombardment). One has to be aware, though, in interpreting the scattering data, that the surfaces were not initially clean. Adsorbed water, at least, was initially driven off by heating targets to  $400^{\circ}$  K for at least 15 minutes. ( $330^{\circ}$  K for covellite which undergoes a transition at  $376^{\circ}$  K and decomposes at around  $490^{\circ}$  K) For scattering which seemed to depend on an accumulated surface layer of some sort, an additional preparation step was taken: the target was cooled to  $240^{\circ}$  K and exposed to a normally incident beam for at least 15 minutes.

\* Here again high pressure and long times are normally necessary for the formation of large single crystals. The best laboratory results are achieved by epitaxial growth from the vapor [47], but the practical limit seems to be crystals a few millimeters in diameter; which is too small for scattering experiments. A zone refining technique [49] has also achieved large single crystals and may be the best approach.

† Studies in our lab [50] following the work of Knight and Knight [51] suggest that an alternative to thermal cracking and cleaving or cutting is the use of "negative" ice crystals. If a hypodermic tube is inserted into a single crystal sample of ice, and a vacuum is maintained in the tube, crystal shaped cavities form. This, at least, gives a good indication of crystal orientation. Sizes achieved thus far are still in the millimeter range, but larger smooth crystal faces may be possible if one can avoid the tendency toward a stepped structure. For orientation determination, one could probably also make do with the crystal-shaped etch pits formed when a single crystal ice sample is put in a vacuum for a few hours at around  $250^{\circ}$  K [50].

## 2.4. DETECTION EQUIPMENT

### 2.4.1. VELOCITY SPECTROMETER

The primary measuring system for the present work was a time-of-flight velocity spectrometer. A brief description of the basic features of the system is given in Appendix A which is a copy of Reference [53]. The components of the system were essentially as described in Reference [52]. A photoetched pseudorandom chopper disk (see Figure 2 of Appendix A) replaced the machined one described in Reference [52]. The chopper and ionizer were mounted on independent arms which could be revolved around the target in the principal plane defined by the target normal and incident beam. The position of these arms could be controlled and measured from outside the vacuum system. The independent motion allowed the chopper to be positioned to chop either the incident beam or reflected stream. To obtain precise alignment of the two arms, a bare wire-wound trim potentiometer was mounted on one arm with a wiper on the other. Alignment to better than  $.1^\circ$  was easily achieved.

Distances and dimensions are indicated in Figure 6. The history of the various baffles is given in detail in Section 3.1.2.

The ionizer (the same one as was used in Reference [52]) was mounted in an open 5.4 cm. copper T, which was cooled with liquid nitrogen to keep the background gas density at a minimum in the ionizing region. The electron multiplier was mounted in the arm of the T (vertically), so that unionized beam particles passed unobstructed out of the T. Early experiments were carried out using an 18 dynode beryllium-copper venetian blind type multiplier (made by EMI). This was replaced with a continuous-

dynode semiconductor multiplier ("channeltron")(Galileo Electron Optics model 4716), which thus far appears to have a much longer usable lifetime.

Signal processing after the electron multiplier is described in Section 2.5.

#### 2.4.2. STAGNATION GAUGE

For some gas flow measurements, a glass-enclosed ionization gauge with a slit opening was mounted on one of the rotating arms. The opening was  $.12 \text{ cm}^2$ , and the volume about  $151 \text{ cm}^3$ , which gives a gauge time constant of about .08 sec. This does not agree with experimentally measured time constants: for pressures of around  $10^{-2}$  Pa the measured time constant was about 2 sec, and for lower pressures (of water, in particular), the response time is much slower: about 20 sec at  $10^{-4}$  Pa, probably due to adsorption on the glass wall.

#### 2.4.3. MASS SPECTROMETER

A late but important addition to the detection apparatus was a UTI model 100C quadrupole mass spectrometer equipped with a channeltron electron multiplier. Due to the difficulty of mounting the mass spectrometer probe on one of the moving arms, it was mounted in two fixed positions, one facing the beam directly, the other forming an angle of  $144^\circ$  from the source to the target to the mass spectrometer ionizer (Figure 1).

For studies of the beam, the range of the instrument was extended from 300 AMU to about 700 AMU by reducing the rf frequency of the quadrupole from 1.70 MHz to 1.11 MHz. Some loss of attainable resolution

occurred when this was done. Further consequences of extending the mass range are discussed in more detail in Section 3.1.1.

For some experiments, time-of-flight measurements were made replacing the original ionizer with the mass spectrometer's ionizer/quadrupole/electron multiplier assembly. This allowed simultaneous mass and velocity resolution. For these experiments, the output of the electron multiplier in the mass spectrometer was fed directly through the usual time-of-flight electronics, while the mass spectrometer was locked onto a particular mass peak.

## 2.5. TIME-OF-FLIGHT SIGNAL PROCESSING

The signal path is diagrammed in Figure 7. The electron multiplier served as a low noise high gain preamplifier. The signal then passed through a current preamplifier (gain  $10^7$  V/A) and an additional amplifier (gain 50), if necessary, to achieve a signal of a few volts. The amplified signal was generally very noisy, and some signal averaging was necessary. All the data reported here were processed through Princeton Applied Research model TDH9 Waveform Eductor which is a 100 channel analogue signal averager. (The Eductor memory consisted of a bank of precision capacitors.) Comparison with a demonstration model of a new digital signal averager made by Nicolet Instruments (model 1170) showed the Waveform Eductor to be a very effective device for processing the signals we generated. Since it used the entire signal (no sample-and-hold), it was actually somewhat more efficient than the digital instrument. The digital device was better for very noisy signals, of course, because it could continue to average indefinitely or at least until available memory is full. Also the A/D conversion was sufficiently



fast that one could achieve about a ten fold improvement in time resolution over the Waveform Eductor. This had interesting consequences for the signal from a 103 channel pseudorandom chopper. The signal, after sufficient averaging, still looked slightly noisy, because the effect of the shutter function (defined by an individual chopper slot passing the chopper collimator) was resolved: there were 103 little bumps superimposed on the signal!

The trigger signal for the Waveform Eductor was supplied by a photodiode-phototransistor which sensed the passage of a long slot which occurred once for each repetition of the chopping sequence. A dead space of 3 channels was set so that the Waveform Eductor channel width matched the chopper channel width. This dead space was usually set to span the time of the phototransistor signal pulse which was picked up slightly on the signal line. The missing channels were interpolated. For most signals, interpolation did not introduce noticeable error, since the deconvolution process for pseudorandom chopping used all channels to reconstruct each channel of the deconvoluted signal.

The averaged signal was displayed on an oscilloscope. When a signal of interest was ready, it was read through a buffer amplifier (to protect the A/D converter from voltage spikes) and A/D converter into an on-line PDP-11/03 computer. This A/D converter was not fast enough to handle the signal directly, which is why the Waveform Eductor was necessary. A typical period (time for 103 channels) was 1-2 msec. For read-in to the computer, a period of about .1 sec. was used. Once the signal was in the computer, a great variety of manipulations were possible. These are described in Section 2.6.

## 2.6 SOFTWARE

A series of routines were developed to process the data. They are given in Appendix B along with user instructions. All were written in FORTRAN and run under the RT-11 version 3 operating system. System hardware included dual floppy disks, a programmable clock, a VT55 graphic display terminal with electrostatic hard copy unit, and a Hewlett-Packard model 7225A digital plotter. Special subroutines were available from the manufacturer or were written for these devices.

Subroutines were written to be self-contained and accessible in any order. Basic data handling routines included routines to read in new data and store it on disk, read in old data off disk, and to consolidate disk files at the end of an experimental run (each trace was initially stored in a separate file to provide crash-resistance for the data). The data could be plotted directly as read in. All plotting could be done either on the graphic display terminal or the digital plotter. Hard copies of the display on the terminal were the most common means of collecting paper copies of graphs since it was faster than using the plotter. Good plotter copies could always be generated as needed, since all data were on file.

The data processing routines are as follows: first, of course, a deconvolution routine [52] recovered a time-of-flight spectrum from the pseudorandom chopped signal. As long as one channel width time resolution was satisfactory, no further corrections were necessary. See Reference [52] and Appendix A for a discussion of shutter function effects and the effects of a finite length ionizer. A smoothing routine was available using a low-pass digital filtering scheme [59]. In

general, this routine was not found to be useful. The noise accompanying the signal was due primarily to statistical fluctuation in the background gas density. As such, it was white noise. A low pass filter cut out the high frequency components, but left low frequency ones. The human eye/brain handled the unfiltered version better since the low frequency noise might look like signal when it alone was present.

Various theoretical plots were relevant to the measurements and appropriate fitting routines were devised for comparing the data to them. Most of these routines fitted a Maxwellian or translating Maxwellian or the sum of two such velocity distributions to the data. To avoid the hazards of non-linear least-squares fitting, only amplitudes were used as fitting parameters. Other parameters were taken as fixed, and if they were not independently measurable, they were determined manually by a guess and try method (manual non-linear least-squares fitting). Such guessed parameters included Mach number and temperature for translating Maxwellians;\* for static Maxwellians, all parameters were known. Fits could be made to all or part of an experimental curve as appropriate. Routines were also available to subtract out parts of a signal. For example, it was often desirable to subtract out a Maxwellian component to be better able to study the remaining features.

In practice, the most useful information could be extracted by these fitting routines, or by an even simpler routine which just identifies peak positions and amplitudes. This is in accord with common practice. See Appendix C for a more detailed discussion.

---

\* For "good" data (signal/noise  $\geq 50$ ), experience with fitting suggested that these parameters could be determined with some confidence (e.g.  $\pm 5\%$  for temperature) by this technique. Note, however, the caution at the end of Appendix C.

## SECTION III

### DATA

A lot of data were collected for this study. There were, for example, some 2000 time-of-flight spectra taken in the course of some 100 experimental runs. It is, therefore, not practical to present all the raw data. They are stored on disk and in a file at the lab. (Fluid Dynamics Research Lab, Rm. 37-442, MIT) Instead, the information has been consolidated and combined as much as possible. Hopefully, this has made the material more digestible, and no important data have been omitted.

The data are presented and discussed in four main divisions. First there is a discussion of instrumental calibration and of spurious signals which were eliminated and are not present in any of the remaining data. Then there is a discussion of the properties of the beam. A few results of some studies of evaporation follow, and finally the scattering data are presented.

#### 3.1. CALIBRATIONS AND ELIMINATION OF ARTIFACTS

##### 3.1.1. MASS SPECTROMETER

The mass calibration was factory set for the 1-300 AMU nominal range of the instrument. Checks against known gases (He, N<sub>2</sub>, H<sub>2</sub>O, O<sub>2</sub>, CO<sub>2</sub>, Ar, Kr) verified this calibration, at least for the low AMU range. Above 84 AMU (Kr), and for the instrument as modified for higher mass range, the clusters in the water beam provided a very convenient calibration series. There are peaks in the mass spectrum of a clustered water beam at  $18n+1$  AMU intervals corresponding to protonated water clusters.

Mass peak amplitude calibration is a more difficult matter. For the most part the problem was ignored, and quantitative measurements were not made. To make a satisfactory calibration requires known amounts of the species to be measured and approximately the same vacuum and flow conditions. Short of this, several corrections can be made, which should allow relative peak amplitude comparison at least to within about a factor of two.

First, ionization efficiency is a function of AMU. Data provided by the manufacturer [55] taken from work by Flaim and Ownby [56] suggest as a good approximation:

$$\epsilon = .6 \frac{Z}{14} + .4 \quad (2.1)$$

where  $\epsilon$  is the ionization efficiency relative to  $N_2$ , and  $Z$  is the sum of the atomic numbers (number of electrons) of the atoms in the ion in question.

Second, the gain of the electron multiplier depends on species in an irregular manner depending on mass, charge, reactivity, and accelerating voltage. Roughly, one finds that there is an  $m^{-1/2}$  dependence [55] where  $m$  is the mass of the ion or ion fragment.

Finally, transmission through the quadrupole is also a function of  $m$ . For the instrument, as delivered, the manufacturer reports [55] that transmission is near 100% for less than 40 AMU and drops off approximately one decade for every 150 AMU thereafter. This is presumably correct for some standard setting of the resolution control. There is a tradeoff between quadrupole transmission and resolution. No estimate of the magnitude of the effect of this tradeoff has been made.

As the rf frequency is lowered to extend the mass range, the transmission goes up roughly proportionally to the mass range. (This last observation is based on some qualitative observations and may be inaccurate. The adjustments in the resolution setting which go along with extending the mass range may be more important.) As yet, we have not been able to apply corrections satisfactorily to obtain relative amplitudes over a large mass range.

### 3.1.2. TIME-OF-FLIGHT APPARATUS WITHOUT MASS FILTERING

Many problems were encountered before satisfactory operation of the time-of-flight apparatus was achieved. Most of these are associated with the time resolution and sensitivity achieved with the present equipment, and were not noticeable with most of our previous equipment. Problems were found associated with each of the components of the system: chopper, ionizer, and electron multiplier. We consider each of these problems and their solutions separately.

When the photoetched pseudorandom chopper disk was first installed, we observed consistent spurious "bumps" on the time-of-flight spectrum. These turned out to be due to a drafting error by the company which made the disks. One line representing the edge of a slot was drawn 1/2 channel off from where it should have been. Simulating the effect of this error on a computer indeed produced bumps of the kind we saw. The error was corrected.

A more elusive problem was a spurious signal which appeared to be due to particles which passed through some portion of the chopper and struck at least one other surface before entering the ionizer. We also

suspected that beam particles might strike the edge of a chopper slot and continue on to produce a coherent signal. The evidence for this comes from observation of variations in the spurious signals as a function of chopper rotation direction. Note that the pseudorandom chopper provides a substantially larger total area of slot edge per cycle than does a single slot chopper. These spurious signals manifested themselves as an assortment of bizarre waveforms (i.e. they could not readily be explained as time-of-flight spectra) which could be generated even with gross misalignments of the components of the apparatus (for example, with the chopper at  $90^\circ$  from the target-ionizer line). A set of properly placed baffles solved these problems. Disks were placed shielding both sides of the chopper disk except where the beam was to pass through. Baffles attached to the ionizer restricted the possible multibounce paths from the chopper to the ionizer. There is, of course, the potential hazard that all this extra baffling might introduce problems of its own. In particular, the baffles next to the chopper might, in effect, momentarily trap blocked beam particles which could then pass through the chopper when next it opened. This would produce an unpredictable coherent noise source which would not be averaged out. We can only say that there is no evidence in any data for an artifact of this sort. With all the baffling in place signals were obtained when and only when they were expected, and a good calibration match could be obtained with a Maxwellian stream (see below).

The ionizer's job is to form ions from the neutral beam and pass them on to the electron multiplier in a time interval negligible compared to the flight time between chopper and ionizer. Not all ionizer

designs successfully perform this task. A box ionizer (similar to many widely used ionizers) which we used initially appeared to introduce delays of tens of microseconds. When that ionizer was replaced with a tapered cylindrical ionizer which provided a draw out potential of a few volts throughout the ionizing region, the delays disappeared. This problem reappeared when mass-filtered time-of-flight spectrometry was attempted as noted in Section 3.1.3.

Vibration of the ionizer can cause an undersired signal by changing the filament-grid spacing. Most sources of vibration are not at the chopper frequency, so that as long as they do not produce too large a signal, they average out nicely. The chopper itself, however, was initially a source of vibration at the chopper frequency. With the chopper mounted on (hung from) springs, and the chopper and ionizer on independent arms, this problem was eliminated.

The major problem caused by the electron multiplier was due to the fact that its gain had both short and long-term drifts which made it difficult to obtain precise amplitude information. One problem did surface briefly when the channeltron electron multiplier was first installed. The time-of-flight peaks inexplicably appeared to split into double peaks. The problem was apparently again one of non-negligible ion flight time — in this case, probably, a short and a long time both being possible. A grid across the cone-shaped opening of the multiplier set at the multiplier high voltage (typically -1500 V to -2000 V) solved the problem, presumably by providing a stronger field to attract the ions to the multiplier.



With all these problems ironed out a careful calibration of the instrument was possible (and necessary in light of the large number of things which can evidently go wrong with a time-of-flight system). First, of course, a check was made to make sure that signals were achieved only under conditions where they were expected. One extraneous signal source was never fully eliminated: a small electrical pickup of the phototrigger pulse. For the most part, the dead time in the Waveform Eductor sweep could be set to span this pulse, but occasionally one or two data channels might have to be discarded and interpolated.

Second, the time origin had to be located precisely. This procedure has been previously described in some detail [52,53] but as the most recent description was never published, it is included in this document as Appendix A. Note especially Section A4.

Once the time origin was located, it was possible to make a direct calibration comparison using a beam whose velocity distribution is known. The only such distribution available is the Maxwellian. A reliable source of a Maxwellian stream is an effusive flow at high Knudsen number using an inert gas. Such a calibration was performed using He, Ne, Ar, and Kr. Data are presented in References [52,53]. The reported time origin discrepancy [52] has been eliminated. The calibration has been generally confirmed by some of the experimental data itself which include studies of two additional sources of near Maxwellian streams, evaporation from a surface, and backscattering from a surface (which in the present experiments consisted only of trapped-reemitted particles). While these are not satisfactory for primary calibration,

they do provide a convenient check on the continued proper functioning of the apparatus with time.

### 3.1.3. TIME-OF-FLIGHT APPARATUS WITH MASS FILTERING

The mass-filtered version of the time-of-flight apparatus (described in Sections 2.4.1 and 2.4.3) was identical to the unfiltered version except in the region between the ionizer and electron multiplier. For the quadrupole mass filter, ions are accelerated only to about 15 V. The filtering action is not directly dependent on this voltage, but for proper functioning, the ion energy must be kept low enough so that the ions are in the finite length quadrupole field for at least several rf cycles. In principle, the ion travel time should still be negligible: at 15 V, the ions travel about 1000 times faster than the neutral beam and traverse the quadrupole in about 1  $\mu$ s.

Several tests were performed which allow us to assess the reliability of the mass-resolved time-of-flight data. First, the system was checked to see if any ionizer parameters (electron energy and current, ion energy, and focus voltage) affected a time-of-flight spectrum in any way other than the expected amplitude changes. Moderate changes (up to about 50 %) in these parameters from the normal settings recommended and set by the manufacturer had no measurable effect. Larger changes caused waveform distortions and overall delays, but the normal settings gave reliable reproducible results.

Next, comparisons were made between time-of-flight spectra with and without mass-filtering. An argon beam provided a signal which was almost entirely at 40 AMU. Since the flight paths for the two versions were different, the comparison was made by fitting the same translating

Maxwellian to both spectra. A satisfactory match was achieved, but only by introducing a delay of 330  $\mu$ s to the fitted curve for the mass-filtered spectra (cf. the chopper period of 2.96 ms and peak position at 1.09 ms). A similar calibration using water evaporating from a surface (normal emission direction) and the mass spectrometer positioned to look at a scattered stream (the beam passes through the ionizer in a different direction in this case) yielded an apparent delay of 90  $\mu$ s. The reason for the discrepancy has not been determined, and additional tests need to be made. If the difference is due entirely to the change in the orientation of the beam relative to the ionizer, then the delay can be measured and the appropriate correction can be applied to all subsequent data. The possibility of mass-dependence has not yet been ruled out, however. Ideally, of course, the delay should be eliminated. The use of an ionizer of the type we built for our time-of-flight apparatus without mass-filtering might eliminate the delay, but one might still expect problems, since in our design, there is an accelerating potential of 1.5-3 kV drawing the ions from the ionizer to the electron multiplier, whereas in the mass spectrometer there is only a 15 V potential drawing ions into the quadrupole field.

The position we have taken tentatively in the interpretation of mass-filtered time-of-flight data is that for a given experimental configuration, there is a constant delay independent of species (mass) and velocity. The magnitude and constancy of the delay is still uncertain and this should be borne in mind in interpreting the data; however, the shape of the distribution should be reliable.

In the category of artifacts, there were some rather interesting

observations made with mass-filtered time-of-flight spectrometry. It was possible to obtain quite satisfactory time-of-flight spectra for species present in very small quantities, since the statistical noise is only that associated with density fluctuations of the species being observed. It was, for example, quite easy to obtain a time-of-flight spectrum  $^{36}\text{Ar}$  and  $^{38}\text{Ar}$  in an argon beam. Unfortunately, we could also obtain clean signals at some mass numbers which could not be associated with anything in the beam (see Figure 8) and were attributed to species present in the background gas. The time-of-flight spectra for these background species were different from those of beam species. In fact, the spectra cannot be interpreted as time-of-flight spectra because they dipped below zero in intensity. The dip below zero is real (not an artifact of overlapping spectra); extending the chopper period substantially showed the steady-state background level to be above the dip. A demonstration of this phenomenon was made using a mixed Ar/He beam. Normal spectra were found at 4 and 40 AMU, while anomalous spectra were found at 18, 28, 32, and 44 AMU (see Figure 9). No signal was achieved for any mass not present in the mass spectrum of the beam or background.

It is not possible to explain these signals as due simply to chopped background gas. The number of particles which just happened to be passing in the right direction to go through the chopper to the ionizer was too small. Experimentally, this was readily verified by turning off or blocking the beam; in which case no time-of-flight signal could be observed. In order to explain the signals, one must postulate a mechanism involving entrainment, or more precisely, single collisions

between beam and background particles. To account for significant signal intensity, such collisions must occur after the chopper, and, most likely, in the immediate vicinity of the ionizer. As long as only a single collision is involved, it is reasonable to suppose that correlation with the chopper is well maintained. Collisions could also knock particles out of the ionizer which might otherwise be ionized, and this could explain the dip below the background level. A detailed modeling of this process has not been attempted, but it seems to be the only plausible explanation for the observed features. At present we know of no way of extracting useful information from these signals. Since they can be readily identified by their signature, there appears to be no problem identifying spectra which are associated with the beam. It is, however, interesting to note that the signals from background species must also contribute to the signal one obtains without mass-filtering. Fortunately, it is unlikely that a situation could be devised where these spurious signals would contribute measurably to the total signal. At least for the mechanism suggested above, there must be many more chopped beam particles than affected background particles reaching the ionizer.

### 3.2. SOURCE STUDIES

The primary focus of the present study was on the scattering of a water beam from surfaces. First, however, the characteristics of the source, and more particularly, the water beam had to be understood. The initial study of the source was with argon.

### 3.2.1. ARGON

The relatively low pumping speed for argon in the collimating chamber limited source pressures to values below 25 kPa; at ~25 kPa, the pressure in the collimating chamber rose to about  $10^{-2}$  Pa, resulting in significant attenuation of the beam due to scattering. The velocity distribution of the Ar beams could be fitted well to a translating Maxwellian, when the beams were generated at source pressures below about 18 kPa and nozzle temperatures around room temperature (Figure 10a). At higher source pressures, argon dimerization resulted in the production of two peaks in the time-of-flight spectrum (Figure 10b). Dimers have been observed before by others [e.g.28] using mass spectrometry, and we also subsequently verified their presence in our beam by mass spectrometry. At nozzle temperatures  $> 100^{\circ}$  C, the dimers were not observed.

### 3.2.2. WATER - GENERAL CHARACTERISTICS AND VELOCITY ANALYSIS

The high pumping speed available for water allowed the use of source pressures to over 1 MPa. In fact, no limit on source intensity was ever reached in our studies. The velocity distribution (without mass-filtering) as a function of source pressure is shown in Figure 11. A typical mass spectrum is shown in Figure 12. Stagnation gauge intensity measurements as a function of source pressure are shown in Figure 13. A plot of peak amplitude in time-of-flight spectra versus stagnation gauge intensity measurements is given in Figure 14. At very low pressures the velocity distribution approaches a Maxwellian. At high pressures, the velocity distribution could not be fitted even to a translating Maxwellian. In particular, a substantial low-velocity

tail appears, which we attribute to clusters (see Section 3.2.4). At high pressures, mass spectrometry indicated that the beam was highly clustered. Substantial superheating (heating the nozzle above the boiler temperature) was required to eliminate all clusters. For example, for a boiler temperature of 376° K, clusters were formed for nozzle temperatures below about 550° K.

### 3.2.3. MASS ANALYSIS

Referring again to the mass spectrum in Figure 12, several interesting features should be noted. Mass peaks were located at  $18n + 1$  AMU (and also 1, 17, 18 and 20 AMU) in the range  $1 \leq n \leq 37$  which is, at present, the extended range of the mass spectrometer. Presumably the pattern would continue beyond  $n = 37$  if the range of the instrument were extended further. Electron diffraction studies of beams formed under similar conditions [35-37] have indicated clusters of  $n = 1000$  or more. There are two possible explanations for peaks at  $18n + 1$  instead of  $18n$ . Either an  $\text{OH}^-$  was removed on ionization of a cluster or an  $\text{H}^+$  was added. The mechanism of proton addition is favored by mass spectrometrists [34,57] as an explanation of our mass spectra. It is a common process in high density ionization processes. The mean free path of neutral species in the ionization region was on the order of meters. (The "total pressure" measured in the ionization region was never  $> 10^{-3}$  Pa.) On this basis collision probabilities would be expected to be very low. There is, however, a significant attractive force between a proton and a neutral water molecule due to the dipole moment of the molecule, which increases the effective "size" of a molecule and decreases the mean free path for a proton - molecule

collision by two to three orders of magnitude. On this basis the mechanism of proton addition appears plausible.

It is interesting to note that whatever the ionization process for the clusters is, it appears to be "clean" for the low mass range studied. We have been unable to find any evidence of fragmentation of clusters on ionization; we have observed no changes in the mass spectrum over a range of electron energies, currents, and ion energies. This is in contrast to mass spectrometry of large molecules which typically fragment into many pieces. Half-order peaks appeared for  $18\frac{1}{2} \leq n \leq 37\frac{1}{2}$ ; these had a threshold of  $\sim 40$  V for the electron energy, suggesting that they were due to double ionization. If this is the case, clusters of up to 75 molecules have been detected. An alternative explanation [34] is the attachment of contaminant molecules to the clusters. Unless nitrogen or oxygen or other permanent gases are the contaminants, this explanation seems unlikely, especially in light of the prolonged steam cleaning of the source assembly through several months of use prior to the mass analysis.

Lin also observed the half-order peaks in his mass spectrometer data [32] for the range  $18\frac{1}{2} \leq n \leq 30\frac{1}{2}$ . He attributed these peaks to the attachment of a molecule of silicone pump oil to the clusters. He did not identify his pump oil, but claimed a molecular weight of 333 ( $= 18\frac{1}{2} \times 18$ ). Data from manufacturers on various diffusion pump oils give "average" molecular weights of between 400 and 500. A range of values should be present in any given oil sample, so a value of exactly 333 is far-fetched. Double ionization remains the most plausible explanation for the half-order peaks.



For clusters of  $n > 3$ , one looks for a signal at  $18n + 1$  AMU. It is less clear where one should expect the signal from a dimer or trimer, or to what original particles to attribute the signal at mass 19. Three sources may contribute to  $m = 19$ : protonated water monomers and fragmented dimers (already mentioned) and isotopic species. Ordinary terrestrial water is known to consist of 99.73%  $^1\text{H}_2^{16}\text{O}$ , 0.20%  $^1\text{H}_2^{18}\text{O}$ , 0.04%  $^1\text{H}_2^{17}\text{O}$ , and 0.03%  $^1\text{HD}^{16}\text{O}$  [2]. Thus 0.07% is mass 19 and 0.2% is mass 20. With a high intensity water source these species are quite detectable. Since the amplitude of the mass 19 signal is appreciably greater than 0.07% of the mass 18 signal, the contribution of isotopes alone is not an adequate explanation; probably the other two sources of  $m = 19$  give rise to the observed signal.

The general amplitude trend in the mass spectrum (Figure 12) is a monotonic decrease with increasing AMU. The actual relative amplitudes of clusters of different size are not the same as those shown in Figure 12 because of the amplitude calibration difficulties (see Section 3.1.1). There are, however, three anomalies in the plot which should be noted. First is the relatively large peak at  $n = 21$  and the relatively small one at  $n = 22$ . The amplitude increases from  $n = 22$  to  $n = 25$ . Finally there is a small dip in amplitude at  $n = 30$ . (See Section 4.1 for further discussion.)

#### 3.2.4. MASS FILTERED VELOCITY ANALYSIS

Time-of-flight spectra associated with specific cluster sizes in the beam are shown in Figure 15. See also Figure 11 which gives the spectrum without mass-filtering. For  $n > 3$  ( $m \geq 73$  AMU), the spectrum

for each cluster size could be fitted very nicely to a translating Maxwellian (Figure 15). In order to perform such a fitting, it was, of course, necessary to select a time delay (see Section 3.1.3). The delay was assumed constant for all cluster sizes. To select a delay, the peak position of the larger clusters ( $n \geq 15$ ) was matched to the peak position of the spectrum without mass-filtering. This peak position also coincided with the position of the larger of the two peaks in the monomer distribution, so it was thought that the combined effect of a large number of monomers and different sized clusters at this particular time-of-flight would produce a peak at the same position when no mass-filtering was used. The delay chosen in this way was 157  $\mu$ s. In any case, an error in the choice of time delay affects the magnitude of the temperatures and velocities determined from the fitting, but not the qualitative trends.

Three parameters were obtained from this fitting process: amplitude, velocity, and translational temperature (along the beam direction; there could conceivably be a different temperature associated with thermal motion orthogonal to the beam or within a cluster). These are plotted in Figures 16, 17 and 18. Only a few amplitudes can be compared, since to maximize signal-to-noise in time-of-flight spectra, the electron multiplier gain was changed occasionally. The corrections cited in Section 3.1.1 apply equally to both mass spectrometer data and mass-filtered time-of-flight data, and hence the amplitudes in Figure 16 can be compared directly to the amplitudes in Figure 12. Note, however, that the time-of-flight apparatus without mass filtering is not hampered by quadrupole transmission losses. The low velocity tail in Figure 11,

which is evidently due to clusters beyond the range we have been able to study with the mass spectrometer, will not be as prominent in mass-filtered analysis.

The translational velocity data shown in Figure 17 is striking in that most clusters moved with nearly the same speed. Note that this speed is substantially faster than that which could be achieved in an unclustered expansion by converting all the enthalpy in the source into directed motion as indicated in the figure (see also Section 4.1).

The temperature data as plotted in Figure 18 assumes a monomer mass for all cluster sizes. Using the mass of the clusters in the fitting, one would find that the temperature is proportional to the cluster size for the range of sizes where the temperature plotted in Figure 18 is constant! See Section 4.1 for a discussion of this phenomenon. Note also that the temperatures determined in this way are somewhat lower than the 100-150° K suggested by Stein and Armstrong[35] for their beams. No explanation is available for the discrepancy between the data taken in the two separate runs. The source conditions were nearly identical, and the experiments must be repeated and extended to resolve the discrepancy.

Only a small amount of data has been taken thus far as a function of source pressure. The effects on the time-of-flight spectrum without mass filtering were cited in Section 3.2.2 and are shown in Figure 11. We attribute the appearance of a low velocity tail to the formation of large ( $n > 37$ ) clusters in the beam. The double peak in the time-of-flight spectra for masses 17, 18, 19, 20 and to a lesser extent 37 and 55 also correlates with the formation of large clusters. For example, raising

the source temperature only 20° caused substantial changes as shown in Figure 19. Apparently, the slower peak is in some way associated with the formation of large clusters. See Section 4.1 for further discussion.

### 3.3. EVAPORATION

Some interesting information was obtained by looking at the material emitted by an evaporating ice surface with no impinging beam. The study of evaporation was never a major goal of the project, so the data are somewhat incomplete. There are several interesting features in the data, though, so we present what we now know.

A summary of experimental conditions studied is given in Table 1.

Table 1. Evaporation Data.

| Surface              | Temperatures | Findings   |
|----------------------|--------------|--|
| Single Crystal Ice   | 214-224°K    | For low end of temperature range, emission is monomer cosine/Maxwellian at a temperature 10-20° below surface temperature. At higher temperatures, emission is non-Maxwellian and there may be dimers emitted. |
| Polycrystalline Ice  | 229°K        | Emission is monomer Cosine/Maxwellian at ~209°K.   |
| Deposit on Covellite | 204°K        | Higher amplitude toward tangent, velocity Maxwellian at tangent, slower at normal.   |
| Deposit on Silicon   | 210°K, 212°K | Maxwellian at surface temperature.   |
| Deposit on Platinum  | 207°K, 212°K | Maxwellian at surface temperature.   |

Two bulk ice surfaces were used, one cut from single crystal glacial ice, and one from a polycrystalline sample. Also studied were evaporation of accumulated ice layers on covellite, silicon, and platinum. It was only possible to study a fairly narrow temperature range (approximately  $210^{\circ} \text{ K} < T < 225^{\circ} \text{ K}$ ), because the vapor pressure of an ice surface rises very rapidly with temperature.

Roughly speaking, the emission from all evaporating surfaces was Maxwellian/cosine (i.e. the velocity distribution was Maxwellian at the surface temperature and the spatial distribution was cosine). There were, however, some notable exceptions, and these are the observations of particular interest.

The mass-filtered time-of-flight spectra allowed mass analysis of the evaporating particles separately from the background (see Section 3.1.3). Under all circumstances, signals could be found at mass 18 and 17. At higher target temperatures a signal appeared at mass 19. No signal was ever conclusively identified at mass 37 or higher. The signal at mass 19 is most likely due to dimers (see Section 3.2.3). Proton addition is not likely to be important, since the pressure at the ionizer is on the order of  $10^{-5} \text{ Pa}$ . Isotopic contributions are not ruled out entirely, because relative amplitudes of mass 18 and 19 signals were not obtained. Dimers may be formed shortly after leaving the surface, rather than before, since the mean free path in the vicinity of the surface may be quite small. For comparison, the mean free path at the equilibrium vapor pressure of ice at  $225^{\circ} \text{ K}$  is about 1 mm.

In almost all cases, there were no measurable deviations from a cosine spatial distribution. The exception was the evaporation of a

substantial frost-like accumulation on covellite. The amplitude of the emitted stream was significantly higher toward the tangent than at the normal (see Figure 20). This may simply reflect the needle-like crystal habit (parallel needles sticking out from the substrate) which, in effect, provided a large area of surface with very short linear dimension oriented perpendicular to the target. Cosine emission from such needles may well give the unexpected amplitudes observed.

Only one surface showed a measurable variation in the velocity distribution as a function of angle (see Figure 21). This was again the frost on covellite. A good fit to a Maxwellian was achieved for angles near the tangent. For near-normal angles there was a significant deviation toward slower velocities. If this is interpreted as a temperature change in a Maxwellian distribution, the normally emitted particles are some 20° C colder than the target. Again, the variation may reflect the crystal habit.

Evaporation of accumulation on silicon and platinum gave a good fit to a Maxwellian at the surface temperature. Evaporation from bulk ice samples both single crystal and polycrystalline, showed a deviation toward slow velocities for all angles, which again can be interpreted as a 30° C cooling. The immediate question is whether or not the surface temperature was in fact being measured correctly. In most cases the thermocouple was clamped to the surface. The calibration of both the thermocouple and time-of-flight equipment were reliable (at least to within about  $\pm 3^\circ$  C), and were checked together by backscattering experiments (see Section 3.4.2.2.1). Even when the thermocouple was embedded in the ice, temperature gradients were not likely to be a

problem. At typical evaporation rates, the power being carried away from the surface is only sufficient to maintain a temperature gradient of a fraction of a degree across the ice sample.

An exception to this behavior was noted for a single crystal ice sample at 221° K and is shown in Figure 22. The velocity distribution now had a distinctly non-Maxwellian shape. The average velocity was somewhat faster than the average of a surface temperature Maxwellian. Whether this behavior was due to surface phenomena, or collisions in the gas phase immediately adjacent to the surface is not clear and cannot readily be resolved by time-of-flight techniques.

### 3.4. SCATTERING DATA

#### 3.4.1. Early Studies

In this category we include all data prior to the installation of the new source system in May, 1979 (see Section 2.2). Experiments involved scatter of water and carbon dioxide beams from surfaces of covellite and aluminum. Argon scattering was attempted, but the signal levels achieved were inadequate. The water data are fully superseded by more recent data. Source pressures of less than 10 kPa were used, and only the scattering patterns which we now associate primarily with monomer scattering appeared.

The carbon dioxide scattering data are of some interest, because they are unique. Measurements were limited to a room temperature nozzle and a source pressure of ~5 kPa. Signal to noise levels were not great (about 15:1 after averaging), but some tentative conclusions were possible. The scattering was primarily diffuse. No deviations from a

Maxwellian velocity distribution at the surface temperature were definitely identified. Such deviations as were suspected were similar to those observed with water. Deviations from a cosine spatial distribution also showed patterns like water: there was a greater intensity at the target tangent than at the target normal. It would be interesting to repeat these experiments with the higher intensity source, but to achieve comparable source conditions would require a chilled nozzle.

#### 3.4.2. THE WATER SCATTERING DATA

##### 3.4.2.1. EXPERIMENTAL CONDITIONS TESTED

We describe here the results of studies made using a water beam formed in the final source assembly described in Section 2.2. The primary detection system used was the time-of-flight spectrometer (without mass filtering). Experimental parameters varied were source pressure and temperature, target material, temperature, and history, and incident and scattering angles.

Source pressure was varied up to about 1 MPa. Nozzle temperature varied little on an absolute scale. The range was from the boiler temperature of 370-470° K up to about 620°K. The main effect of these variations was on the degree of clustering of the beam (see Section 3.2).

Six targets were tested: Al, Pt, Si, Glass, CuS, and H<sub>2</sub>O. The differences in scattering from these surfaces are summarized in Table 2 and described in more detail in Section 3.4.2.2. Descriptions of the surfaces themselves are given in Section 2.3.2. Incident and scattering angle effects are also described in detail in Section 3.4.2.2.



Table 2. Surface Temperature Range for Observed Features.

| Surface                     | Maxwellian Peak  | Fast Peak  | Specular Slow Peak                                    | Non-Specular Slow Peak                                |
|-----------------------------|--|--|---|---|
| Cleaved Si(111)             | $\updownarrow$<br>$T_s \geq 210^\circ\text{K}$<br>$\downarrow$ | $\updownarrow$<br>$T_s \geq 210^\circ\text{K}$<br>$\downarrow$ | $210^\circ\text{K} \leq T_s \leq 300^\circ\text{K}$   | $210^\circ\text{K} \leq T_s \leq 300^\circ\text{K}$   |
| Polished Pt polycrystalline |  |  | Not present   | $210^\circ\text{K} \leq T_s \leq 500^\circ\text{K}^a$ |
| Polished CuS (1000)         |  |  | $210^\circ\text{K} \leq T_s \leq 300^\circ\text{K}^b$ | $210^\circ\text{K} \leq T_s \leq 330^\circ\text{K}$   |
| Polished Al polycrystalline |  |  | Present at $225^\circ\text{K}^c$                      | ? <sup>c</sup>  |
| Glass                       |  |  | $210^\circ\text{K} \leq T_s \leq 300^\circ\text{K}$   | $210^\circ\text{K} \leq T_s \leq 500^\circ\text{K}$   |
| H <sub>2</sub> O (1000)     |  |  | Present <sup>d</sup>                                  | ? <sup>d</sup>  |

a No upper threshold found

b A weaker feature than on other surfaces

c Except as noted, conditions not checked

d Very difficult to identify because of evaporation from the surface

#### 3.4.2.2. FEATURES OBSERVED

Four distinct types of scattering were detected. To facilitate discussion, we label these in terms of their distinguishing characteristics in the time-of-flight spectra: the "fast peak", the "Maxwellian peak", the "specularly directed slow peak", and the "non-specular slow peak". Labels which are descriptive of the mechanism of scattering must await understanding of the mechanism.

Each of the four features cited has been independently resolved under some experimental conditions. Under most conditions at least two features overlapped to the extent that there was no valley between them. This was particularly the case with the fast peak and Maxwellian peak, but one example where they are resolved is shown in Figure 23.

Also note the spectrum shown in Figure 25b, where the Maxwellian peak is undetectable. In cases where the two peaks are unresolved, it seems reasonable to assume on the basis of backscattering observations (where only the Maxwellian component survives [see Figure 24]) that the "Maxwellian peak" in the unresolved spectrum is indeed a Maxwellian at the surface temperature and cosine spatially, hence one can isolate the fast peak with some confidence by subtracting out a Maxwellian at the surface temperature. The amplitude of this Maxwellian cannot be determined with satisfactory precision from backscattering data, because there are substantial drifts in the gain of the electron multiplier with time. Instead, an amplitude is typically chosen such that the remaining peaks have plausible shapes and there is no dip below the zero amplitude line.

The properties of the four peaks are described individually in the following sections. Discussion of possible scattering mechanisms is deferred to Sections 4.3 and 4.4.

#### 3.4.2.2.1. THE MAXWELLIAN PEAK

As discussed above, our experiments indicate that this feature is Maxwellian/cosine (monomer) at the surface temperature (see Figure 24). It was found under almost all experimental conditions, though it was sometimes dwarfed by either the fast peak or one of the slow peaks. Small deviations from Maxwellian were difficult to detect because of the presence of the other peaks in a scattering pattern. Such deviations, if present, would not, of course, alter the analysis of the remaining peaks appreciably. If one assumes a trapping/desorption model for the Maxwellian peak, then the data should look much like the evaporation of an accumulated layer

of ice (at least in the limit where the layer is very thin). The evaporation data of Section 3.3 thus further support the conclusion that the Maxwellian peak is, in fact, Maxwellian at the surface temperature.

The particles in the incident beam giving rise to the Maxwellian peak could be monomers or clusters or both. Mass spectrometer measurements indicate that any particles which are trapped at the surface, regardless of their original size, evaporate as monomers. Some measure of the time scale of this accommodation process can be made by comparing data obtained by chopping the incident beam to data obtained by chopping the scattered stream. The two kinds of spectra are identical (taking into account the changed flight path and the fact that the velocity distribution is that of the incident beam until the particles reach the target). Evidently the residence time for the trapped particles is less than a few microseconds (the smallest time shift observable). Actually, this result should be expected; since molecular vibrations have periods on the order of  $10^{-13}$  seconds, a microsecond is a long time. A practical experiment for measuring residence time must be able to measure such shorter times.

There was one experimental condition where a notable difference was observed between the spectra obtained by chopping the incident and scattered streams. The pair of spectra shown in Figure 25 are for a water beam scattering from a silicon (111) surface at 212° K. In this case, the target was cold enough that most of the beam stuck indefinitely to the surface. The few particles reemitted as a Maxwellian stream after sticking lost correlation with the incident beam (i.e. have resided more than several hundred microseconds on the surface). No intermediate

target temperature range giving a measurable residence time could be found. The behavior appeared to be bimodal. Either particles stuck for a short time before remission, or they stuck for some indeterminate (and random) long time.

The deviations from Maxwellian behavior noted in the early results (Section 3.4.1) can all be attributed to a manifestation of a fast peak which overlaps the fast end of the Maxwellian peak. The signal-to-noise ratio in those data was not high enough to separate the fast peak satisfactorily. Hindsight and a bit of imagination show the peak to be present.

#### 3.4.2.2.2. THE FAST PEAK

The behavior of the fast peak for typical operating conditions is shown in Figures 26<sup>\*</sup> and 27. The major features are a small but measurable decrease in speed from that of the incident beam and a scattering pattern in which intensity increases from the surface normal to the tangent (no well defined lobe), regardless of incident angle ( $0^\circ \leq \theta_i \leq 75^\circ$ ). Furthermore, the fast peak is approximately constant in amplitude for constant "turning angle", i.e. for  $\theta_i + \theta_s = \text{constant}$ .

---

\* In this and all subsequent plots of peak amplitude, the Maxwellian peak amplitude is used for normalization. The detector collimation is such that for angles less than about  $75^\circ$ , the detector sees an infinite target. The Maxwellian cosine distribution is then constant with scattering angle. The flux per unit area on the surface is a function of incident angle, so the Maxwellian peak intensity is not constant for changes in incident angle. By dividing by the Maxwellian amplitude, this variation and any experimental drifts are eliminated. Note that since peak amplitudes and not integrals are used, the ratios do not represent the relative numbers of particles even for constant ionization efficiency.

The velocity loss also varies somewhat with angle and also appears constant for constant turning angle. This peak was observed for all targets at temperatures above the point where virtually all beam particles stick to the surface (around 210° K for typical beam intensities). Even the amplitude and velocity of the peak appear to be independent of target conditions, at least for the cases which have been checked, and this peak is the last to disappear as the target temperature is lowered. Even when nearly everything is sticking a few particles continue to bounce off with little loss of energy.

#### 3.4.2.2.3. THE SPECULARLY DIRECTED SLOW PEAK

A striking feature in the scattering data is the appearance under a fairly narrow range of experimental conditions of a specularly directed slow peak. This peak may dominate a time-of-flight spectrum and vary widely in peak position and amplitude as shown by the examples in Figure 28. If attributed to water monomers, its average velocity would be lower than a Maxwellian at any surface temperature in the system (the coldest being 77° K). The intensity pattern is a lobe at the specular angle (at least to within  $\pm 5^\circ$ ) with a half width of  $20^\circ$  (at least for cleaved Si (111) for which a detailed survey was made). Figure 29 shows this as a plot of the slow peak amplitude versus scattering angle. A plot of stagnation gauge flux measurements for similar conditions is shown in Figure 30. (Since the slow peak can be made to dominate the scattering, the stagnation gauge primarily measures the slow peak amplitude.) Note that the stagnation gauge and flow through ionizer may detect clusters of different efficiencies. The peak shape is non-Maxwellian and, in fact, resembles fairly closely the incident

beam distribution scaled in time by a factor of 2 to 6 (see Figure 31).

The peak varied in amplitude but not in position as a function of scattering angle as expected for lobular scattering. There were pronounced changes in both amplitude and peak position as a function of incident angle (Figures 29 and 32). The peak has not been detected for incident angles less than  $50^\circ$ . The arrangement of the apparatus limited satisfactory data to incident angles less than  $\sim 75^\circ$ .

As indicated in Table 2, some evidence for the specularly directed slow peak was found with all surfaces tested except platinum, and for target temperatures in the range  $210^\circ \text{ K} < T < 300^\circ \text{ K}$ . Below  $210^\circ \text{ K}$ , all particles in the incident beam stick to the target (though as the temperature is lowered, the slow peak disappeared at a slightly higher temperature than the fast peak and Maxwellian peak). The strongest slow peak amplitude was achieved in the range  $240^\circ \text{ K} < T < 245^\circ \text{ K}$  (at least for Si (111)); as the temperature was raised above  $\sim 300^\circ \text{ K}$ , the peak disappeared. The effect of target temperature on the slow peak position (velocity) was relatively small (Figure 33). However, in the available temperature range, temperature could only vary by about 15 % on an absolute scale, so major effects were not to be expected.

The behavior of the specularly directed slow peak as a function of nozzle temperature and source pressure provides the strongest evidence for the importance of large clusters in the beam. The effect can be described in two ways. For constant source pressure of 350 kPa, the slow peak disappears when the nozzle temperature was only  $40\text{-}50^\circ \text{ C}$  above the boiler temperature. For constant nozzle temperature, there

was a threshold source pressure (boiler temperature), below which the slow peak could not be found (see Table 3). Because of the rapid rise in vapor

Table 3. Source Pressure Thresholds for the Appearance of the Specularly Directed Slow Peak

| Source Temperature ( $T_0$ ) | Threshold Pressure ( $P_0$ ) <sup>a</sup> | Relative Beam Flux <sup>b</sup> |
|------------------------------|---|---------------------------------|
| 455° K                       | 350 kPa                                   | 1.0                             |
| 485                          | 550                                       | 1.4                             |
| 535                          | 800                                       | 1.5                             |
| 605                          | 1300                                      | 1.9                             |

a No consistent criterion was used to define threshold. Values good to within about  $\pm 15\%$ .

b Conversion from stagnation gauge pressure versus source pressure measurements. Probably gives a good indication of relative mass flux (see Section 3.2.2 and Figure 13).

pressure of water with boiler temperature, the source pressure threshold for the onset of the slow peak increased approximately as the square of the nozzle temperature, and the degree of superheating necessary to eliminate the slow peak increased also: at 1.3 MPa, a superheating of about 140° C is needed. Note also that for constant nozzle temperature, the fast peak and Maxwellian peak amplitudes rose approximately linearly with source intensity, while the specularly directed slow peak amplitude rose much more rapidly (see Figure 33).

Finally, there is an interesting time dependence in the behavior of the slow peak amplitude. (Only the amplitude was affected in observations

to date.) If a target was heated to  $\sim 400^\circ \text{ K}$  to drive off adsorbed water, cooled to  $240^\circ \text{ K}$ , then exposed suddenly to a glancing incidence beam ( $\theta_i > 60^\circ$ ), it took minutes to hours for the slow peak to reach its full amplitude from a near zero initial amplitude. The process can be accelerated by using a normally incident beam, for which about 15 minutes suffices to achieve steady-state surface conditions. Apparently the slow peak depends on the presence of a surface water or ice layer which forms slowly in a temperature range where a macroscopic layer does not accumulate. (The vapor pressure of bulk ice at  $240^\circ \text{ K}$  causes bulk ice to evaporate much faster than could be resupplied by the beam.) No surface monitoring instruments besides the beam (such as LEED, Auger Electron Spectroscopy, or a quartz crystal microbalance) were available, so one can only speculate on the condition of the surface. Certainly no macroscopic (visible to the eye) ice layers were present.

#### 3.4.2.2.4. THE NON-SPECULAR SLOW PEAK

As source intensities were increased above those used for most of the studies of the specularly directed slow peak ( $P_0 \approx 600 \text{ kPa}$ ,  $T_0 \approx 450^\circ \text{ K}$ ), a new peak was detected in the scattered streams. The main features of this peak were a velocity comparable to that of the specularly directed slow peak and a tangential reemission angle for all incident angles ( $55^\circ \leq \theta_i \leq 80^\circ$ ) (see Figure 34). The peak shape of the time-of-flight spectrum was non-Maxwellian but broader than that of the specularly directed slow peak (see Figure 35). Under conditions where both slow peaks were present, it was difficult or impossible to separate them. Fortunately, there were conditions where each could be studied separately.

Exact intensity thresholds for the appearance of the non-specular



slow peak were not established, but source pressures of at least 1.0 MPa were required, suggesting that this non-specular slow peak is associated with larger clusters.

The peak position as a function of incident and scattering angles (for the range  $55^\circ$  to  $80^\circ$  where detection was possible) is shown in Figure 36. The variation in amplitude is quite large and similar to that of the specularly directed slow peak. Note, that unlike the specularly directed slow peak, there are amplitude variations as a function of both incident and scattering angles, analogous to those of the fast peak.

The non-specular slow peak was found in scattering from silicon, platinum, glass, and covellite. Aluminum and ice were not checked. There were striking variations in its behavior as a function of target temperature (see Table 2). On silicon both slow peaks were detected only below  $280^\circ$  K. On covellite, the non-specular slow peak persists to about  $330^\circ$  K; on glass, the threshold was about  $470^\circ$  K; and on platinum the slow peak showed no sign of extinction at  $585^\circ$  K (no higher temperatures were attempted). On glass there was an observable hysteresis: after heating the target until the slow peak vanished, it was necessary to cool it to near  $273^\circ$  K before the slow peak reappeared. The implication is that there is again a surface coverage effect, though the rank ordering of the threshold temperatures is mystifying.

Finally, it is interesting to note that the non-specular slow peak (and presumably also the specularly directed slow peak, though this was not checked) vanished completely when the inside of the nozzle became partially blocked. The source pressure ratio and nozzle temperature

remained as before, but the reduced intensity evidently reduced the clustering in the expansion from the nozzle.

#### 3.4.2.3. SCATTERING FROM ICE

Nearly all beam particles stuck to the surface for target temperatures where the ice surface was not evaporating excessively. Even when chopping the incident beam, high evaporation rates destroyed the signal, because the local density became high enough for significant gas-phase collisions. With some careful searching, it was possible to find a temperature where a noisy signal was achieved and the fast peak was visible. Chopping the scattered beam, of course, showed mostly simple evaporation. With a bit of imagination it was possible to identify a slow peak under appropriate conditions, but the evaporating particles dominated.

It does not appear likely that it will ever be possible to observe the scattering of water from ice. Possibly a higher intensity source would allow the use of a lower target temperature, but then it would be difficult to avoid high-densities caused by the beam itself. Clearly the ice layers believed to be on the higher temperature targets must be more tightly bound to the underlying substrate than are the surface molecules of bulk ice.

#### 3.4.2.4. MASS-FILTERED VELOCITY ANALYSIS

The mass-filtered version of the time-of-flight equipment is not yet set up to do detailed spatial scans. It can function in two fixed positions, one along the incident beam axis and the other at an angle of  $144^\circ$  from the source target line, thus limiting scattering studies

to a narrow range of angles. Calibration of this equipment (see Section 3.1.3) suggested that it is generally reliable but requires correction for delay. Results obtained from observations of evaporation reinforced confidence in the system.

Results of scattering from silicon under conditions where the non-specular slow peak was present are shown in Figure 37. Signals were found for masses 18, 19, 37 and no higher. This is consistent with our hypothesis that the slow peaks are due to clusters of masses beyond the range of the mass spectrometer. Unfortunately the time-of-flight spectra obtained at low mass (18, 19 AMU) (Figure 37) resemble neither the incident beam (Figure 15) nor the spectra obtained without mass-filtering (Figure 38). Correcting for delay (see Section 3.1.3), one finds that the first peak in Figure 37 probably corresponds to the fast Maxwellian peak in Figure 38. The second peak must be a manifestation of the slow peak in Figure 38, though the peak shape is distinctly different. As shown in Figure 37, this second peak did appear when and only when the source conditions were such that the non-specular slow peak appeared. Without more data at a higher mass range, it is difficult to interpret the monomer time-of-flight spectra in Figure 37. The presence of a slow peak in the monomer time-of-flight spectrum does not necessarily contradict the hypothesis that the slow peak is due to clusters. Monomers could be detached from clusters in the ionizer.

## SECTION IV

### DISCUSSION AND GUIDELINES FOR FUTURE WORK

#### 4.1. HOMOGENEOUS NUCLEATION IN THE BEAM

There is a good deal of interesting information about clusters in jet expansions both in the mass spectrometer and time-of-flight measurements of the beam and in the scattering data. Unfortunately, we are still at the stage where we are using the beam to probe the surface and the surface to probe the beam at the same time, and detailed interpretation of the data is difficult.

It is fairly safe to say that the beam typically consists of clusters of all sizes from monomer out to at least a few hundred molecules. Electron diffraction measurements of beams generated similarly to ours [35-37] indicate that clusters of several thousand molecules may be present under some circumstances. From the magnitude of the slow peaks we observe in scattering, and from the behavior of stagnation gauge intensity and time-of-flight peak amplitude, it appears that, at least for higher incident beam intensities, a substantial portion of the mass of the beam may be in large clusters. It is only possible to construct an approximate cluster size distribution with any data that now exist on cluster beams (see Section 3.1.1). One can still draw some conclusions about the behavior of clusters in two size ranges: (1) clusters less than 50-100 molecules, where most molecules reside on the surface and few in the bulk (consider, for example, a simple cubic structure of  $5 \times 5 \times 5 = 125$  molecules: 98 are surface molecules, and only 27 are bulk), and (2) clusters near the critical nucleus size for homogeneous nucleation, thought to be around 35-1000 molecules for water [9,10]\*.

---

\* The notion of a critical nucleus is that clusters of lesser size tend to shrink on the average, while clusters of larger size tend to grow. Theor-

The information about the smaller clusters is derived from mass spectra (Figure 12, for example) and mass-filtered velocity analysis (Figure 15).

No clusters within the range of the mass spectrometer ( $n < 75$ ) of more than 2 or perhaps 3 molecules survive any collision with a surface.\* They are apparently fully destroyed and reemitted as monomers. They do, however, survive, at least in part, the collision with a 70 eV ionizing electron or perhaps a free proton. If electron impact is the ionization mechanism, at least an  $\text{OH}^-$  must be detached leaving a free proton in the cluster. The attachment of a proton traveling at low velocity relative to the cluster (glancing collision: the protons, being formed from beam particles, move with the beam) could also be the ionization mechanism. In either case, the proton might stabilize a cluster by interaction between it and the water dipole moments. The charged clusters clearly do survive 2 kV acceleration in the rf fields of the quadrupole to form the mass spectra we observe (else we would see no clusters).

One charge center may stabilize a cluster, but two may destroy it. The repulsion between the two charge centers may tear a small cluster apart. This might explain the absence of double-ionization peaks (see et al. values for the size of the critical nucleus calculated thermodynamically by considering the balance between surface and bulk energies of the growing cluster in a quasiequilibrium system (a bad approach for very small clusters). The actual value depends on temperature and the "super-saturation ratio" (the ratio of the actual pressure to the pressure at which solid and vapor would be in equilibrium at the system temperature). One must use some care in extending the notion of critical nucleus to the highly non-equilibrium conditions in a nozzle beam and to beam-surface collisions.

\* More precisely, we have not observed any clusters in the scattered stream. While we have not surveyed all possible  $\theta_i$  and  $\theta_s$ , nor looked for scattered particles out of the principal plane, we have looked at near tangential  $\theta_i$  and  $\theta_s$  where we would expect cluster survival to be most favored. (The normal component of momentum is smaller for large  $\theta_i$ , and one would expect the normal component to be the determining factor for cluster survival/destruction.)

Section 3.2.3) in the mass spectrum below  $n = 18\frac{1}{2}$ . Either clusters larger than  $n = 37$  are more stable, or the charge centers are more effectively shielded from one another.

All small clusters travel with nearly the same velocity. The simplest explanation for this observation is that the larger clusters are swept along by the monomers. This explanation fails, because it also predicts that all clusters should have the same temperature, which is contrary to our results (Figure 18). The clusters could be formed by glancing collisions between molecules and clusters having very nearly zero relative velocity (both directed and thermal translational).

A plausible model can be constructed from the data on the variations in the velocity distribution of small clusters of different  $n$  values. Consider first the energetics of cluster formation. We start with monomers at  $P_0$  and  $T_0$  in the source. Their available energy (ignoring viscous losses in the nozzle) is the enthalpy of the source gas,  $c_p T_0$ . We have detailed mass-filtered time-of-flight data for clusters in the beam for only one source condition:  $T_0 = 458^\circ \text{ K}$ . At this temperature rotational modes in water are fully excited and vibrational modes are not. The internal energy per molecule,  $u$ , is thus  $\frac{3}{2}kT_0 + \frac{3}{2}kT_0 = 3kT_0$  (translational and rotational). The enthalpy per molecule,  $h = u + Pv$  ( $= u + kT_0$  for an ideal gas) is thus  $h = 4kT_0$ . Tabulated values for  $c_p$  [59], actually give  $h = 4.17 kT_0$  at  $T_0 = 458^\circ \text{ K}$ .

We begin by assuming that each cluster of  $n$  water molecules is formed from a group of monomers each of mass  $m$  which interact only among themselves. The energy balance for this process can be written as

$$n4.17kT_0 = \frac{1}{2}(nm)u^2 + E_{tr} + E_i + E_f \quad (4.1)$$

where  $\frac{1}{2}(nm)u^2$  is the kinetic energy of the directed motion of the cluster,  $E_{tr}$  is the additional energy associated with thermal translational motion,  $E_i$  includes all other thermal energies (rotation and vibration), and  $E_f$  is the energy of formation of the cluster.

We measure  $T_0$ ,  $u$ ,  $E_{tr}$  and  $n$  (see Figures 16-18), while  $E_i$  and  $E_f$  are unknown. Note that since velocity distributions for small clusters ( $3 < n \leq 50$ ) are all nearly Maxwellian and have half-widths which are nearly independent of  $n$  (Figure 15), the apparent translational temperature,  $T_{tr}$ , is proportional to  $n$ ; i.e., the fitting of the same translating Maxwellian velocity distribution,  $v^2 e^{-M(v-u)^2/2kT_{tr}}$ , to all the data of the type shown in Figure 15 implies that the exponential is constant. Since  $M = nm$ , we must have  $T_{tr} = nT_c$ , where  $T_c$  is a temperature we shall refer to as the "cluster temperature". We clearly do not have an equipartition of thermal energy in the cluster beam. We have no way of predicting, then, how much energy,  $E_i$  is contained in internal modes. One can speculate that internal modes will be populated according to a temperature  $T_c$  ( $nT_c$  would destroy a sizeable cluster), but one needs to postulate a cluster structure to count available modes, anyway, and we are not yet in a position to do so. One way to explain the apparent variation in  $T_{tr}$  with cluster size is to postulate that clusters are formed only from monomers moving together with virtually no relative motion, i.e., monomers whose directed velocities and thermal translational velocity are within the same narrow range. The thermal motion of a cluster would then be determined by a coherent addition of the monomer motion rather than the more typical incoherent (random) addition. This implies a

very weak binding energy for the clusters (insufficient attractive force to pull together molecules with significant relative motion), a notion which is supported by the observed vulnerability of clusters to impact (see Section 3.4.2.4). It might be more appropriate to think of the width of the velocity distribution as arising from a statistical spread in the directed velocity rather than from residual thermal motion.

Accordingly,  $E_{tr} = \frac{3}{2}k(nT_c)$ , and we have

$$\frac{E_i + E_f}{n} = 4.17kT_0 - \frac{3}{2}mu^2 - \frac{3}{2}kT_c. \quad (4.2)$$

$T_0$ ,  $u$ , and  $T_c$  can be obtained from the data, hence everything on the right hand side is known. We can thus calculate a sort of potential energy per molecule (consisting of internal energy and bond energy) as a function of  $n$ .

In order to determine  $u$  and  $T_c$ , we must set a time origin for the mass-filtered time-of-flight spectra. Insofar as the absolute time origin is uncertain, we must be cautious in assigning absolute values to  $u$  and  $T_c$ . It is reasonable at this point to postulate that the mass spectrometer introduces a constant delay to the velocity spectra which is greater than zero (see Section 3.1.3). On inspection of the spectra of Figure 15, it seems reasonable to match the peak position of the larger peak in the monomer time-of-flight spectrum to the peak of the spectrum without mass-filtering (Figure 15a). This is also the peak position of the time-of-flight spectra for  $n \geq 15$ , so the largest part of the mass of the beam probably has this peak velocity. This match gives a delay of 157  $\mu s$ , which is both the best estimate and a maximum reasonable value (all other peaks appear at shorter time).



Table 4 gives values for  $\frac{E_i + E_f}{n}$ . For comparison, note that  $\frac{E_f}{n}$  for bulk ice is about -580 meV/molecule. The main effect of an error in the time origin determination would be just to shift all values of  $(E_i + E_f)/n$  by a constant amount. The trend would still be in the same direction: larger clusters more weakly bound than smaller clusters (for  $n \leq 40$ ).

Particularly disturbing, though, is the negative value for  $E_i + E_f$  for  $n = 1$ .  $E_f$  for a monomer is zero by definition. The extra energy for monomers is probably a result of collisions between monomers and the larger clusters, which we have neglected to consider thus far. The formation of the bond involved in the growth of the larger clusters may well require the presence of a third body to remove some excess energy, so it is not reasonable to neglect such processes.

The amount of energy exchanged between monomers and clusters of a particular size,  $n$ , cannot be found. Now, instead of writing an energy balance for a single cluster, the best we can do is to write an energy balance for the system as a whole. Equation 4.2 must be rewritten as follows:

$$\sum_n A_n \frac{E_i(n) + E_f(n)}{n} = 4.17kT_0 \sum_n A_n - \sum_n A_n \frac{1}{2}m[u(n)]^2 - \frac{3}{2}kT_c \sum_n A_n \quad (4.3)$$

where  $A_n$  is the number of clusters of size  $n$  and  $\sum_n nA_n$  is the total number of molecules. This expression would give us a weighted average of the potential energy per molecule, provided we could determine the  $A_n$ 's with reasonable accuracy. One may be able to determine the  $A_n$ 's with sufficient accuracy by using the corrected peak heights from the mass spectrum. To obtain useful information in this way requires more data

Table 4. Values of  $(E_i + E_f)/n$  <sup>a</sup>

| $n$ | $\frac{E_i + E_f}{n}$ |
|-----|-----------------------|
| 1   | -202 meV/molec        |
| 2   | -177                  |
| 3   | -146                  |
| 4   | -120                  |
| 5   | -97                   |
| 6   | -97                   |
| 7   | -80                   |
| 8   | -80                   |
| 9   | -80                   |
| 10  | -62                   |
| 11  | -62                   |
| 12  | -65                   |
| 13  | -65                   |
| 14  | -65                   |
| 15  | -51                   |
| 16  | -51                   |

<sup>a</sup> Calculated from equation 4.2 using data of Figure 15.

cf. binding energy of water in bulk ice = 580 meV/molec

with different distributions for  $A_n$  (different  $T_0$  and  $P_0$ ). Using such data it might be possible to make some interesting statements about  $\frac{E_i + E_f}{n}$  as a function of cluster size. Of course, it would be very useful to resolve the time origin problems and extend the useful mass range of the mass spectrometer.

Perhaps a more fruitful approach is to look directly at the  $A_n$ . In the range of cluster sizes (below the critical nucleus size) which have had sufficient opportunity to grow and diminish by collision (this might include all but the largest clusters in the beam at any particular source conditions), one might expect the number,  $A_n$ , of clusters of size  $n$  to be distributed as a function of the energy of formation,  $E_f$ , according to

$$A_n = A_1 e^{-E_f/kT} \quad (4.4)$$

Probably, the appropriate temperature is  $T = T_c$ . One can thus obtain  $E_f(n)$  directly from the  $A_n$ . Furthermore, one can attempt to fit  $E_f(n)$  to a function of the form

$$\frac{E_f}{kT} = -An^{2/3} + Bn \quad (4.5)$$

where  $A$  represents the surface energy per molecule of a cluster, and  $B$  represents bulk energy. This would be the first experimental determination of  $A$  and  $B$ . Note that one also obtains a measure of critical nucleus size from  $A$  and  $B$ :  $n_c = (\frac{2}{3} \frac{A}{B})^3$ . Such a fitting is shown in Figure 12. We obtain  $A=1.56$ ,  $B=.29$ , and  $n_c=46$ . Note that these energies are an order of magnitude smaller than those obtained by assuming bulk crystalline values. [10] See Appendix E for a discussion of the effect of mass spectrometer amplitude correction factors on this fitting. It would be desirable to collect data for a variety of source conditions, of course, and we are

still in the process of refining this approach.

The anomalies in the mass spectrum must also contain potentially useful information about the smaller clusters. For  $n \leq 40$ , say, there is no reason to expect clusters with bulk ice structure. Indeed, one theory [6,10] suggests a variety of other more likely (or energetically favorable) structures. The differences in free energy between these structures and those of bulk ice are not large, and alternate structures may, in fact, coexist. The feature at  $n=21$  has now been observed by several groups [32-34]. One proposed structure [59] is a regular dodecahedron (20 vertices) with a water molecule trapped in the center. Only a small distortion of the tetrahedral bond angle of hexagonal ice is necessary ( $108^\circ$  instead of  $109^\circ 28'$ ). The apparent dip in the mass spectrum for clusters of 22-24 molecules can also be explained by postulating that at least some of these structures are unstable compared to the simple clathrate and lose molecules to achieve  $n=21$ . Our model of weakly bound clusters is not consistent with this picture, however, and we do not yet have a satisfactory alternative.

The feature at  $n=30$  has not been previously reported, but is quite reproducible. We have no good explanation for its presence.

For homogeneous nucleation, the main interest in cluster structure is to establish the range of contributing configurations and the paths among them. From the point of view of nucleation and growth of macroscopic crystals, the most critical events take place at cluster sizes close to the critical nucleus size. With clusters of smaller size, it is only important to know that there are no important barriers to stable nucleation or phenomena which affect the macroscopic nucleation

rate. The 20 or 21 molecule clathrate structure is potentially such a barrier, but present experimental evidence suggests that the effect is small. Perhaps the clathrate structure cannot even become a critical nucleus, but must first break up and re-form in another configuration, in which case, it is not important unless it ties up a significant amount of mass.

Detailed information about large clusters is even more difficult to obtain. Specially designed mass spectrometers have approached the ten thousand molecule mark for  $H_2$  and  $H_2O$  [34,39,43], but mass spectrometry in this size range is difficult. Our instrument has been extended to  $(H_2O)_{37}$  (or  $(H_2O)_{75}$ , if half-order peaks are interpreted as due to double ionization). Electron diffraction measurements [35-37] are useful for the larger  $n$  values, but are limited in the sort of information they provide. It appears that nearly all large water clusters formed in nozzle expansions have the cubic structure of ice Ic (from bulk studies [60], this implies an effective temperature at formation of about  $100^\circ$ - $150^\circ$  K.). However, only rough estimates of average cluster size can be obtained, and it is not possible to track the growth of a cluster.

Our data provides two indirect clues about the behavior of large clusters. First the monomer velocity distribution undergoes a dramatic change (becomes bimodal) when a certain source intensity (size of cluster) is reached. At present, this phenomenon is poorly understood, but one can speculate that some significant event takes place when some large cluster size is achieved. Similarly, since the slow peaks in the scattering data appear to involve the scattering of large clusters, while small clusters simply do not survive collision with a surface, there seem to

be two transitions in the scattering behavior as a function of cluster size. Some or all of these transitions could be related to the critical nucleus size. Clusters larger than the critical nucleus size are more stable with respect to gas phase collisions, and one might expect them to be more stable with respect to impact as well. There are some exciting possibilities for studying critical nuclei, if these speculations can be substantiated. Some means must be found for monitoring cluster size; extending the range of mass spectrometry is probably still the most promising approach.

#### 4.2 EVAPORATION AND DETAILED BALANCING.

The usual theoretical argument for the inference that the velocity and spatial distribution of particles evaporating from a surface is Maxwellian is as follows: Consider a solid in equilibrium with its vapor. The vapor may consist of clusters as well as monomers. (Most discussions of evaporation treat the vapor phase as monomers. At least one other group [61] has definitely identified small clusters in evaporation from metals.) In equilibrium the vapor and solid are at the same temperature. The vapor has Maxwellian velocity distributions associated with each cluster size. The surface is neither growing nor shrinking, so detailed balancing requires that any particles which stick to the surface must be exactly balanced by particles leaving the surface. Furthermore for equilibrium to be maintained, every dynamic process must be accompanied by its inverse. Monomers and clusters in the gas phase have a Maxwellian distribution. If these are incident on the surface, they must leave the surface in a cosine spatial distribution with a Maxwellian velocity distribution at the surface temperature. Since the incident stream is

independent of the evaporating stream, if the vapor is removed, and particles no longer strike the surface, the evaporating particles should still retain the equilibrium properties. How then can one explain observed deviations from this behavior?

The answer is that the detailed balancing argument is not strictly valid. In equilibrium, the argument is sound, but the extension to non-equilibrium is not necessarily valid. For example, as soon as collisions between evaporating molecules become likely (when the stream density becomes high enough), equilibrium arguments fail. If there are gas phase collisions only between molecules leaving the surface and not between these molecules and those of an incoming vapor, there is no reason to expect equilibrium arguments to work, and a specific kinetic model must be constructed. This problem could apply to all the data for higher target temperatures (Section 3.3, Figure 22). It does not necessarily imply that the higher temperature data are of no interest, however. Rapid non-equilibrium evaporation is a common occurrence, and its study is also interesting.

#### 4.3. MONOMER SCATTERING

We consider here the possibilities for the contribution of monomers to all the features of the time-of-flight scattering data (Section 3.4.2.2). The Maxwellian peak was discussed in Section 3.4.2.2.1. A plausible explanation was presented involving processes of trapping/desorption. We attribute the fast peak to the scattering of monomers, but we must also consider possible mechanisms whereby monomers might give rise to the slow peaks.

#### 4.3.1. THE FAST PEAK

The properties of the fast peak were presented in detail in Section 3.4.2.2.2. We believe this scattering feature to be the same as that reported by Hurst et al [62] for heavy inert gas scattering from metals. They used only grazing incident angles, and interpreted the scattering as specular. Our observations show some rather unexpected properties. Roughly speaking, the scattering appears to be almost elastic in velocity space, but inelastic in coordinate space. Figure 39 shows incident and scattered velocity components. Note that neither normal nor tangential momentum is conserved. There are, in fact, regions where there is a gain of either normal or tangential momentum. The total scattered velocity is always less than the incident velocity, so there is a net loss of total momentum. There is, of course, no problem of total momentum conservation: the extra momentum is either gained or lost by the surface. However, most simple interaction models that have been developed to explain classical scattering in the thermal regime[63] cannot explain any gain of momentum components (unless the surface is much hotter than the beam). Most models require tangential momentum conservation and allow for either gain or loss of normal momentum.

A simple explanation which addresses itself to all the features of the fast peak is as follows: Referring to Figure 26, note that, to within experimental accuracy at least, the (normalized) amplitude of the fast peak is constant for constant "turning angle" ( $\theta_i + \theta_s$ ). For example, the amplitude at  $\theta_s = 75^\circ$  for a beam incident at  $\theta_i = 65^\circ$ . An amplitude pattern of this sort could be generated by specular scattering from a rough surface. All surfaces used in this study (see Table 2) can be expected to be rough



on the scale of a single water molecule. Even an optically smooth surface need only be smooth down to a scale of about 1000 Å.

For any given incident angle (relative to the average surface normal), a full range of local surface orientations could present themselves to an incoming molecule from the beam. Molecules which scatter specularly relative to the local surface normal would be found at any scattering angle relative to the average surface normal. One need only add the hypothesis that molecules which scatter specularly do so as a function of (local) incident angle, and a complete match to the amplitude data is obtained. A Debye-Waller attenuation may be adequate to formalize this relationship.\*

To explain the small loss in velocity, then, we need only invoke a small energy exchange as, for example, from the hard cube model. Then normal velocity/momentum loss manifests itself as greater velocity loss small turning angles.

The data are not sufficiently accurate to warrant detailed numerical comparison. There are a couple of predictions which could be tested, for which data have not yet been taken. Scattering outside the principal plane should also show the fast peak. The peak amplitude should be constant for a constant angle between the vectors associated with the incident and scattering direction. (Note, that this is no longer equal to the sum of the incident and scattering angles.) If a surface can be polished smooth to the scale of a water molecule, real specular scattering should occur. This may not, in practice, be possible, especially when a surface layer of ice is present (such a layer would probably be patchy

\* A study of this possibility is under way with Nicolas García, but the results are not yet ready for presentation.

and rough).

#### 4.3.2. THE SLOW PEAKS

We have ascribed the slow peaks in the time-of-flight spectra to the scattering of clusters from the surface. There is good evidence that this hypothesis is reasonable (see Sections 3.4.2.2.3 and 3.4.2.2.4), but without positive identification of clusters in the slow peaks, one should not rule out the possibility of monomer scattering.

The scattering cannot involve any sort of thermal equilibration: if the particles are monomers, neither the target nor any surface in the entire system is cold enough to produce the observed velocities. Hence for monomers, the scattering would have to be direct scattering with an attendant kinetic energy loss. The energy can either be lost to the surface (via surface phonon creation) or to internal modes of the water molecule (either rotation or vibration). The observed energy loss is about  $2 \times 10^{-20}$  J/molec. There is a strong peak in the bulk phonon spectrum of ice at about  $1.3 \times 10^{-20}$  J/molec[2]. Of the possible vibrational modes, the only one close is the OH stretching mode at about  $6.5 \times 10^{-20}$  J/molec.[2] Rotational modes are excited at about  $1.7 \times 10^{-20}$  J/molec.[2] Both translation-rotation transfer and phonon creation thus appear plausible. Where these explanations fail most seriously is in the behavior of the slow peaks as a function of nozzle temperature for constant source pressure. There is a sharp cut-off in the slow peak amplitude for fairly small (<10%) increases in temperature (see Section 3.4.2.2.3). This is reasonable if there is a resonance, but a corresponding low energy cut-off cannot be found. An explanation in terms of clusters appears much more promising.

#### 4.4. CLUSTER SCATTERING

Small clusters (less than 75 molecules) apparently never survive collision with a surface (see Section 3.4.2.4). Above some critical size, possibly in the neighborhood of 1000 molecules, it is plausible to assume that some fraction of the clusters survive, at least in part, and give rise to the slow peaks. The non-specular slow peak apparently requires even larger clusters than the specular slow peak (see Sections 3.4.2.2.3 and 3.4.2.2.4)

Constructing a convincing model of cluster scattering to explain the observed features is a formidable task. There are many possible mechanisms to consider. The cluster may scatter intact, fragment, or lose a few surface molecules. It may change structure substantially and/or have internal modes excited. Clusters and monomers present on the surface may play an important role. One can imagine a sputtering process where the incoming cluster knocks material loose from the surface. In any case, the nature of the surface is, at present, largely unknown. There may be a layer of water/ice one or more molecules thick. Such a layer might be significantly deformed on collision with a cluster even if sputtering does not take place. At the present limited state of knowledge about the system, any model will be necessarily somewhat ad hoc, and it would be difficult to decide on reasonable approximations to create a numerical model. There are, nevertheless, some things which can be said in general terms about the scattering.

First, it should be noted that the scattering of water clusters from surfaces appears to be quite different from the scattering of nitrogen, helium, and hydrogen clusters (see Section 1.3)[44]. Neither of the two

types of scattering observed with these other species has features similar to those of the slow peaks observed for water. The model proposed to explain one of the scattering patterns for hydrogen and helium [44] involved the concept of evaporative recoil: some molecules from the surface of the cluster evaporate and leave the surface; conservation of momentum requires that the cluster gain momentum in the opposite direction. The problem with this explanation is that the "evaporation" from the cluster must take place during contact with the target, and the evaporating molecules probably end up on the target and do not necessarily carry away any momentum. In any case, such a model does not predict the features observed in the water scattering data.

Consider what we do know about the scattering: The incoming clusters are cold (probably  $50^{\circ}$ - $150^{\circ}$  K) and moving very fast for their size (nearly as fast as the monomers). We need to explain two kinds of behavior. The clusters lose much of their initial velocity and either come out at the specular angle or near the tangent. These two cases are considered separately.

The appearance of a scattering maximum at the specular angle is startling in any "classical" scattering system. In addition we have just explained the absence of specularly directed scattering for the fast peak (Section 4.3.1) by postulating a rough surface. A rough surface for monomer scattering could appear smooth for cluster scattering, though, if the scale of roughness were in between the size of a monomer and the size of a cluster. We have also considered a model where there is total momentum in the locally normal direction on a rough surface. Such models produce a near-specular reemission angle, but it does not (for any way) a lobe of the sort observed, and does not

account for sufficient loss of total momentum.

Returning to the smooth surface (for cluster scattering) hypothesis, we have considered a couple of other models. A rough analogy to the observations is the bounce of a very soft rubber ball. The ball is so weakly held together that it fragments for incident angles less than  $50^\circ$ . For larger incident angles, it survives collision but loses much of its translational kinetic energy. The loss mechanism might be conversion to thermal motion via vibrational deformation of the cluster and/or the surface, or perhaps the energy could go into breaking some of the bonds of the cluster resulting in some loss of mass. Such a process might explain the intensity variations with incident angle. From the mass spectrometry data, it appears that a wide range of cluster sizes must contribute to the slow peaks. Perhaps clusters of smaller and smaller size survive collision with the surface as incident angle is increased. Detailed mass analysis with a mass spectrometer of sufficient range might verify such a behavior. In any case, the equal loss of normal and tangential momentum must be accounted for.

The non-specular slow peak evidently has quite a different scattering mechanism. Almost all of the normal momentum of the incident cluster is lost. A large fraction (50-80%) of the tangential momentum is lost as well. A rough surface explanation is of no use (comforting if one believes the non-specular slow peak to involve the largest clusters). Again a detailed mechanism can be only guessed at. One might envision a cluster almost sticking and then rolling or bouncing/hopping along the surface until it just happens to get enough energy to escape the attractive potential well and goes skimming off near the surface. It is certainly

remarkable that these clusters can survive collision with a hot surface. The variation of threshold temperatures among targets is quite baffling. What changes can be taking place on the surface at threshold. A water monolayer is the most obvious explanation, but what role does it play?

The immediate directions for further study of cluster scattering include the following: Mass analysis (or more precisely, mass-filtered velocity analysis) of the slow peaks needs to be accomplished. This will involve a very high mass range mass spectrometer, but as long as individual mass peaks can be resolved (and for time-of-flight work even if they cannot), mass resolution can be sacrificed for range. Some other means must be found for monitoring the condition of the surface. Helium scattering or LEED would probably be most useful. Auger Electron Spectroscopy or a quartz crystal microbalance are other possibilities. There is probably useful information to be gained from other surfaces as well; we still do not know what surface features are important.

APPENDIX A. TIME-OF-FLIGHT ANALYSIS BY THE PSEUDORANDOM CHOPPING TECHNIQUE:  
CALIBRATION AND APPLICATION TO MASS SPECTROMETRY

This appendix contains a copy of a paper [53] presented at the 11th Rarefied Gas Dynamics Symposium (July, 1978, Cannes, France). It was not included in the published proceedings (due to a disagreement over whether it contained any "new" material), and is therefore reproduced in full here. It contains its own figures and references.

Time-of-Flight Analysis by the Pseudorandom Chopping Technique:  
Calibration and Application to Mass Spectrometry

David D. Dreyfuss,\* Robert B. Doak,+ Harold Y. Wachman<sup>††</sup>

A time-of-flight apparatus utilizing a cross correlation chopper for beam modulation has been calibrated against a Maxwellian stream. A consistent and reliable scheme for determining the time origin, to  $\pm 5 \mu$  sec for any arbitrary time-of-flight wave-form has been devised. It is also shown that the need for deconvolution over shutter function is virtually eliminated, since with this scheme it is possible to work in principle with an arbitrarily narrow width of unit slot. A relatively simple and straightforward analytical procedure for deconvoluting the modulated signal is described.

---

\* Present Address: Dept. of Aeronautics & Astronautics, M.I.T., Cambridge, MA

+ Present Address: Aerodyne Research, Burlington, MA, USA

<sup>††</sup> Professor, Dept. of Aeronautics & Astronautics, M.I.T., Cambridge, MA, USA



## 1. Introduction

In 1966 we reported [1, 2] from this laboratory, on the calibration and performance of a time-of-flight (TOF) apparatus (fig. 1) in which the shutter consisted of a single rotating disk having four narrow slots of equal widths located at 90° intervals around the rim. The detector consisted of an electron beam ionizer which (ideally) produced a sheet of electrons, which ionized the molecular stream at a plane. The ions were drawn out of the stream and collected on an electron multiplier.

There are several limitations to this scheme. The time resolution of the apparatus is determined by the ratio of the open to closed arc segments around the disk (the chopping period, which is the sum of these two lengths, is fixed by the need to prevent overlap of fast molecules from one pulse and slow molecules of the previous pulse). To obtain good time resolution, one uses a narrow slot. It is, in principle, possible to deconvolute from the effects of a wide slot (shutter function), but the mathematical manipulations involved are very sensitive to the magnitude of the noise in the data. In practice, if the shutter function is broad enough to distort the TOF waveform, then the best that deconvolution provides are the lowest order moments of the velocity distribution represented. Usually, in the past, it was found necessary to sacrifice information on velocity, and use a wide enough slit to transmit a sensible signal in each pulse.

The ionization detector has its own limitations. An electron beam ionizer is a universal detector, hence is usable for all molecular species in the test stream. As a consequence, however, background molecules are detected as well (in particular, with permanent gases, all those stream

molecules which strike closed portions of the disk are detected as background). Statistical fluctuations in this background are usually the major source of noise in the TOF data. Other detector problems include the finite extent of the ionization region along the beam direction and non-zero ion travel time between the instant of ionization and detection. The extent of the ionization region does not present a serious problem because it has only a second order effect on the TOF distribution (the finite shutter function is a first order effect). We have shown [3] that a considerable flight path through the ionization region (up to about 25% of the total flight path) can be used before appreciable distortion in waveform occurs, and we have taken advantage of this to improve the efficiency of ionization. As to the effects of the ion travel time, it can be made insignificant with sufficient draw-out potentials or alternatively it can be accounted for in interpreting the data.

## 2. Pseudorandom Chopping

An alternative approach to molecular beam chopping, which avoids many of the problems cited above is to use a pseudorandom chopping scheme (fig. 2). This technique was originally developed in connection with thermal neutron studies [4-7], and has only recently been used with neutral molecular beams [8, 9]. In comparison to the scheme described above a larger number of pulses of molecules are produced over each revolution of the disk. As a consequence several pulses are produced

within each chopping period, which overlap at the detector. By spacing the pulses "randomly" within the period, it is possible by a simple arithmetic procedure to undo the overlap produced [3, 9]. It is possible, in fact, to attain a duty cycle of 50% for such a chopper independent of individual slot width. With this chopper, the time resolution is determined by the length of the pseudorandom chopping sequence, where "length" counts the total number of unit slot widths (note that several adjacent locations may be open, thus forming a single larger slot which is treated as a set of unit slots). The deconvolution procedure recovers the waveform which would be obtained from a chopper with a single unit slot per period. While it is conceivable, in principle, to improve time resolution arbitrarily by taking longer and longer sequences, in practice, limitations in electronic response time and the need to have unit slot width compatible with molecular beam width precludes this extension. Avoiding these problems by using larger diameter disks will cause other experimental difficulties. (Given an electronic chopping scheme of some sort (e.g. chopping laser excitation of a beam), this last limitation may not apply, since chopping could be entirely independent of collimation, and even better time resolution might be obtainable.)

### 3. Calibration

Although the pseudorandom chopping technique has been demonstrated for molecular beams, to our knowledge, no calibration of a system using the technique has been reported. We have performed such a calibration against inert gas Maxwellian beams. A schematic diagram of the apparatus is shown in figure 3. A room temperature gas reservoir at a pressure on

the order of 10 Pa supplies a beam through a small hole in a thin stainless steel wall. In operation, conditions were such that adequate signals were achieved for a source Knudsen number,  $Kn \sim 1$ . Flow at this value of  $Kn$  is perhaps not fully molecular (one would like to use  $Kn \approx 100$ ), but it appears adequate for velocity distribution measurements from comparison of velocity distributions for a series of decreasing source pressures which indicates no measurable change in distribution when values of  $Kn \geq .1$  are used.

Some examples of calibration runs are shown in figure 4. To compare the data with the known velocity distribution of the gas in the source, a least square fit of a Maxwellian velocity distribution to the data was made. Source parameters such as molecular weight and temperature which are known or independently measurable were held fixed. Fitting parameters were a baseline position (baseline information is lost experimentally because the signal is superposed on a large DC background), and an overall amplitude factor. The distribution is linear in these quantities, so the fitting is straight-forward and well-defined. It avoids the hazards of peak height matching in that it weights all data points equally, and can be used for comparison with moderately noisy data. Also it is readily extended to gas mixtures, which should have a velocity distribution consisting of a weighted sum of two different Maxwellians.

#### 4. Time Origin Considerations

One parameter important to comparison of the data with Maxwellian theory, which has not so far been mentioned, is the location of the time origin in the TOF waveform. Physically, this is the time at which all

molecules represented by the TOF waveform passed the chopper. Because of the sharp leading edge of the Maxwellian TOF waveform, small differences in time origin (less than one channel (slot) width or 15  $\mu$ sec) are readily detected. In making a calibration it is especially important that the time origin be fixed independently, and not determined by matching peak locations or the leading edge or by some similar scheme.

In principle, the time origin is easy to determine. Using a photo-trigger reference, whose position relative to the beam position is measured, time origin can be determined in terms of some constant number of channels. Time delays associated with either ion drawout time or electron signal processing, are essentially constant, and may also be assessed. It is difficult, however, to measure these delays independently with sufficient precision. It seems best to measure them for the composite apparatus. Of the several schemes attempted, the following appeared the most satisfactory.

Using the complete system with molecular beam and all processing electronics in place, electronic delays were determined from background gas detection without the chopper. For this process the electron accelerating grid in the ionizer was pulsed electronically, and the time delay from the electronic pulse to signal rise was measured. To determine geometric timing relationships, a series of TOF spectra were measured for a constant intense signal. (The stream was not necessarily Maxwellian: we used a fairly high pressure  $H_2O$  beam for which we could obtain an excellent signal-to-noise ratio.) These TOF waveforms were produced by rotating the chopper both "forward" and "backwards" (the relative location of the photo-trigger and molecular beam define directions). Then the relative location of some

known feature (e.g. peak position) for the two resulting waveforms were compared to give a measure of the geometric timing relationship which is independent of electronic delays. Improved precision in the measurement can be obtained by making the measurement at several chopping frequencies. We have been able to locate the time origin to within about  $\pm 1/3$  channel (typically  $\pm$  a few microseconds for our operating chopping period of 1-2 msec and pseudorandom sequence of length 103) using these techniques.

#### 5. Applications to Mass Spectrometry

One possible application of the improved resolution TOF system we have developed is to mass spectrometry (see fig. 5). As mentioned above in connection with the fitting of theoretical curves to the data, it is possible to obtain a measure of the relative amounts of gases in a gas mixture by comparing amplitude of the fitting Maxwellians. The advantage of the technique is that it is non-destructive, in the sense that ionization takes place only after the necessary information (time of flight between two fixed points) has been obtained. There are difficulties, however, because the velocity distributions for the species to be separated must be known independently. This information is available, *a priori* only for free molecular flows. If Maxwellian velocity distributions must be used, only a few fairly widely spaced molecular weights can reasonably be separated since the separate TOF peaks are broad and overlapping. In some experimental situations, for example, detection of dimers and higher order clusters in near condensing systems, the advantage of non-destructive sensing may outweigh the disadvantages cited.

#### REFERENCES

1. P. B. Scott, "Molecular Beam Velocity Distribution Measurements"  
M.I.T. Fluid Dynamics Research Lab. Report 65-1, Cambridge, MA, (1965).
2. P. B. Scott et al., in RGD (C.L. Brundin ed.) p. 1353, Academic Press  
New York, (1967).
3. David D. Dreyfuss, "Neutral Time-of-Flight Mass Spectrometry,"  
SM Thesis, M.I.T., Cambridge, MA (1977).
4. T.E. Stein, et al., J. Nuc. Energy A/B 16, 499 (1962).
5. K. Sköld, Nucl. Instr. and Meth. 63, 114 (1968).
6. A. Virjo, Nucl. Instr. and Meth. 73, 189 (1969).
7. W. Gläser and F. Gompf, Nukleonik 12, 153 (1969).
8. V. L. Hirschy and J. P. Aldridge, RSI 42, 381 (1971).
9. H. D. Meyer, Max Planck Inst., Göttingen Bericht 113 (1974).

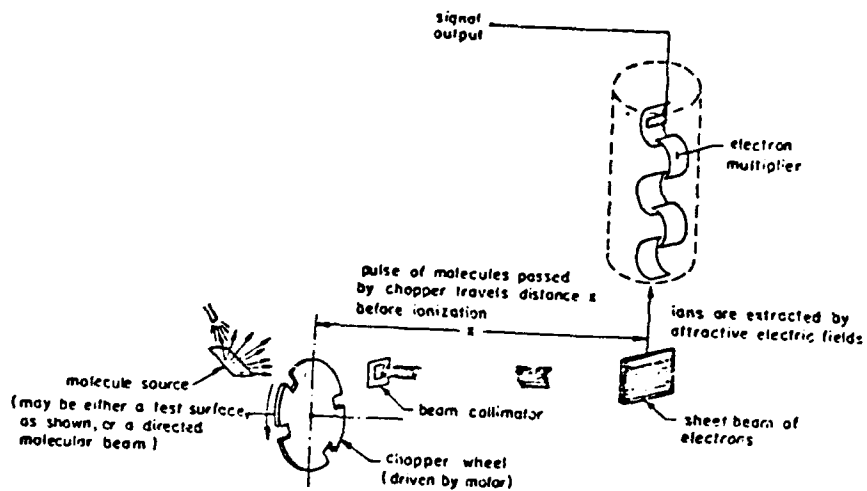


FIGURE 1  
Typical TOF Apparatus

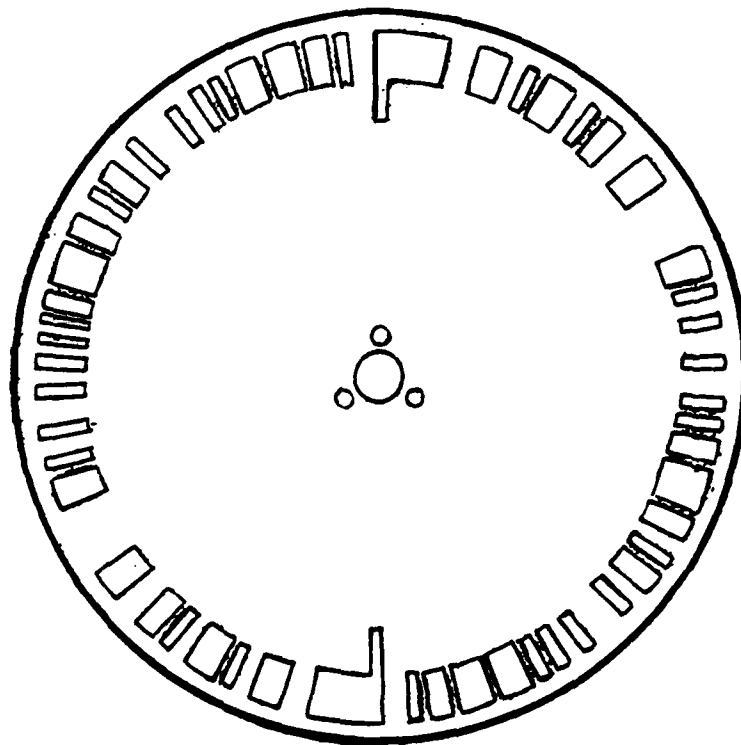


FIGURE 2  
Pseudorandom Chopper



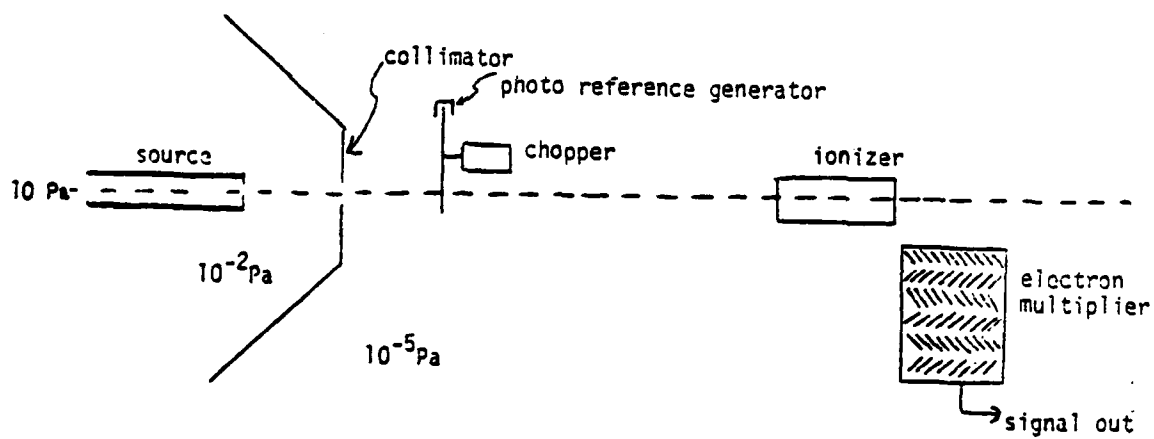


FIGURE 3  
The Apparatus

MASSACHUSETTS INST OF TECH CAMBRIDGE DEPT OF AERONAU--ETC F/G 7/4  
THE INTERACTION OF MONATOMIC AND DIATOMIC MOLECULES WITH SOLID --ETC  
NOV 80 D D DREYFUSS, L TRILLING, H Y WACHMAN F44620-76-C-0036

AFOSR-TR-80-1368

24

40239-

END

DATE \_\_\_\_\_

FILMED

2-8

DTIC

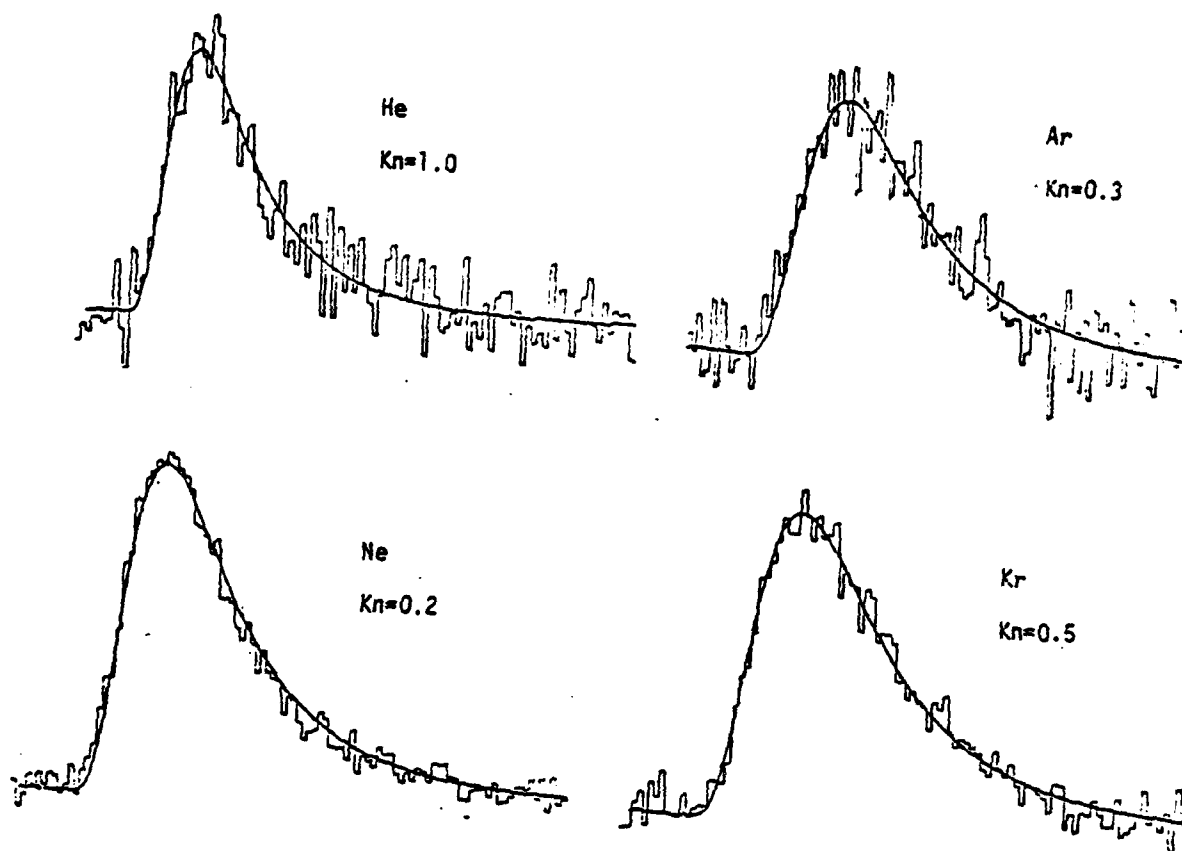


FIGURE 4

Calibration Examples

Solid Curves are theoretical Maxwellian TOF curves at source temperature (fitting parameters: baseline, amplitude). Periods (abscissas) are not equal.

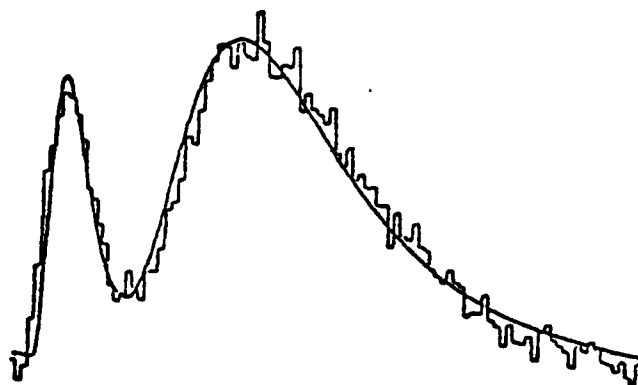


FIGURE 5

Sample TOF Waveform for a  $H_2/Ar$  Gas Mixture. Solid Curve is a least-squares fit of a sum of two Maxwellians to the data (fitting parameters: baseline, amplitudes).

---

## APPENDIX B. DATA PROCESSING PROGRAMS AND DOCUMENTATION

This appendix contains user instructions for the data handling software, as well as copies of the programs. Computer hardware is described in Section 2.6. Programs were written in FORTRAN IV. Non-standard subroutines include a collection provided by the manufacturer for support of specific hardware (clock, A/D, and graphic display terminal). An additional set of subroutines were specially written for use with the plotter. Documentation for these routines is available (and is kept with the system software documentation) but is not reproduced here.

## DOCUMENTATION FOR EXPERI.

Includes documentation for all routines present as of May 1980.

Programs and documentation written by David Dreyfuss.

The program is accessed by putting disk labeled EXPERIMENT in drive 0 and a disk for data in drive 1. Routines are available to collect and store data, as well as to perform a variety of data processing tasks. A summary and list are available by running the program (type R EXPERI) and typing HELP.

All routines are accessible in any order. When the program is started and whenever a routine is finished, a prompt character ( > ) indicates that a new routine can be selected. Simply type the name of the routine to start it. Generally, data is preserved until a routine specifically changes or replaces it. To return to the RT11 monitor, type QUIT. If an error causes the program to abort, it should be restarted using the monitor REENTER command which will give the EXPERI prompt character ( > ), and leave the data unchanged (i.e. if a spectrum has been read in from disk, it will still be there). Many errors are detected and dealt with by the program. Routines with two word names can be written as either one or two words (with or without a space).

Assumed hardware is a 103 channel pseudorandom chopped time-of-flight system with a 100 channel Waveform Eductor providing signal averaging.

1) Data reading and file maintenance.

DATA --- Reads in a spectrum. Queries as follows:

NEW or OLD? --- Select NEW to accept a new spectrum via the A/D converter and store it on disk, or OLD to retrieve a spectrum already on disk.

File name: --- If OLD was selected this is where the file name is entered, assumed to be on drive 1 and have a .DAT extension.

Run no.: --- Spectra are labeled by the run number entered here. A new spectrum is stored in a file DX1:RUN.DAT, where n is the run number. This puts each new spectrum in a separate file to provide crash resistance for the data. These files are generally combined into one file at the end of a data gathering session using CONCAT. Old spectra are thus identified by file name and run number. Old spectra from the same day's run would be accessed by file name RUN and run number n.

CONCAT --- Concatenates temporary data files into one larger file. Queries as follows:

Output file: --- A 6 letter (maximum) name for the output file. Standard practice is to use the date in the form 02MAY0, where the first 2 digits are the day of the month, the next 3 characters give the month, and the final digit is the final

disit of the year (e.g. 0 for 1980).

Are files consecutively numbered starting with 1? --- Answer YES or NO as appropriate. Usually the answer should be YES.

How many files? --- Give number of files to be concatenated.

If the files are consecutively numbered, the concatenation proceeds. If not, each file must be given (when asked for) by name. The process may be slow, since a lot of disk operations are required.

## 2) Plotting routines.

Many of the data processing routines automatically produce plots, but in addition there are the following routines for controlling plots:

### PLOTON

PLOTTOFF --- These routines simply enable and disable plotting on the HP 7225A plotter. The plotting is sufficiently slow that standard practice is to use the plotter only to produce report quality reproductions. For routine plotting the display screen is adequate, and the terminal copier can provide quick hard copies. The default condition when the program is started is with the plotter disabled.

### ERASE

DISPLAY --- These routines can suppress or reactivate the graphic display on the terminal (primarily to avoid confusion with text). Stored data is not affected, and subsequent plotting proceeds regardless of how these routines are used.

HISTOGRAM --- Allows activation or suppression of histogram display on terminal (filling in space below graph). Queries are obvious.

PLOTDATA --- Plots raw data (prior to deconvolution). Generally used to check visually that data was read in correctly, and to check for necessary interpolation.

## 3) Data manipulation routines.

These routines change a spectrum in various ways. The raw data is always maintained on disk. In addition the current spectrum can also be recovered by reinvoking DECONV (it is not necessary to reread the raw data unless a smaller interpolation is desired).

DECONV --- Recovers a time-of-flight spectrum from the pseudorandom-chopped raw data. Queries as follows:

FORWARD or REVERSE chopping? --- Normally the chopper is run in one direction labeled 'FORWARD'. If for some reason the chopper is run in the other direction, REVERSE can be selected.

The channels around the region to be interpolated are printed, and then the query:

Low and high channels for interpolation: --- If all 100 channels of the Waveform Eductor signal are good, the standard answer is 100,104. It is sometimes desirable to extend the interpolation region by one or two channels in either direction. Interpolation is simply linear between the endpoints.

A plot of the deconvoluted spectrum is automatically produced.

### SUBMAX

SUBTRANS --- Subtract a manually chosen Maxwellian (SUBMAX) or translating Maxwellian (SUBTRANS) from a deconvoluted spectrum. This procedure is invoked when a known Maxwellian component is obscuring other features of interest. Queries as follows:

```

Flight path (cm.):      :
Period (msec.):         : Responses are obvious. All
Eductor delay (usec.):   : numbers should be entered as
Temperature (centigrade): : real (with decimal point).
Mach number: [SUBTRANS only] :
Molecular weight:       :
Maxwellian amplitude:   :

```

Eductor delay is the delay from the center of the trigger pulse to the beginning of the first channel as set on the Waveform Eductor.  
Maxwellian amplitude is the peak amplitude.

After the revised spectrum is plotted comes the query:

Another try? --- A response of NO or <CR> ends the routine. A response of YES allows the selection of a new amplitude in case the subtraction does not appear reasonable. The query 'Maxwellian amplitude:' is repeated, and a new plot is produced. The cycle can be repeated indefinitely.

**SMOOTH** --- smooths data by low-pass digital filtering (see Kaiser and Reed, R.S.I. 48:1447 (1977) for details of the technique). Lambda is set to 80 dB, and delta is set to about 2.5 Fourier components, which sets NP to 103, giving good accuracy and reasonable run-time. Queries are as follows:

How many Fourier components to be kept? --- For typical time-of-flight spectra, around 10-15 components represent the usable information. For a 103 channel signal, 52 components contains all the information available. This filtering process does effectively eliminate all of the high-frequency noise, but since the low frequency noise is generally of about the same amplitude, eliminating just the high frequency noise tends to create features which aren't really present. The human brain seems capable of doing a more realistic smoothing operation on the unsmoothed data by fitting a curve of approximately the right shape.

The smoothed data is plotted over the original spectrum. Additional queries allow another choice of number of components and ask whether the smoothed version should replace the original.

#### 4) Information extracting and fitting routines.

**PEAKS** --- Locates peak positions and amplitudes and calculates average velocity for any time-of-flight spectrum. Queries are as follows:

```

Flight path (cm.):      :
Period (msec.):         : Responses as for SUBMAX
Eductor delay (usec.):   :
How many channels are 'zero'? --- Number of channels at beginning
of spectrum which can be taken as zero for determining a
baseline (enter as integer [no decimal point]).

```

Peaks found are marked on display, and positions and amplitudes are printed along with the average velocity.

**MAXFIT** --- Fits one or two Maxwellians of the form  $V_{xx}^2 \exp(-V_{xx}^2)$  to a spectrum. Plots fit. Queries are as follows:

```

How many species? --- 1 or 2. Determines whether 1 or 2 Maxwellians
are to be fit (integer).
Flight path (cm.):      :
Period (msec.):         : Responses as for SUBMAX and PEAKS
Temperature (centigrade): :
Molecular weight(s):    :

```



How many channels are 'zero'?  
What fraction do you want to fit (starting from left)? --- Real number between 0. and 1. indicating how much of the spectrum is to be used for fitting (allows fitting to a tail or fitting to one portion of spectrum if desired). This option is available only for a single Maxwellian fit.

Fitting is by least squares. Fitting parameters are just the amplitudes of the 1 or 2 Maxwellians specified. The two Maxwellians are distinguished only by their molecular weight as might be appropriate for a gas mixture.

TRANSFIT --- Similar to MAXFIT, but one of the Maxwellians can be a translating Maxwellian:  $U \cdot \exp(-(U-U_0)^2)$ . Queries as follows:

How many species? --- If 1 is selected a fit is made for a translating Maxwellian. 2 gives one of each type.

Other queries as for MAXFIT with the following changes: Only one molecular weight can be specified. Two temperatures are allowed, and, of course, a Mach number is needed for the translating Maxwellian. The Mach number is the ratio of  $U$  to the average thermal velocity,  $\sqrt{8kT/(\pi)m}$ .

SAVE --- Stores a spectrum for use by DOUBLEFIT.

DOUBLEFIT --- Fits the sum of a spectrum stored by SAVE and a Maxwellian. Queries as for MAXFIT, with a warning that SAVE must be invoked first, and a question as to whether a spectrum has been stored.

```

C      PROGRAM EXPERI
Monitor program for control of data acquisition and processing
REAL DECONV(309),MAX1,MIN1
INTEGER DATA(206),GRAPH(512)
BYTE COMMAN(21),TDATE(9),TTIME(8),RUNNO(5),ERR
C      The following values are passed around among subroutines.
COMMON /RAWD/ DATA,MIN,MAX, /DECD/ DECONV,MAX1,MIN1,ICHNL1,GTO
+/,/PLOT/ GRAPH, /RUNUM/ RUNNO
CALL DATE(TDATE)
CALL TIME(TTIME)
T=10*(TTIME(1)-48)+TTIME(2)-48
IF (T .LE. 12) GOTO 5
IT=(T-12)/10
TTIME(1)=48+IT
TTIME(2)=36+T-IT*10
5      IF (TTIME(1) .EQ. 48) TTIME(1)=32
CALL PLOTOFF
CALL PLOTSS(13,72,)
CALL PLOTSS(10,,)
TYPE 10,TDATE,(TTIME(I),I=1,5)
10     FORMAT(' Data acquisition & processing system version 1:
+last changed 4-MAR-80.'/' Today is ',9A1,' and it is '
+,'SA1,' o'clock.'//)
C      Enter prompt character.
20     TYPE 30
30     FORMAT (' > ',3)
CALL GETSTR(5,COMMAN,20)
CALL SCOPY(COMMAN,COMMAN,16)
CALL TRIM(COMMAN)
C      Identify command and invoke appropriate routine.
CALL SCOMP('HELP',COMMAN,IVAL)
IF (IVAL .NE. 0) GOTO 40
CALL HELP
GOTO 20
40     CALL SCOMP('DATA',COMMAN,IVAL)
IF (IVAL .NE. 0) GOTO 50
CALL READER
GOTO 20
50     CALL SCOMP('DECONV',COMMAN,IVAL)
IF (IVAL .NE. 0) GOTO 60
CALL DECONV
GOTO 20
60     CALL SCOMP('MAXFIT',COMMAN,IVAL)
IF (IVAL .NE. 0) GOTO 70
CALL MAXFIT
GOTO 20
70     CALL SCOMP('PLOTDATA',COMMAN,IVAL)
CALL SCOMP('PLOT DATA',COMMAN,JVAL)
IF (IVAL .NE. 0 .AND. JVAL .NE. 0) GOTO 80
CALL PLDATA
GOTO 20
80     CALL SCOMP('CONCAT',COMMAN,IVAL)
IF (IVAL .NE. 0) GOTO 90
CALL JOIN
GOTO 20
90     CALL SCOMP('ERASE',COMMAN,IVAL)
IF (IVAL .NE. 0) GOTO 100
CALL ERASE
GOTO 20
100    CALL SCOMP('DISPLAY',COMMAN,IVAL)
IF (IVAL .NE. 0) GOTO 110
CALL DISPLAY

```

```

110      GOTO 20
      CALL SCOMP('HISTOGRAM',COMMAN,IVAL)
      IF (IVAL .NE. 0) GOTO 120
      CALL HISTO
      GOTO 20
120      CALL SCOMP('QUIT',COMMAN,IVAL)
      IF (IVAL .NE. 0) GOTO 130
      CALL EXIT
130      CALL SCOMP('SAVE',COMMAN,IVAL)
      IF (IVAL .NE. 0) GOTO 140
      CALL SAVE
      GOTO 20
140      CALL SCOMP('DOUBLE FIT',COMMAN,IVAL)
      CALL SCOMP('DOUBLEFIT',COMMAN,JVAL)
      IF (IVAL .NE. 0 .AND. JVAL .NE. 0) GOTO 150
      CALL DBLFIT
      GOTO 20
150      CALL SCOMP('TRANSFIT',COMMAN,IVAL)
      IF (IVAL .NE. 0) GOTO 160
      CALL TRAFIT
      GOTO 20
160      CALL SCOMP('SUBMAX',COMMAN,IVAL)
      IF (IVAL .NE. 0) GOTO 170
      CALL SUBMAX(1)
      GOTO 20
170      CALL SCOMP('SUBTRANS',COMMAN,IVAL)
      IF (IVAL .NE. 0) GOTO 180
      CALL SUBMAX(2)
      GOTO 20
180      CALL SCOMP('PEAKS',COMMAN,IVAL)
      IF (IVAL .NE. 0) GOTO 190
      CALL PEAKS
      GOTO 20
190      CALL SCOMP('SMOOTH',COMMAN,IVAL)
      IF (IVAL .NE. 0) GOTO 200
      CALL SMOOTH
      GOTO 20
200      CALL SCOMP('PLOTON',COMMAN,IVAL)
      CALL SCOMP('PLOT ON',COMMAN,JVAL)
      IF (IVAL .NE. 0 .AND. JVAL .NE. 0) GOTO 210
      CALL PLTON
      GOTO 20
210      CALL SCOMP('PLOTOFF',COMMAN,IVAL)
      CALL SCOMP('PLOT OFF',COMMAN,JVAL)
      IF (IVAL .NE. 0 .AND. JVAL .NE. 0) GOTO 220
      CALL PLTOFF
      GOTO 20
220      CONTINUE
      TYPE 510
510      FORMAT('What?')
      GOTO 20
C      TO ADD A NEW ROUTINE: WRITE ROUTINE, ADD 4 LINES AS ABOVE, AND
C      ADD NEW INSTRUCTION TO LIST IN HELP SUBROUTINE.
      END

SUBROUTINE REPL(INSTRN,RNUM)
C      Extends capabilities of PLTRER to handle larger numbers.
      BYTE INSTRN(81)
      IF (RNUM .LT. 10000.) GOTO 10
      CALL CONCAT(INSTRN,'##',INSTRN)
      CALL PLTREI(INSTRN,INT(RNUM/10000.))
      RNUM=RNUM-10000.*INT(RNUM/10000.)
      IF (RNUM .GE. 1000) GOTO 10
      CALL INSERT('0##',INSTRN,INDEX(INSTRN,'##'))
      IF (RNUM .GE. 100) GOTO 10
      CALL INSERT('0##',INSTRN,INDEX(INSTRN,'##'))

```

```

IF (RNUM .GE. 10) GOTO 10
CALL INSERT('0##',INSTRN,INDEX(INSTRN,'##'))
10 CALL PLTREI(INSTRN,INT(RNUM+.3))
CALL CONCAT(INSTRN,'.',INSTRN)
RETURN
END

SUBROUTINE HELP
TYPE 10
10 FORMAT (' Current valid commands are:/'
+ ' HELP',T20,'Produces this list.//'
+ ' DATA',T20,'Reads in a new or old spectrum and stores it.//'
+ ' PLOTDATA',T20,'Plots raw data.//'
+ ' DECONV',T20,'Deconvolutes data and plots it.//'
+ ' SUBMAX',T20,'Subtracts a manually chosen Maxwellian from data &
+ replots.//'
+ ' SUBTRANS',T20,'Same as SUBMAX, but using translating
+ Maxwellian.//'
+ ' SMOOTH',T20,'Performs low-pass filtering on deconvoluted data.//'
+ ' MAXFIT',T20,'Fits one or two Maxwellians to deconvoluted data &
+ plots/T25, 'over data plot.//'
+ ' SAVE',T20,'Stores a deconvoluted trace for DOUBLE FIT.//'
+ ' DOUBLE FIT',T20,'Fits the sum of a Maxwellian and a stored
+ waveform/T25, 'and plots over data plot.//'
+ ' TRANSFIT',T20,'Fits a translating Maxwellian and plots it or
+ fits the/T25, 'sum of that and a regular Maxwellian and
+ plots it.//'
+ ' PEAKS',T20,'Locates and gives resolved peak amplitudes; finds
+ average/T25, 'velocity.//'
+ ' ERASE',T20,'Stops all graphic display.//'
+ ' DISPLAY',T20,'Reactivates graphic display.//'
+ ' HISTOGRAM',T20,'Disables or re-enables histogram.//'
+ ' CONCAT',T20,'Condenses all temporary data files into
+ one file.//'
+ ' PLOT ON',T20,'Activates 7225A plotter.//'
+ ' PLOT OFF',T20,'Deactivates 7225A plotter.//'
+ ' QUIT',T20,'Returns system to RT-11 monitor.//'
+ ' For more help, type "TYPE SY:EXPERI.DOC" from RT-11 monitor.')
RETURN
END

SUBROUTINE ERASE
CALL PLOT33(2,0,1)
RETURN
END

SUBROUTINE D5PLAY
CALL PLOT33(2,1,0)
CALL PLOT33(13,72,)
CALL PLOT33(10,,)
RETURN
END

SUBROUTINE PLDATA
INTEGER DATA(206),GRAPH(312)
COMMON /RAWD/ DATA,MIN,MAX, /PLOT/ GRAPH
ICHNL1=60 !set starting point for plot.
CALL PLOT33(2,312,)
CALL PLT33(1,0,)
CALL PLT33(2,137,374)
CALL PLOT33(13,72,)
CALL PLOT33(10,,)
DO 10,IX=0,305,5
IY=INT(FLOAT(DATA(ICHNL1+IX/5)-MIN)*235./(MAX-MIN))
DO 10, I=1,3
GRAPH(IX+I)=IY
10

```

```

      IY=INT(FLOAT(DATA(ICHNL1+102)-MIN)*233./((MAX-MIN)))
      GRAPH(311)=IY
      GRAPH(312)=IY
      CALL PLT55(7,0,0)
      CALL PLT55(3,-312,GRAPH)
      CALL PLT55(2,1,)
      RETURN
      END

      SUBROUTINE HISTO
      BYTE ANSWER(10),ERR
      ERR=.FALSE.
3      TYPE 10
10     FORMAT ('+Turn ON or OFF? ',)
      CALL GETSTR(5,ANSWER,9,ERR)
      CALL SCOMP('ON',ANSWER,IVAL)
      IF (IVAL .EQ. 0) GOTO 50
      CALL SCOMP('OFF',ANSWER,IVAL)
      IF (IVAL .EQ. 0) GOTO 70
      TYPE 20
20     FORMAT ('+What?'/)
      GOTO 5
50     CALL PLOT55(2,8,0)
      GOTO 100
70     CALL PLOT55(2,0,8)
100    CALL PLOT55(13,72,)
      CALL PLOT55(10,,)
      RETURN
      END

      SUBROUTINE DECONV
      BYTE TDATE(81),RUNNO(5)
      COMMON /RUNUM/ RUNNO
      REAL MAX1,MIN1,DECONV(309)
      INTEGER DATA(206),HIGH,GRAPH(312)
      BYTE S(103),IDIREC(8),ANSWER(12),ERR,IVAL,JVAL
      COMMON /RAWD/ DATA,/DECD/DECONV,MAX1,MIN1,ICHNL1,GTO
      +, /PLOT/ GRAPH
C      Set up deconvolution sequence, set IDIREC initially to 'FORWARD'.
      DATA ERR/.FALSE./,3/7*1,3*-1,3*1,-1,-1,1,-1,3*1,-1,-1,1,-1,1,
      +3*-1,3*1,7*-1,3*1,-1,1,-1,-1,1,3*-1,1,3*-1,1,-1,1,-1,1,-1,
      +4*1,-1,1,1,-1,-1,1,-1,1,1,-1,-1,1,4*-1,1,-1,-1,1,-1,1,-1,3*1,
      +1,3*1,-1,1,1,-1,1,3*-1/,IDIREC/70,79,82,87,45,82,68,0/
      TYPE 10
10     FORMAT ('+FORWARD or REVERSE chopping? ',)
      CALL GETSTR(5,ANSWER,10,ERR)
      CALL SCOMP('FORWARD',ANSWER,IVAL)
      IF (IVAL .NE. 0) GOTO 20
      ICHNL1=59                !1st channel to plot.
      GTO=60.9                 !Geometric time origin (no delay corrections).
      GOTO 50
20     CALL SCOMP('REVERSE',ANSWER,IVAL)
      IF (IVAL .EQ. 0) GOTO 40
      TYPE 30
30     FORMAT ('+What?'/)
      GOTO 5
40     ICHNL1=40                !1st channel to plot
      GTO=42.1                 !Geometric time origin.
C      Reverse deconvolution sequence if direction is changed.
50     IF (ISCOMP(IDIREC,ANSWER) .EQ. 0) GOTO 70
      CALL SCOPY(ANSWER,IDIREC)
      DO 60,I=2,52
      J=S(I)
      S(I)=S(103-I)
60     S(103-I)=J
C      Choose channels for interpolation and perform linear interpolation.

```

```

70      TYPE 80
80      FORMAT ('+Channels 96 thru 108')
      TYPE 90, (DATA(I),I=96,108)
90      FORMAT (13I5)
      TYPE 100
100     FORMAT (' Low and high channels for interpolation: ',3)
      ACCEPT 110,LOW,HIGH
110     FORMAT (2I4)
      DO 140,I=LOW+1,HIGH-1
      DATA(I)=(I-LOW)*(DATA(HIGH)-DATA(LOW))/(HIGH-LOW)+DATA(LOW)
      IF (I-103) 130,120,120
120     DATA(I-103)=DATA(I)
      GOTO 140
130     DATA(I+103)=DATA(I)
140     CONTINUE
C      Deconvolute:
      DO 150 I=1,103
150     DECONV(I)=0.
      MAX1=-10000.
      MIN1=10000.
      DO 170,I=1,103
      DO 160,J=1,103
160     DECONV(I)=DECONV(I)+S(J)*FLOAT(DATA(I+J))
      DECONV(I)=-DECONV(I)
      DECONV(I+103)=DECONV(I)
      DECONV(I+206)=DECONV(I)
      MAX1=AMAX1(MAX1,DECONV(I))
      MIN1=AMIN1(MIN1,DECONV(I))
170     'Determine max and min values for plot
C
C      PLOTTING ROUTINE
C
      CALL PLOT55(1,0,)
      CALL PLOT55(2,512,)
      CALL PLT55(2,9,502)
      CALL PLOT55(13,72,)
      CALL PLOT55(10,,)
      DO 200, IX=0,505,5
      IY=INT((DECONV(ICHNL1+IX/5)-MIN1)*201./(MAX1-MIN1))+17
      DO 200, I=1,5
200     GRAPH(IX+I)=IY
      IY=INT((DECONV(ICHNL1+102)-MIN1)*201./(MAX1-MIN1))+17
      GRAPH(511)=IY
      GRAPH(512)=IY
      CALL PLT55(7,0,0)
      CALL PLT55(3,-512,GRAPH)
      CALL PLT55(9,44,0)
      CALL DATE(TDATE)
      TDATE(10)=0
      CALL PLTTXT(TDATE)
      CALL PLT55(9,44,1)
      CALL CONCAT('Run #',RUNNO,TDATE)
      CALL PLTTXT(TDATE)
      CALL PLT55(9,44,2)
      CALL SCOPY('Full scale amplitude: ##',TDATE)
      CALL REPL(TDATE,MAX1-MIN1)
      CALL PLTTXT(TDATE)
      CALL PLOT55(13,72,)
      CALL PLT55(2,1,)
      RETURN
      END

      SUBROUTINE MAXFIT
      BYTE TDATE(81),RUNNO(5)
      COMMON /RUNUM/ RUNNO
      REAL MAXWEL,DECONV(309),MAX1,MIN1
      MAXWEL(U)=EXP(-(U*U))*U**4

```

```

C      This is a static Maxwellian. The V**4 occurs because the plots are
C      time-of-flight ( $dv=L/t^2$   $dt=v^2/L$   $dt$ ).
      INTEGER GRAPH(512)
      COMMON /DECD/ DECONV,MAX1,MIN1,ICHNL1,GTO
5      TYPE 10
10     FORMAT ('+How many species? ',5)
      ACCEPT 20,NSPEC
      FORMAT (I3)
20     IF (NSPEC .EQ. 1 .OR. NSPEC .EQ. 2) GOTO 40
      TYPE 30
30     FORMAT ('+1 or 2 only!'/)
      GOTO 5
40     ZERO=0.
      TYPE 50
50     FORMAT ('+Flight path (cm.): ',5)
      ACCEPT 60,PATH
60     FORMAT (F9.4)
      TYPE 70
70     FORMAT ('+Period (nsec.): ',5)
      ACCEPT 60,PERIOD
      TYPE 80
80     FORMAT ('+Eductor delay (usec.): ',5)
      ACCEPT 60,DELAY
      TO=GTO-(DELAY+3.)*.103/PERIOD !locates time origin. 3 is for
      PERIOD=PERIOD/1000. !electronic delay.
      ITO=INT(TO+1.) !1st channel for fittings.
      IZERO=INT(5.*(TO-ICHNL1)) !No. of points at beginning of fitted
      IZ=IZERO !curve to set to zero.
      IF (IZERO .LT. 0) IZERO=0
      TYPE 90
90     FORMAT ('+Temperature (centigrade): ',5)
      ACCEPT 60,TEMP
      TEMP=TEMP+273.15
      GOTO (100,120) NSPEC
100    TYPE 110
110    FORMAT ('+Molecular weight: ',5)
      ACCEPT 60,WEIGHT
      TSCALE=SQRT(WEIGHT/TEMP*6.01659E-9)*PATH !scaling time for
      GOTO 150 !MAXWEL velocity.
120    TYPE 130
130    FORMAT ('+Molecular weights: ',5)
      ACCEPT 140,WEIGH1,WEIGH2
140    FORMAT (2F9.4)
      TSCAL1=SQRT(WEIGH1/TEMP*6.01659E-9)*PATH
      TSCAL2=SQRT(WEIGH2/TEMP*6.01659E-9)*PATH
150    TYPE 160
C      Set baseline.
160    FORMAT ('+How many channels are 'zero'? ',5)
      ACCEPT 20,NZERO
      DO 170, I=ITO-NZERO,ITO+NZERO-1
170    ZERO=ZERO+DECONV(I)
C      Set prefittng points on fitted curve.
      ZERO=ZERO/NZERO/2
      IY=INT((ZERO-MIN1)*201./(MAX1-MIN1))+17
      DO 180, I=0,IZERO+3
180    GRAPH(I+1)=IY
      GOTO (200,250) NSPEC
C      Single Maxwellian fit.
200    S1=0.
      S2=0.
204    TYPE 205
205    FORMAT ('+What fraction do you want to fit (starting
      +from right)? ',5)
      ACCEPT 206,FRACT
206    FORMAT (F6.4)
      IF (FRACT .GT. 0. .AND. FRACT .LE. 1.) GOTO 208

```

```

207     TYPE 207
      FORMAT ('+Huh? Between 0. and 1. please!'/)
      GOTO 204
208     START=INT(103*(1-FRACT))
      IF (START .LT. NZERO/2) START=NZERO/2
      DO 210, I=ITO+START, ITO+102
      V=103./(I-T0)/PERIOD*TSCALE
      S1=S1+(DECONV(I)-ZERO)*MAXWEL(V)
210     S2=S2+MAXWEL(V)**2
      AMP=S1/S2
      DO 220, I=IZERO+1, 511
      IF (I .LE. 0) GOTO 220
      V=512./(I-IZERO)/PERIOD*TSCALE
      Y=AMP*MAXWEL(V)+ZERO
      GRAPH(I+4)=INT((Y-MIN1)*201./(MAX1-MIN1))+17
      IF (GRAPH(I+4) .LT. 0) GRAPH(I+4)=0
      IF (GRAPH(I+4) .GT. 235) GRAPH(I+4)=235
220     CONTINUE
      GOTO 300
C      Double Maxwellian fit.
250     S1=0.
      S2=0.
      S3=0.
      S4=0.
      S5=0.
      DO 260, I=ITO+NZERO/2, ITO+102
      V1=103./(I-T0)/PERIOD*TSCALE1
      V2=103./(I-T0)/PERIOD*TSCALE2
      S1=S1+MAXWEL(V1)**2
      S2=S2+MAXWEL(V1)*MAXWEL(V2)
      S3=S3+MAXWEL(V2)**2
      S4=S4+(DECONV(I)-ZERO)*MAXWEL(V1)
260     S5=S5+(DECONV(I)-ZERO)*MAXWEL(V2)
      DEN=S1*S3-S2*S2
      AAMP=(S4*S3-S2*S5)/DEN
      BAMP=(S1*S5-S4*S2)/DEN
      DO 270, I=IZERO+1, 511
      IF (I .LE. 0) GOTO 270
      V1=512./(I-IZERO)/PERIOD*TSCALE1
      V2=512./(I-IZERO)/PERIOD*TSCALE2
      Y=AAMP*MAXWEL(V1)+BAMP*MAXWEL(V2)+ZERO
      GRAPH(I+4)=INT((Y-MIN1)*201./(MAX1-MIN1))+17
      IF (GRAPH(I+4) .LT. 0) GRAPH(I+4)=0
      IF (GRAPH(I+4) .GT. 235) GRAPH(I+4)=235
270     CONTINUE
C      Determine Standard Deviation.
300     VAR=0.
      DO 330, I=ITO+NZERO/2, ITO+102
      GOTO (310, 320) NSPEC
310     V=103./(I-T0)/PERIOD*TSCALE
      TERM=AMP*MAXWEL(V)
      GOTO 330
320     V1=103./(I-T0)/PERIOD*TSCALE1
      V2=103./(I-T0)/PERIOD*TSCALE2
      TERM=AAMP*MAXWEL(V1)+BAMP*MAXWEL(V2)
330     VAR=VAR+(DECONV(I)-ZERO-TERM)**2
C      PLOTTING ROUTINE
      CALL PLOT55(13, 72, )
      CALL PLOT55(10, , )
      CALL PLOT55(1, 1, )
      CALL PLT55(2, 167, 314)
      CALL PLT55(4, 1, IY)
      CALL PLT55(7, 0, 0)
      CALL PLT55(3, -512, GRAPH)
      CALL PLOT55(1, 0, )
      CALL PLT55(6, IZ, 1)

```

!Marker put on graph 0 since  
!graph 1 markers are flaky!



```

CALL PLOT55(9,44,0)
CALL DATE(TDATE)
TYPE 335, (TDATE(I),I=1,9)
335  FORMAT('+',9A1)
CALL PLOT55(9,44,1)
TYPE 340
340  FORMAT ('+Run #',%)
CALL PUTSTR(7,RUNNO,'+')
CALL PLT55(9,44,3)
GOTO (350,370) NSPEC
350  CALL SCOPY('Fit amplitude: ##',TDATE)
CALL REPL(TDATE,AMP*4./EXP(2.))
CALL PLTTXT(TDATE)
GOTO 400
370  CALL SCOPY('Coefficient for mass ##: ##',TDATE)
CALL PLTRER(TDATE,WEIGH1)
CALL REPL(TDATE,AMP*4./EXP(2.))
CALL PLTTXT(TDATE)
CALL PLT55(9,44,4)
CALL SCOPY('Coefficient for mass ##: ##',TDATE)
CALL PLTRER(TDATE,WEIGH2)
CALL REPL(TDATE,AMP*4./EXP(2.))
CALL PLTTXT(TDATE)
400  CALL PLT55(9,44,5)
VAR=SQRT(VAR/(102-NZERO/2))/(MAX1-MIN1)*100.
VAR=INT(10.*VAR)*.1
CALL SCOPY('Standard deviation: ##%',TDATE)
CALL PLTRER(TDATE,VAR)
CALL PLTTXT(TDATE)
CALL PLOT55(13,72,)
CALL PLT55(2,1,)
RETURN
END

SUBROUTINE SAVE
C  Saves a spectrum for DBLFIT.
REAL DECONV(309),SAVED(309),SAMP,MAX1,MIN1
COMMON /DECD/ DECONV,MAX1,MIN1, /SAVER/ SAVED,SAMP
DO 10, I=1,309
10  SAVED(I)=DECONV(I)
SAMP=MAX1-MIN1
RETURN
END

SUBROUTINE DBLFIT
BYTE TDATE(81),RUNNO(5),ERR
COMMON /RUNUM/ RUNNO
REAL MAXWEL,DECONV(309),SAVED(309),MAX1,MIN1
MAXWEL(V)=EXP(-(V*V))*V**4
INTEGER GRAPH(512)
COMMON /DECD/ DECONV,MAX1,MIN1,ICHNL1,GTO, /SAVER/ SAVED,SAMP
TYPE 10
10  FORMAT ('+This routine fits the sum of a Maxwellian and a waveform
+ stored using // SAVE. Is that waveform ready? ',%)
CALL GETSTR(5,TDATE,8,ERR)
CALL SCOMP('NO',TDATE,IVAL)
IF (IVAL .EQ. 0) RETURN
SZERO=0.
ZERO=0.
TYPE 50
50  FORMAT ('+Flight path (cm.): ',%)
ACCEPT 60,PATH
60  FORMAT (F9.4)
TYPE 70
70  FORMAT ('+Period (nsec.): ',%)
ACCEPT 60,PERIOD

```

```

      TYPE 80
80  FORMAT ('+Eductor delay (usec.): ',%)
      ACCEPT 60, DELAY
      TO=GT0-(DELAY+3.)*.103/PERIOD
      PERIOD=PERIOD/1000.
      ITO=INT(TO+1.)
      IZERO=INT(5.*(TO-ICHNL1))
      IZ=IZERO
      IF (IZERO .LT. 0) IZERO=0
      TYPE 90
90  FORMAT ('+Temperature (centigrade): ',%)
      ACCEPT 60, TEMP
      TEMP=TEMP+273.15
      TYPE 110
110 FORMAT ('+Molecular weight: ',%)
      ACCEPT 60, WEIGHT
      TSCALE=SQRT(WEIGHT/TEMP*6.01659E-9)*PATH
      TYPE 160
160 FORMAT ('+How many channels are "zero"? ',%)
      ACCEPT 165, NZERO
165  FORMAT (I3)
      DO 170, I=ITO-NZERO, ITO+NZERO-1
      SZERO=SZERO+SAVED(I)
170  ZERO=ZERO+DECONV(I)
      SZERO=SZERO/NZERO/2
      ZERO=ZERO/NZERO/2
      IY=INT((ZERO-MIN1)*201./(MAX1-MIN1))+17
      DO 180, I=0, IZERO+3
180  GRAPH(I+4)=IY
C  FITTING
      S1=0.
      S2=0.
      S3=0.
      S4=0.
      S5=0.
      DO 260, I=ITO+NZERO/2, ITO+102
      V=103./(I-TO)/PERIOD*TSCALE
      S1=S1+MAXWEL(V)**2
      S2=S2+MAXWEL(V)*(SAVED(I)-SZERO)
      S3=S3+(SAVED(I)-SZERO)**2
      S4=S4+(DECONV(I)-ZERO)*MAXWEL(V)
260  S5=S5+(DECONV(I)-ZERO)*(SAVED(I)-SZERO)
      DEN=S1*S3-S2*S2
      AAMP=(S4*S3-S2*S5)/DEN
      BAMP=(S1*S5-S4*S2)/DEN
      DO 300, I=IZERO+1, 311
      IF (I .LE. 0) GOTO 300
      J=I/5+ICHNL1
      K=I-I/5+1
      GOTO (270, 270, 270, 280, 280) K
270  TERM=FLOAT(K+2)/5.*(SAVED(J)-SAVED(J-1))+SAVED(J-1)-SZERO
      GOTO 290
280  TERM=FLOAT(K-3)/5.*(SAVED(J+1)-SAVED(J))+SAVED(J)-SZERO
290  V=512./(I-IZERO)/PERIOD*TSCALE
      Y=AAMP*MAXWEL(V)+BAMP*TERM+ZERO
      GRAPH(I+4)=INT((Y-MIN1)*201./(MAX1-MIN1))+17
      IF (GRAPH(I+4) .LT. 0) GRAPH(I+4)=0
      IF (GRAPH(I+4) .GT. 235) GRAPH(I+4)=235
300  CONTINUE
      VAR=0.
      DO 330, I=ITO+NZERO/2, ITO+102
      V=103./(I-TO)/PERIOD*TSCALE
      TERM=AAMP*MAXWEL(V)+BAMP*(SAVED(I)-SZERO)
330  VAR=VAR+(DECONV(I)-ZERO-TERM)**2
C  PLOTTING ROUTINE
      CALL PLOT55(13, 72,)

```

```

CALL PLOT55(10,,)
CALL PLT55(1,1,)
CALL PLT55(2,167,344)
CALL PLT55(4,1,IY)
CALL PLT55(7,0,0)
CALL PLT55(3,-512,GRAPH)
CALL PLT55(1,0,)
CALL PLT55(6,IZ,1)
CALL PLOT55(9,44,0)
CALL DATE(TDATE)
TYPE 335,TDATE
335  FORMAT ('+',9A1)
CALL PLOT55(9,44,1)
TYPE 340
340  FORMAT ('+Run #',)
CALL PUTSTR(7,RUNNO,'+')
CALL PLT55(9,44,3)
CALL SCOPY('Coefficient for Maxwellian: #',TDATE)
CALL REPL(TDATE,AAMP*4./EXP(2.))
CALL PLTTXT(TDATE)
CALL PLT55(9,44,4)
CALL SCOPY('Coefficient for other peak: #',TDATE)
CALL REPL(TDATE,BAMP*SAMP)
CALL PLTTXT(TDATE)
CALL PLT55(9,44,5)
CALL SCOPY('Standard deviation: ##%',TDATE)
RNUM=INT(10*SQR(TVAR/(102-NZERO/2)))/(MAX1-MIN1)*100.)*.1
CALL PLTRER(TDATE,RNUM)
CALL PLTTXT(TDATE)
CALL PLOT55(13,72,)
CALL PLT55(2,1,)
RETURN
END

SUBROUTINE TRAFIT
C This routine functions essentially as MAXFIT, except that the first
C Maxwellian can be a translating Maxwellian.
BYTE TDATE(81),RUNNO(5),ERR
COMMON /RUNUM/ RUNNO
REAL MAXWEL,TRANS,DECONV(309),MAX1,MIN1
MAXWEL(U)=EXP(-(U*U))*U**4
TRANS(U,U)=EXP(-(U-U)**2))*U**4
INTEGER GRAPH(512)
COMMON /DECD/ DECONV,MAX1,MIN1,ICHNL1,GTO
5 TYPE 10
10  FORMAT ('+How many species? ',)
ACCEPT 20,NSPEC
20  FORMAT (I3)
IF (NSPEC .EQ. 1 .OR. NSPEC .EQ. 2) GOTO 40
TYPE 30
30  FORMAT ('+1 or 2 only!'/)
GOTO 5
40  ZERO=0.
TYPE 50
50  FORMAT ('+Flight path (cm.): ',)
ACCEPT 60,PATH
60  FORMAT (F9.4)
TYPE 70
70  FORMAT ('+Period (msec.): ',)
ACCEPT 60,PERIOD
TYPE 80
80  FORMAT ('+Eductor delay (usec.): ',)
ACCEPT 60,DELAY
TO=GTO-(DELAY+3.)*.103/PERIOD
PERIOD=PERIOD/1000.
ITO=INT(TO+1.)

```

```

      IZERO=INT(5.*(T0-ICHNL1))
      IZ=IZERO
      IF (IZERO .LT. 0) IZERO=0
      TYPE 83
83      FORMAT ('+Molecular weight: ',%)
      ACCEPT 60,WEIGHT
      GOTO (85,120) NSPEC
85      TYPE 90
90      FORMAT ('+Temperature (centigrade): ',%)
      ACCEPT 60,TEMP
      TEMP=TEMP+273.15
      TSCALE=SQRT(WEIGHT/TEMP*6.01659E-9)*PATH
      TYPE 115
115     FORMAT ('+Mach number: ',%)
      ACCEPT 60, SR
      U=SR*1.128379          !Sets SR (Mach no.) to be ratio of U to square
      GOTO 150              !root of (8kT/[pi]m)
120     TYPE 130
130     FORMAT ('+Translating Maxwellian-- '
      +/'      Temperature (centigrade): ',%)
      ACCEPT 60,TEMP
      TEMP=TEMP+273.15
      TSCALE=SQRT(WEIGHT/TEMP*6.01659E-9)*PATH
      TYPE 135
135     FORMAT ('+      Mach number: ',%)
      ACCEPT 60,SR
      U=SR*1.128379
      TYPE 140
140     FORMAT ('+Regular Maxwellian--'/'      Temperature: ',%)
      ACCEPT 60,TEMP
      TEMP=TEMP+273.15
      TSCALE=SQRT(WEIGHT/TEMP*6.01659E-9)*PATH
150     TYPE 160
160     FORMAT ('+How many channels are "zero"? ',%)
      ACCEPT 20,NZERO
      DO 170, I=ITO+NZERO,ITO+NZERO-1
170     ZERO=ZERO+DECONV(I)
      ZERO=ZERO/NZERO/2
      IY=INT((ZERO-MIN1)*201./(MAX1-MIN1))+17
      DO 180, I=0,IZERO+3
180     GRAPH(I+1)=IY
      GOTO (200,250) NSPEC
C      SINGLE MAXWELLIAN FIT:
200     S1=0.
      S2=0.
204     TYPE 205
205     FORMAT ('+What fraction do you want to fit (starting
      +from right)? ',%)
      ACCEPT 206,FRACT
206     FORMAT (F6.4)
      IF (FRACT .GT. 0. .AND. FRACT .LE. 1.) GOTO 208
      TYPE 207
207     FORMAT ('+Huh? Between 0. and 1. please!')
      GOTO 204
208     START=INT(103*(1-FRACT))
      TMAX=-100000.
      IF (START .LT. NZERO/2) START=NZERO/2
      DO 210, I=ITO+START,ITO+102
      V=103./(I-T0)/PERIOD*TSCALE
      TMAX=AMAX1(TMAX,TRANS(V,U))
      S1=S1+(DECONV(I)-ZERO)*TRANS(V,U)
210     S2=S2+TRANS(V,U)**2
      AMP=S1/S2
      DO 220, I=IZERO+1,511
      IF (I .LE. 0) GOTO 220
      V=512./(I-IZERO)/PERIOD*TSCALE

```

```

Y=AMP*TRANS(V,U)+ZERO
GRAPH(I+4)=INT((Y-MIN1)*201./(MAX1-MIN1))+17
IF (GRAPH(I+4) .LT. 0) GRAPH(I+4)=0
IF (GRAPH(I+4) .GT. 235) GRAPH(I+4)=235
220 CONTINUE
GOTO 300
C
250 DOUBLE MAXWELLIAN FIT:
S1=0.
S2=0.
S3=0.
S4=0.
S5=0.
TMAX=-100000.
DO 260, I=ITO+NZERO/2, ITO+102
V1=103./(I-TO)/PERIOD*TSCAL1
V2=103./(I-TO)/PERIOD*TSCAL2
TMAX=AMAX1(TMAX, TRANS(V1,U))
S1=S1+TRANS(V1,U)**2
S2=S2+TRANS(V1,U)*MAXWEL(V2)
S3=S3+MAXWEL(V2)**2
S4=S4+(DECONV(I)-ZERO)*TRANS(V1,U)
260 S5=S5+(DECONV(I)-ZERO)*MAXWEL(V2)
DEN=S1*S3-S2*S2
AAMP=(S4*S3-S2*S5)/DEN
BAMP=(S1*S5-S4*S2)/DEN
DO 270, I=IZERO+1, 511
IF (I .LE. 0) GOTO 270
V1=512./(I-IZERO)/PERIOD*TSCAL1
V2=512./(I-IZERO)/PERIOD*TSCAL2
Y=AAMP*TRANS(V1,U)+BAMP*MAXWEL(V2)+ZERO
GRAPH(I+4)=INT((Y-MIN1)*201./(MAX1-MIN1))+17
IF (GRAPH(I+4) .LT. 0) GRAPH(I+4)=0
IF (GRAPH(I+4) .GT. 235) GRAPH(I+4)=235
270 CONTINUE
300 VAR=0.
DO 330, I=ITO+NZERO/2, ITO+102
GOTO (310,320) NSPEC
310 V=103./(I-TO)/PERIOD*TSCALE
TERM=AMP*TRANS(V,U)
GOTO 330
320 V1=103./(I-TO)/PERIOD*TSCAL1
V2=103./(I-TO)/PERIOD*TSCAL2
TERM=AAMP*TRANS(V1,U)+BAMP*MAXWEL(V2)
330 VAR=VAR+(DECONV(I)-ZERO-TERM)**2
C
PLOTTING ROUTINE
CALL PLOT55(13,72,)
CALL PLOT55(10,,)
CALL PLT55(1,1,)
CALL PLT55(2,167,314)
CALL PLT55(4,1,IY)
CALL PLT55(7,0,0)
CALL PLT55(3,-512,GRAPH)
CALL PLOT55(1,0,)
CALL PLT55(6,IZ,1)
CALL PLOT55(9,44,0)
CALL DATE(TDATE)
TYPE 335,TDATE
335 FORMAT ('+',9A1)
CALL PLOT55(9,44,1)
TYPE 340
340 FORMAT ('+Run #',%)
CALL PUTSTR(7,RUNNO,'+')
CALL PLT55(9,44,3)
GOTO (350,370) NSPEC
350 CALL SCOPY('Fit amplitude: %',TDATE)
CALL REPL(TDATE,AMP*TMAX)

```

91

```

      CALL PLTTXT(TDATE)
      CALL PLT55(9,44,6)
      CALL SCOPY('Temperature: ##',TDATE)
      CALL PLTREI(TDATE,INT(TEMP))
      CALL PLTTXT(TDATE)
C      Print degree sign on terminal and plotter.
      CALL PLOT55(13,70,)
      TYPE 366
366  FORMAT ('+°K, ',)
      CALL PLOT55(13,71,)
      CALL PLTSTA(ISTAT)
      GOTO (368,367) ISTAT+1
367  CALL SCOPY('UC1,S,99,1,1,0,1,-1,1,-1,-1,0,-1,
      +1,-1,-99;L&K ',TDATE)
      CALL PLTSND(TDATE)
C      Continue other printing.
368  CALL SCOPY('Mach #: ##',TDATE)
      CALL PLTRER(TDATE,SR)
      CALL PLTTXT(TDATE)
      GOTO 400
370  CALL SCOPY('Coefficient for Maxwellian: ##',TDATE)
      CALL REPL(TDATE,BAMP*4./EXP(2.))
      CALL PLTTXT(TDATE)
      CALL PLT55(9,44,4)
      CALL SCOPY('Coefficient for other peak: ##',TDATE)
      CALL REPL(TDATE,AAMP*TMAX)
      CALL PLTTXT(TDATE)
400  CALL PLT55(9,44,5)
      VAR=SQRT(VAR/(102-NZERO/2))/(MAX1-MIN1)*100.
      VAR=INT(VAR*10.)*.1
      CALL SCOPY('Standard deviation: ##%',TDATE)
      CALL PLTRER(TDATE,VAR)
      CALL PLTTXT(TDATE)
      GOTO (415,425) NSPEC
415  CALL PLOT55(9,35,10)
C      Allow change of temperature &/or Mach number without saving all else.
      TYPE 420
420  FORMAT('Another temperature &/or Mach number? ',)
      CALL GETSTR (5,TDATE,8,ERR)
      CALL SCOMP('YES',TDATE,IVAL)
      IF (IVAL .EQ. 0) GOTO 430
425  CALL PLOT55(13,72,)
      CALL PLT55(2,1,)
      RETURN
430  TYPE 90
      ACCEPT 60,TEMP
      TEMP=TEMP+273.15
      TSCALE=SQRT(WEIGHT/TEMP*6.01639E-9)*PATH
      TYPE 115
      ACCEPT 60,SR
      U=SR*1.128379
      S1=0.
      S2=0.
      GOTO 208
      END

      SUBROUTINE SUBMAX(ITYPE)
C      Subtracts a translating or static Maxwellian from data. Most details
C      are as they are in MAXFIT and TRAFIT.
      BYTE TDATE(S1),RUNNO(5),ERR
      COMMON /RUNUM/ RUNNO
      REAL MAXWEL,DECONV(309),MAX1,MIN1,DIFFER(309),MAX2,MIN2
      MAXWEL(V,U)=EXP(-((V-U)**2))*V**4
      INTEGER GRAPH(512)
      COMMON /DECD/ DECONV,MAX1,MIN1,ICHNL1,GTO
40  ZERO=0.
  
```

```

TYPE 50
50  FORMAT ('+Flight path (cm.): ',%)
ACCEPT 60,PATH
60  FORMAT (F9.4)
TYPE 70
70  FORMAT ('+Period (asec.): ',%)
ACCEPT 60,PERIOD
TYPE 80
80  FORMAT ('+Eductor delay (usec.): ',%)
ACCEPT 60,DELAY
TO=GTO-(DELAY+3.)*.103/PERIOD
PERIOD=PERIOD/1000.
IT0=INT(TO+1.)
TYPE 90
90  FORMAT ('+Temperature (centigrade): ',%)
ACCEPT 60,TEMP
TEMP=TEMP+273.15
GOTO (95,100) ITYPE
95  U=0.
GOTO 105
100 TYPE 101
101  FORMAT ('+Mach number: ',%)
ACCEPT 60,SR
U=SR*.128379
105 TYPE 110
110  FORMAT ('+Molecular weight: ',%)
ACCEPT 60,WEIGHT
TSCALE=SQRT(WEIGHT/TEMP*.01659E-9)*PATH
AMPMAX=-10000.
DO 120,I=1,103
U=103./I/PERIOD*TSCALE
120  AMPMAX=AMAX1(AMPMAX,MAXWEL(U,U))
185 TYPE 190
190  FORMAT ('+Maxwellian amplitude: ',%)
ACCEPT 60, AMP
AMP=AMP/AMPMAX
C  SUBTRACTION BEGINS HERE.
MAX2=-10000.
MIN2=10000.
DO 210, I=IT0+3,IT0+105
U=103./(I-T0)/PERIOD*TSCALE
DIFFER(I)=DECONV(I)-AMP*MAXWEL(U,U)
IF (I+206 .LE. 309) DIFFER(I+206)=DIFFER(I)
IF (I+103 .LE. 309) DIFFER(I+103)=DIFFER(I)
IF (I-103 .GE. 1) DIFFER(I-103)=DIFFER(I)
MAX2=AMAX1(MAX2,DIFFER(I))
210 MIN2=AMIN1(MIN2,DIFFER(I))
DO 220, IX=0,505,5
IY=INT((DIFFER(ICHNL1+IX/5)-MIN2)*201./(MAX2-MIN2))+17
DO 220, I=1,5
220  GRAPH(IX+I)=IY
IY=INT((DIFFER(ICHNL1+102)-MIN2)*201./(MAX2-MIN2))+17
GRAPH(511)=IY
GRAPH(512)=IY
C  PLOTTING ROUTINE
CALL PLOTSS(13,72,)
CALL PLOTSS(10,,)
CALL PLOTSS(1,0,)
CALL PLOTSS(2,512,)
CALL PLTSS(2,11,500)
CALL PLTSS(7,0,0)
CALL PLTSS(3,-512,GRAPH)
CALL PLTSS(9,44,0)
CALL DATE(TDATE)
TDATE(10)=0
CALL PLTTXT(TDATE)

```





```

+
CALL PLOT33(9,0,16)
IFLAG=0
C IFLAG identifies direction of slope. 6 points on either side of
C current location are summed.
SUMLO=DECONV(ICHNL1)+DECONV(ICHNL1+1)+DECONV(ICHNL1+2)
++DECONV(ICHNL1+3)+DECONV(ICHNL1+4)+DECONV(ICHNL1+5)
SUMHI=DECONV(ICHNL1+7)+DECONV(ICHNL1+8)+DECONV(ICHNL1+9)
++DECONV(ICHNL1+10)+DECONV(ICHNL1+11)+DECONV(ICHNL1+12)
DIFF=SUMHI-SUMLO
IF (DIFF .GT. 0) IFLAG=1
DO 190, I=ICHNL1+6, ICHNL1+70
SUMLO=SUMLO-DECONV(I-6)+DECONV(I)
SUMHI=SUMHI-DECONV(I+1)+DECONV(I+7)
DIFF=SUMHI-SUMLO
IF (IFLAG .EQ. 0 .AND. DIFF .LT. 0
+ .OR. IFLAG .EQ. 1 .AND. DIFF .GE. 0) GOTO 190
IF (IFLAG .EQ. 0 .AND. DIFF .GE. 0) GOTO 185
180 TYPE 180, I+1-ICHNL1, (I+1.5-T0)/1.03E-4*PERIOD, DECONV(I+1)-ZERO
FORMAT ('+Peak in channel', I4, ' (' , F5.0, ' microseconds) with
+ amplitude: ', F9.0/)
IFLAG=0
CALL PLOT33(1,0,)
CALL PLOT33(2,128,)
C Mark peaks.
CALL PLOT33(6,5*(I+1-ICHNL1)-3,1)
GOTO 190
185 IFLAG=1
190 CONTINUE
C Calculate and print average velocity.
S1=0.
S2=0.
DO 210, I=IT0+NZERO/2, IT0+102
V=PATH/(I-T0)*103./PERIOD
S1=S1+V*(DECONV(I)-ZERO)
210 S2=S2+DECONV(I)-ZERO
TYPE 220, S1/S2
220 FORMAT ('+Average velocity: ', F7.0, ' centimeters per second.')
CALL PLOT33(13,72,)
RETURN
END

SUBROUTINE SMOOTH
BYTE TDATE(81), RUNNO(5), ERR
COMMON /RUNUM/ RUNNO
INTEGER GRAPH(512)
REAL IN(309), OUT(309), MAX1, MIN1
COMMON /DECD/ IN, MAX1, MIN1, ICHNL1 /BKS/ BK(103)
TYPE 3
3 FORMAT (' This routine smooths data by digital low-pass
+ filtering.')
C Lambda is set to 80. dB, Delta is set to about 2.5 components.
C This sets NP to 103, giving good accuracy and reasonable run-time.
C See Kaiser and Reed, R.S.I. 48:1447 (1977) for details and for
C modifications.
5 TYPE 10
10 FORMAT (' How many Fourier components to be kept? ', 5)
ACCEPT 20, BETA
20 FORMAT (F8.2)
IF (BETA .LT. 52.) GOTO 22
TYPE 21
21 FORMAT ('+Maximum number is 52!')
GOTO 5
22 BETA=2.*BETA/103.
IFLAG=0
CALL NER(BETA)

```

```

DO 40, N=1,103
OUT(N)=0.
DO 30, K=-103,103
30 OUT(N)=OUT(N)+BK(IABS(K)+1)*IN(N+103-K)
OUT(N+204)=OUT(N)
40 OUT(N+103)=OUT(N)
C PLOTTING ROUTINE
DO 50, IX=0,505,5
IY=INT((OUT(ICHNL1+IX/5)-MIN1)*201./(MAX1-MIN1))+17
DO 50, I=1,5
50 GRAPH(IX+I)=IY
IY=INT((OUT(ICHNL1+102)-MIN1)*201./(MAX1-MIN1))+17
GRAPH(511)=IY
GRAPH(512)=IY
CALL PLOTSS(13,72,)
CALL PLOTSS(10,,)
CALL PLOTSS(1,1,)
CALL PLTSS(2,31,500)
CALL PLTSS(7,0,0)
CALL PLTSS(3,-512,GRAPH)
CALL PLTSS(9,44,0)
CALL DATE(TDATE)
TDATE(10)=0
CALL PLTTXT(TDATE)
CALL PLTSS(9,44,1)
CALL SCOPY('Run #',TDATE)
CALL CONCAT(TDATE,RUNNO,TDATE)
CALL PLTTXT(TDATE)
CALL PLTSS(9,44,2)
CALL SCOPY('Full scale amplitude: ##',TDATE)
CALL REPL(TDATE,MAX1-MIN1)
CALL PLTTXT(TDATE)
CALL PLOTSS(9,35,10)
TYPE 90
90 FORMAT ('+Another try? ',S)
CALL GETSTR(5,TDATE,8,ERR)
CALL SCOMP('YES',TDATE,IVAL)
IF (IVAL .EQ. 0) GOTO 5
CALL PLOTSS(9,35,11)
C Either replace DECONV with smoothed version, or simply abort routine.
TYPE 100
100 FORMAT ('+Save smoothed version? ',S)
CALL GETSTR(5,TDATE,8,ERR)
CALL SCOMP('YES',TDATE,IVAL)
CALL PLTSS(2,11,500)
IF (IVAL .NE. 0) RETURN
CALL PLOTSS(1,0,)
CALL PLOTSS(3,-512,GRAPH)
DO 110, I=1,309
110 IN(I)=OUT(I)
RETURN
END

SUBROUTINE MER(BE)
COMMON /BKS/ BK(103)
PI=3.141592654
FK=10.0344
ET=7.85726
CALL INO(ET,FIA)
DO 10, K=1,103
GK=PI*FLOAT(K)
GE=ET*SQR(1.-(FLOAT(K)/103)**2)
CALL INO(GE,E)
BK(K)=(SIN(BE*GK)/GK)*(E/FIA)
10 CONTINUE
DO 20, I=2,104

```

```

      K=104-I+2
      J=K-1
20    BK(K)=BK(J)
      BK(1)=BE
      RETURN
      END

      SUBROUTINE INO(X,S)
      S=1.
      DS=1.
      D=0.
1     D=D+2.
      DS=DS**X/(D*D)
      S=S+DS
      IF (DS .GT. 0.2E-8*S) GOTO 1
      RETURN
      END

      SUBROUTINE READER
      Read in new spectrum via a/d or old from disk.
      INTEGER DATA(206),IDATA(100)
      BYTE ANSWER(5),RUNNO(3),TEMP(11),FILNAM(15),ERR,NAME(7)
      COMMON /RAWD/ DATA,MIN,MAX, /RUNUM/ RUNNO
      ICMF=0
      MIN=10000
      MAX=-10000
      C     Set values for missing channels to be interpolated.
      DATA(101)=2048
      DATA(102)=2048
      DATA(103)=2048
      5     TYPE 10
10    FORMAT('+NEW or OLD? ',3)
      CALL GETSTR(5,ANSWER,4,ERR)
      CALL SCOMP('NEW',ANSWER,IVAL)
      IF (IVAL .EQ. 0) GOTO 100
      CALL SCOMP('OLD',ANSWER,IVAL)
      IF (IVAL .EQ. 0) GOTO 200
      TYPE 20
20    FORMAT ('+What?'/)
      GOTO 5
100   TYPE 110
110   FORMAT ('+Run no.: ',3)
      C     Create temporary data file 'DX1:RUN.DAT'
      CALL GETSTR(5,RUNNO,4,ERR)
      CALL CONCAT('DX1:RU',RUNNO,TEMP)
      CALL CONCAT(TEMP,'.DAT',FILNAM)
      CALL ASSIGN(2,FILNAM,0)
      TYPE 120
120   FORMAT(' Ready with data? ',3)
      CALL GETSTR(5,TEMP,10,ERR)
      CALL RTS(IDATA,100,,,,,4,ICMF,IBEF)      !read in data at clock rate
      CALL LWAIT(ICMF,0)                        !provided at ST1 input.
      DO 125, I=1,100
125   DATA(I)=IDATA(I)
      CALL PUTSTR(2,RUNNO,0)
      WRITE (2,130) (DATA(I),I=1,103)
130   FORMAT (25I3)
      GOTO 300
200   TYPE 210
210   FORMAT('+File name: ',3)
      ERR=.FALSE.
      CALL GETSTR(5,NAME,6,ERR)
      IF (.NOT. ERR) GOTO 230
      TYPE 220
220   FORMAT('+6 characters maximum for file name!'/)
      GOTO 200

```

```

230      CALL CONCAT('DX1:',NAME,TEMP)
      CALL CONCAT(TEMP,'.DAT',FILNAM)
      CALL ASSIGN(2,FILNAM,0)
232      TYPE 110
      CALL GETSTR(5,ANSWER,4,ERR)
235      READ (2,240,END=260) RUNNO(1)
240      FORMAT (A1)
      BACKSPACE 2
      CALL GETSTR(2,RUNNO,4,ERR)
      READ (2,250)(DATA(I),I=1,103)
250      FORMAT(25I5)
      IF (ISCOMP(RUNNO,ANSWER)) 235,300,235
260      TYPE 270
270      FORMAT('No such runno. '//)
      REWIND 2
      GOTO 232
300      CALL CLOSE(2)
      DO 310, I=1,103
      DATA(I+103)=DATA(I)
      MIN=MINO(MIN,DATA(I))
310      MAX=MAXO(MAX,DATA(I))
      RETURN
      END

```

```

SUBROUTINE JOIN
C      Produce composite file for a set of temporary files by reading in
C      each file and writing them out into one new file. This is necessary
C      to avoid to inefficient concatenation achieved by the monitor COPY
C      command, which does not eliminate blank spaces.
      BYTE ANSWER(11),ERR,IVAL,JVAL,FILNAM(15),TEMP(11)
5      TYPE 10
10      FORMAT ('+Output file: ',S)
      CALL NAME(ERR,FILNAM)
      IF (ERR .EQ. .TRUE.) GOTO 5
      CALL ASSIGN(2,FILNAM,0)
15      TYPE 20
20      FORMAT ('+Are files consecutively numbered starting with 1? ',S)
      CALL GETSTR(5,ANSWER,10,ERR)
      CALL SCOMP('YES',ANSWER,IVAL)
      IF (IVAL .EQ. 0) GOTO 30
      CALL SCOMP('NO',ANSWER,JVAL)
      IF (JVAL .EQ. 0) GOTO 30
      TYPE 25
25      FORMAT ('+What? '//)
      GOTO 5
30      TYPE 40
40      FORMAT ('+How many files? ',S)
      ACCEPT 50, NFILES
50      FORMAT (I3)
      IF (IVAL .NE. 0) GOTO 200
      IF (NFILES .LT. 100) GOTO 70
      TYPE 60
60      FORMAT ('+Maximum of 99 consecutive files allowed. '//)
      GOTO 15
70      DO 100, I=1,NFILES
      IF (I .GE. 10) GOTO 80
      CALL CONCAT('DX1:RU',48+I,TEMP)
      GOTO 90
80      CALL CONCAT('DX1:RU',48+I/10,FILNAM)
      CALL CONCAT(FILNAM,48+I-10*(I/10),TEMP)
90      CALL CONCAT(TEMP,'.DAT',FILNAM)
100      CALL TRANSF(FILNAM)
      CALL CLOSE(2)
      RETURN
200      DO 230, I=1,NFILES

```

```

210     TYPE 220,I
220     FORMAT ('+File #',I4,': ',s)
        CALL NAME(ERR,FILNAM)
        IF (ERR.EQ..TRUE.) GOTO 210
230     CALL TRANSF(FILNAM)
        CALL CLOSE(2)
        RETURN
        END

        SUBROUTINE NAME(ERR,FILNAM)
        BYTE ERR,ANSWER(7),TEMP(11),FILNAM(15)
        ERR=.FALSE.
        CALL GETSTR(5,ANSWER,6,ERR)
        IF (ERR.EQ..FALSE.) GOTO 20
        TYPE 10
10      FORMAT ('+6 characters maximum for file name.//')
        RETURN
20      CALL CONCAT('DX1:',ANSWER,TEMP)
        CALL CONCAT(TEMP,'.DAT',FILNAM)
        RETURN
        END

        SUBROUTINE TRANSF(FILNAM)
        INTEGER DATA(103)
        BYTE FILNAM(15),ANSWER(6),ERR
        CALL SIGN(5,FILNAM,0)
        CALL GETSTR(3,ANSWER,4,ERR)
        READ (3,10) (DATA(I),I=1,103)
10      FORMAT (25I5)
        CALL PUTSTR(2,ANSWER,0)
        WRITE (2,10) (DATA(I),I=1,103)
        CALL CLOSE(3)
        RETURN
        END

```

## APPENDIX C. SOME THOUGHTS ON FITTING THEORY TO TIME-OF-FLIGHT DATA

Early time-of-flight work (eg. [45]) was able to extract only a few moments of a velocity distribution, in part, because of the shutter function deconvolution problem, and also because the higher moments magnify the effects of even small amounts of noise in the first part of a time-of-flight spectrum. Most workers [eg. 46, 61, 62] now fit Maxwellians where appropriate (as we have done) with varying degrees of mathematical sophistication (ranging from peak height matching to non-linear least-squares fitting to determine temperature). For nozzle beams, translating Maxwellians generally work (as in our data; see Figure 15); others have used the sum of two translating Maxwellians [64] or even a translating Maxwellian multiplied by a Hermite polynomial expansion [65].

Initially, it seemed attractive to devise a scheme which would fit some sort of expansion in terms of some set of orthogonal functions to the data. This gives a convenient analytic form which can be arbitrarily manipulated for comparison with theory, and in effect, smooths the data providing a representation in terms of a small set of fitting parameters. In practice, there are problems.

Basically, given sufficient parameters to adjust, and a functional form which is approximately correct, one can readily make a fit to most any set of experimental data. The problem is to choose a function whose parameters can readily be fitted to the data (i.e., the function should be linear in the fitting parameters), and which approaches the data with just a few terms. For velocity distributions, a polynomial times an exponential is the obvious choice. Hermite polynomials are attractive, because the expansion coefficients are closely related to the moments of

the distribution. However, evaluating these coefficients amounts to calculating moments, which is difficult to impossible beyond the first three or so, if there is appreciable noise in the early steep high velocity part of the time-of-flight curve. Examples of such an attempt are shown in Figure 40. A better choice is to select a set of polynomials which are explicitly orthogonal over the data spacing with respect to the exponential weighting function:

$$\sum_{i=1}^N P_n(v_i) P_m(v_i) e^{-2(v_i-u)^2} \propto \delta_{nm} \quad (C.1)$$

Such a set of polynomials can be readily generated, although they must be regenerated for each particular data spacing<sup>\*</sup>. The advantage of this orthogonality relation is that the matrix inversion necessary to calculate the expansion coefficients becomes trivial (see below), and successive terms in the expansion can be added without recalculating previous ones. If we choose to set the (somewhat arbitrary) translational velocity,  $u$ , in the exponential equal to zero, we have an expansion in time domain of the form:

$$f\left(\frac{1}{t}\right) = \sum_{i=0}^{\infty} B_i P_i\left(\frac{1}{t}\right) e^{-1/t^2} \quad (C.2)$$

We determine the  $B_i$  by least squares fitting; i.e., we require a minimum for:

$$\sum_{j=1}^N [f(v_j) - \sum_{i=0}^m B_i P_i(v_j) e^{-v_j^2}]^2 \quad (C.3)$$

where we take only  $m$  terms of the expansion and use  $v=1/t$  for convenience.

This gives a set of  $m+1$  equations:

---

\* These polynomials are related to the Gram polynomials which have a constant data spacing and no weighting function [66].

$$\sum_{i=0}^m B_i \sum_{j=1}^N P_k(v_j) P_i(v_j) e^{-2v_j^2} = \sum_{j=1}^N f(v_j) P_k(v_j) e^{-v_j^2} \quad k = 0 \rightarrow m \quad (C.4)$$

These equations are trivially solved if the following orthogonality relation holds:

$$\sum_{j=1}^N P_k(v_j) P_i(v_j) e^{-2v_j^2} = \delta_{ki} \quad (C.5)$$

It is this set of polynomials we wish to find. They can be determined by the following recurrence relations:

$$P_{j+1}(x) = (x - \alpha_{j+1}) P_j(x) - \beta_j P_{j-1}(x) \quad j = 0, 1, \dots$$

$$P_0(x) = 1, \quad P_{-1}(x) = 0$$

$$\alpha_{j+1} = \sum_{i=1}^N \omega_i x_i [P_j(x_i)]^2 / \sum_{i=1}^N \omega_i [P_j(x_i)]^2$$

$$\beta_j = \sum_{i=1}^N \omega_i [P_j(x_i)]^2 / \sum_{i=1}^N \omega_i [P_{j-1}(x_i)]^2$$

$$\omega_i = e^{-2x_i^2} \quad (C.6)$$

These relations are easily proven by induction.

For moderately noisy data, the expansion generated in this way behaves well to about 5 terms. For better data, about 10 terms can be obtained (see Figure 41). After these terms, the problem of magnifying the effect of small amounts of noise again becomes important, and the fitted curve starts to diverge from the data.

Being a purely mathematical construct, this kind of curve fitting or



smoothing tends to obscure rather than illuminate the physics of the situation. The exponential contains important physical information (Mach number, mass, temperature), which must be chosen arbitrarily. In the present experiments, many if not most time-of-flight spectra seem to consist of two to four components ("fast peak", "Maxwellian peak", two "slow peaks"; see Section 3.4.2.2). What best distinguishes these components is the exponential, not some polynomial. Especially in the case of incident beam data of the present experiments where the presence of particles of widely varying mass produce a distinctly non-Maxwellian spectrum, there seems to be nothing to be gained by finding an arbitrary analytic function to fit the data.

A final note of caution is in order for the interpretation of time-of-flight spectra. Often the peaks are sufficiently broad and noisy that any function of approximately the same shape and enough (even 3 or 4) fitting parameters can be made to fit. This does not, of course, give any indication of a reasonable theory. One must either reduce the number of fitting parameters to one or two by independently measuring the others, or at very least, show that calculated fitting parameters behave in predictable ways for different data.

#### APPENDIX D. SAMPLE EXPERIMENTAL PROCEDURE

Since the data have been presented in this document largely in a processed form, we present here an example of a typical experimental session. The details obviously depend on what particular experiment is being run, but an example can still give a feel for the sorts of procedures involved. We consider an experiment to survey a range of incident and scattering angles with the time-of-flight spectrometer for constant beam and surface conditions (cleaned silicon target).

Starting from standby status with the chamber evacuated to  $5 \times 10^{-6}$  Pa, the start-up procedure is as follows: The target is heated to  $130^\circ$  to drive off adsorbed material. The target is lowered out of the path of the beam. The liquid nitrogen cooling systems are started (valves are opened on a pressurized supply). The source boiler is refilled with distilled water, if necessary, and its heater is turned on. When all the liquid-nitrogen-cooled surfaces are near  $77^\circ$  K. (by thermocouple readings), and the boiler is up to the desired temperature, the source valve is opened. The source temperature controller is then activated and a nozzle temperature is selected. The target temperature is adjusted to the experimental value. These procedures generally take about an hour.

The time-of-flight equipment is turned on: ionizer, chopper, electron multiplier, amplifiers, Waveform Eductor, oscilloscope, and computer. An appropriate chopper period is selected (just long enough so that there is no overlap between consecutive spectra after deconvolution [52]) and gains are adjusted, and a delay is set on the Waveform Eductor (typically, so that the 3 channel dead time between sweeps spans the trigger pulse which may otherwise be picked up as signal). Before bringing the target into

position, a spectrum of the incident beam is recorded. (The chopper and ionizer are positioned to look at the beam.) When a satisfactory spectrum can be seen on the oscilloscope, it is read into the computer, deconvoluted, stored, and copied onto paper.

The target is now brought into position. For cold surface work, it is exposed to a normally incident beam for 15 minutes before proceeding. Then the target is set for the first incident angle (say  $75^\circ$ ), and the time-of-flight apparatus is positioned. For a broad survey a spectrum might be recorded at  $10^\circ$  increments in both scattering and incident angles. For each spectrum, recorded information might include time, run number, angles, period, temperatures of target, source, and boiler, chamber pressures, and any changes in other settings. The spectrum is read in and processed as for the incident beam. Spectra can typically be recorded at 3-4 minute intervals. This allows the Waveform Educator to average to its noise limit. A survey of the sort we describe might take about 5 hours total.

# APPENDIX E. EFFECTS OF MASS SPECTROMETER AMPLITUDE CORRECTIONS ON DETERMINATION OF SURFACE AND BULK ENERGIES OF CLUSTERS

Let  $N_n$  be the actual number of clusters of size  $n$  and  $A_n$  be experimental mass spectrum peak heights. Neglecting the possibility of fragmentation on ionization, we relate  $A_n$  to  $N_n$  by applying the corrections discussed in Section 3.1.1:

$$A_n = N_n \left( 0.6 \frac{10n}{14} + 0.4 \right) \left( \frac{18n+1}{28} \right)^{-\frac{1}{2}} 10^{-(18n+1-m_{th})/m_d} \quad (E.1)$$

for  $18n+1 > m_{th}$ . The quadrupole transmission is unity for  $18n+1 < m_{th}$  (the last factor in equation E.1 is set equal to 1 for  $18n+1 < m_{th}$ ).  $m_d$  is the decay constant for the transmission for  $18n+1 > m_{th}$ . Divide by  $A_1 = N_1 \alpha$ , where  $\alpha$  is a number obtained by setting  $n=1$  in equation E.1, and take the logarithm:

$$\ln \frac{A_n}{A_1} = \ln \frac{N_n}{N_1} - \ln \alpha + \ln \left( \frac{\frac{3}{2}n + 0.4}{\sqrt{18n+1}} \right) + \frac{1}{2} \ln 28 - 2.3 (18n+1-m_{th})/m_d \quad (E.2)$$

Now set  $\ln \frac{N_n}{N_1}$  equal to  $-A n^{2/3} + B n$  and rearrange terms:

$$\ln \frac{A_n}{A_1} = -A n^{2/3} + \left( B - \frac{(2.3)(18)}{m_d} \right) n + \ln \left( \frac{\frac{3}{2}n + 0.4}{\sqrt{18n+1}} \right) + \left[ \frac{1}{2} \ln 28 - \ln \alpha + 2.3 (m_{th} - 1) / m_d \right] \quad (E.3)$$

The expression in brackets is constant and does not affect the determination of other fitting coefficients. The  $\ln$  term is seen to be negligible if  $A$  and  $B$  are of at least order unity. It could be included for a more precise fitting. What remains is a small offset in  $B$  (since  $m_d$  is typically  $> 150$ ). There is no error in  $A$  as long as the  $\ln$  term can be neglected.

We can thus fit to the  $A_n$ 's without correction and make only small

errors in the determination of A and B, and fairly crude estimates of the correction factors allow quite precise determinations of A and B. In retrospect this makes sense. Since we are interested in the logarithm of the amplitudes, only corrections which go exponentially with n are important, and if that exponential can be made to decay much slower than the  $N_n$  themselves, almost no correction is necessary.

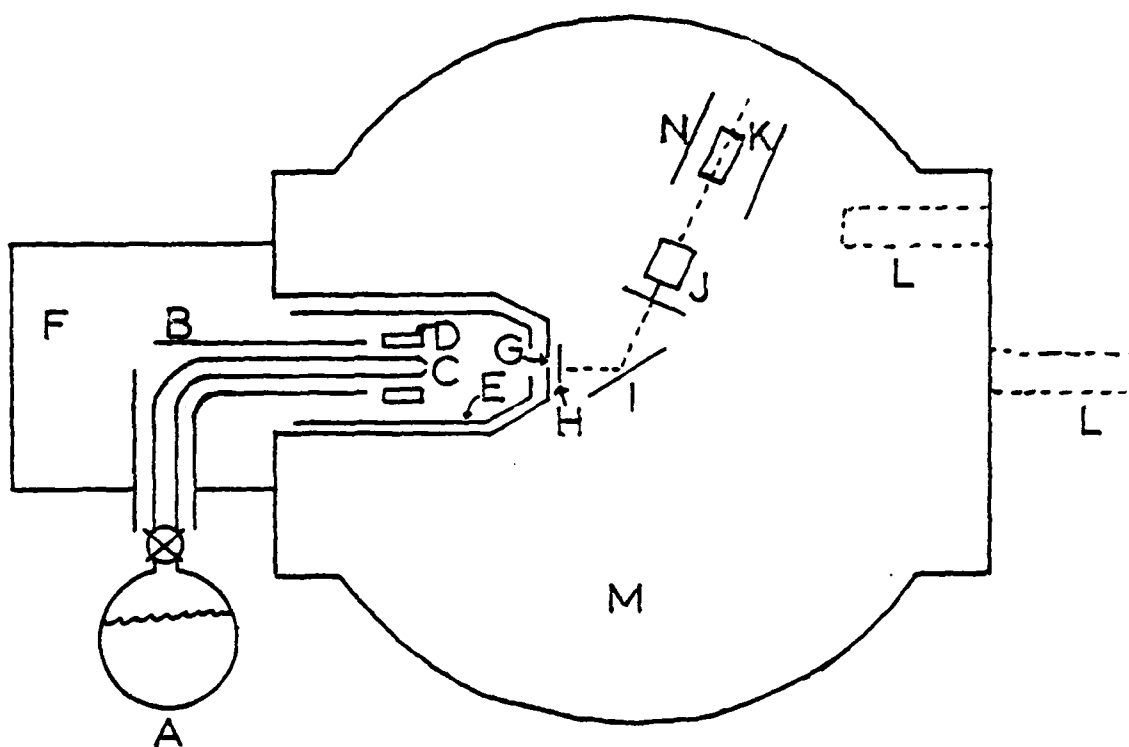


FIGURE 1. SCHEMATIC DIAGRAM OF APPARATUS

A - Temperature controlled boiler; B - Shielded heat pipe; C - Nozzle;  
D - Oven around nozzle; E - Liquid nitrogen-cooled inner wall;  
F - Collimating chamber; G - Collimating plate; H - Beam flag;  
I - Target; J - Chopper; K - Ionizer and electron multiplier;  
L - Quadrupole mass spectrometer (shown in the two positions used);  
M - Main vacuum chamber; N - Liquid nitrogen-cooled flow through enclosure.

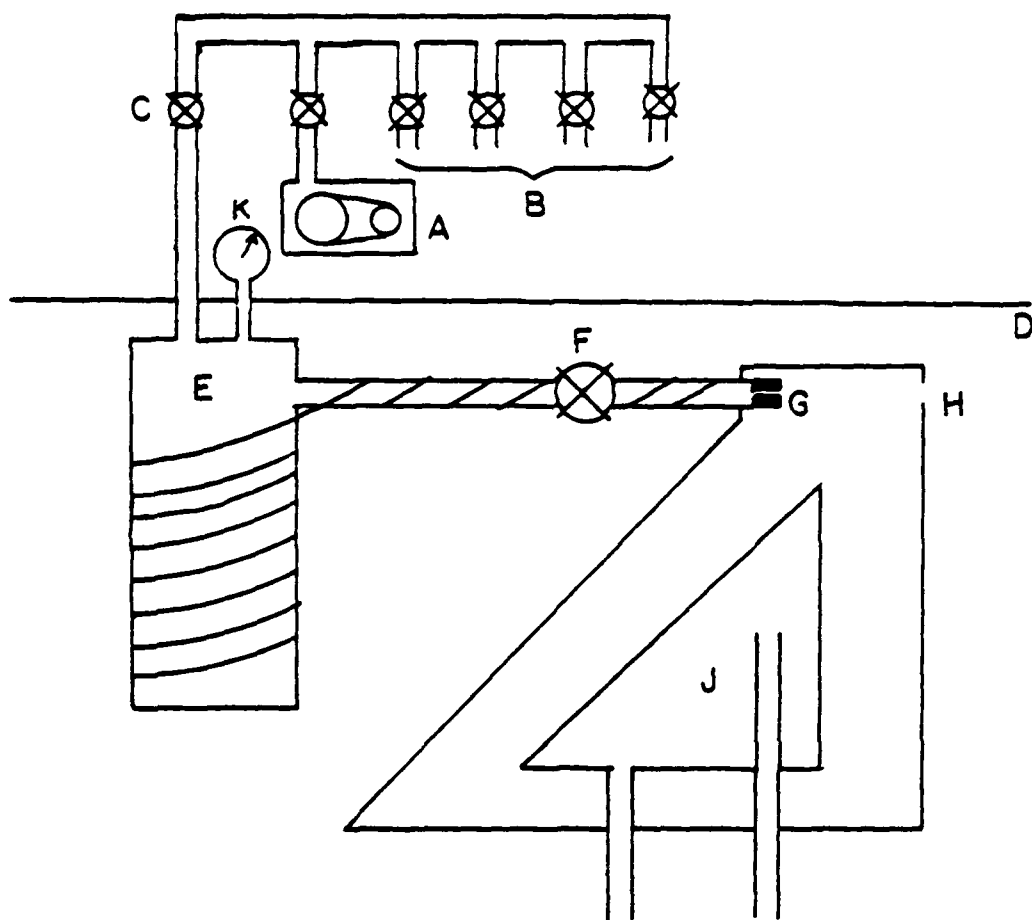


FIGURE 2. EARLY NOZZLE SOURCE ASSEMBLY

A - Vacuum pump; B - Gas supply manifold; C - Needle valve;  
D - Vacuum wall; E - Water reservoir with external heater;  
F - Motor-driven needle valve; G - Nozzle; H - Collimator;  
J - Liquid nitrogen reservoir; K - Capacitance manometer (pressure gauge).

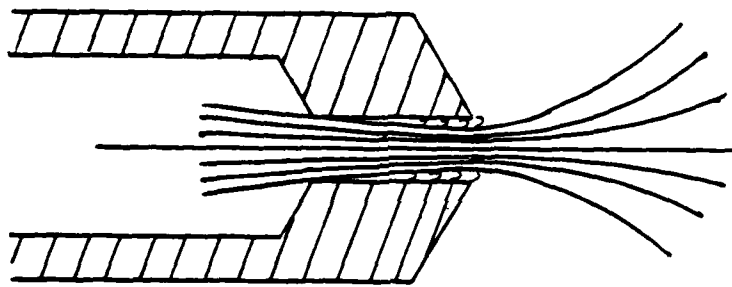


FIGURE 3. FLOW THROUGH CYLINDRICAL NOZZLE

The growing boundary layer through the cylindrical channel constricts the flow to give a converging-diverging flow pattern as in "supersonic" nozzles.



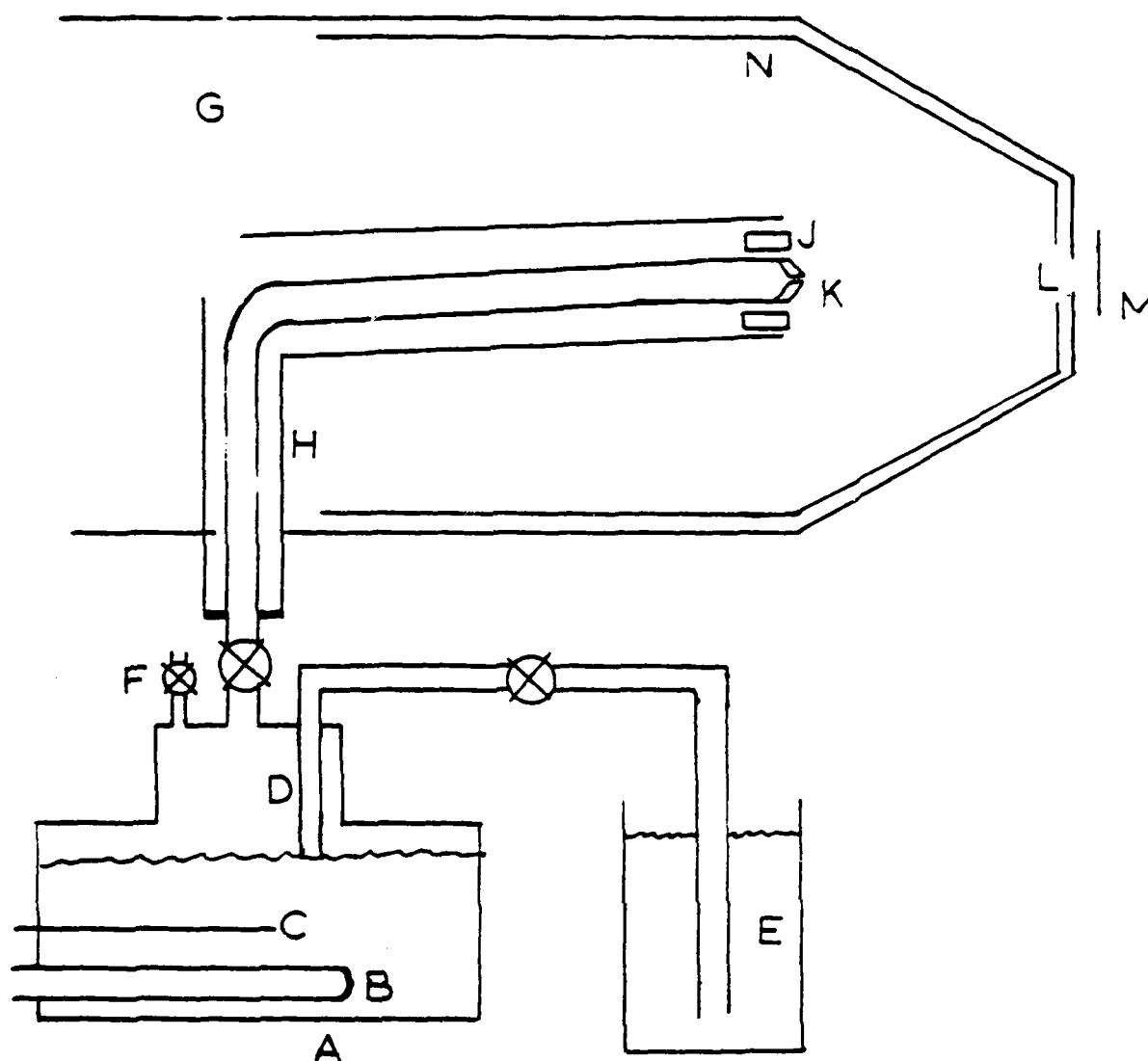


FIGURE 4. FINAL SOURCE ASSEMBLY

A - Stainless steel boiler; B - 1000W cartridge heater; C - Thermocouple;  
D - Fill tube; E - Distilled water supply bottle; F - Overpressure  
relief valve; G - Collimating chamber; H - Shielded heat pipe;  
J - 100W source oven; K - Nozzle (with another thermocouple, not shown);  
L - Collimator; M - Beam flag in main vacuum chamber; N - Liquid  
nitrogen-cooled inner wall.

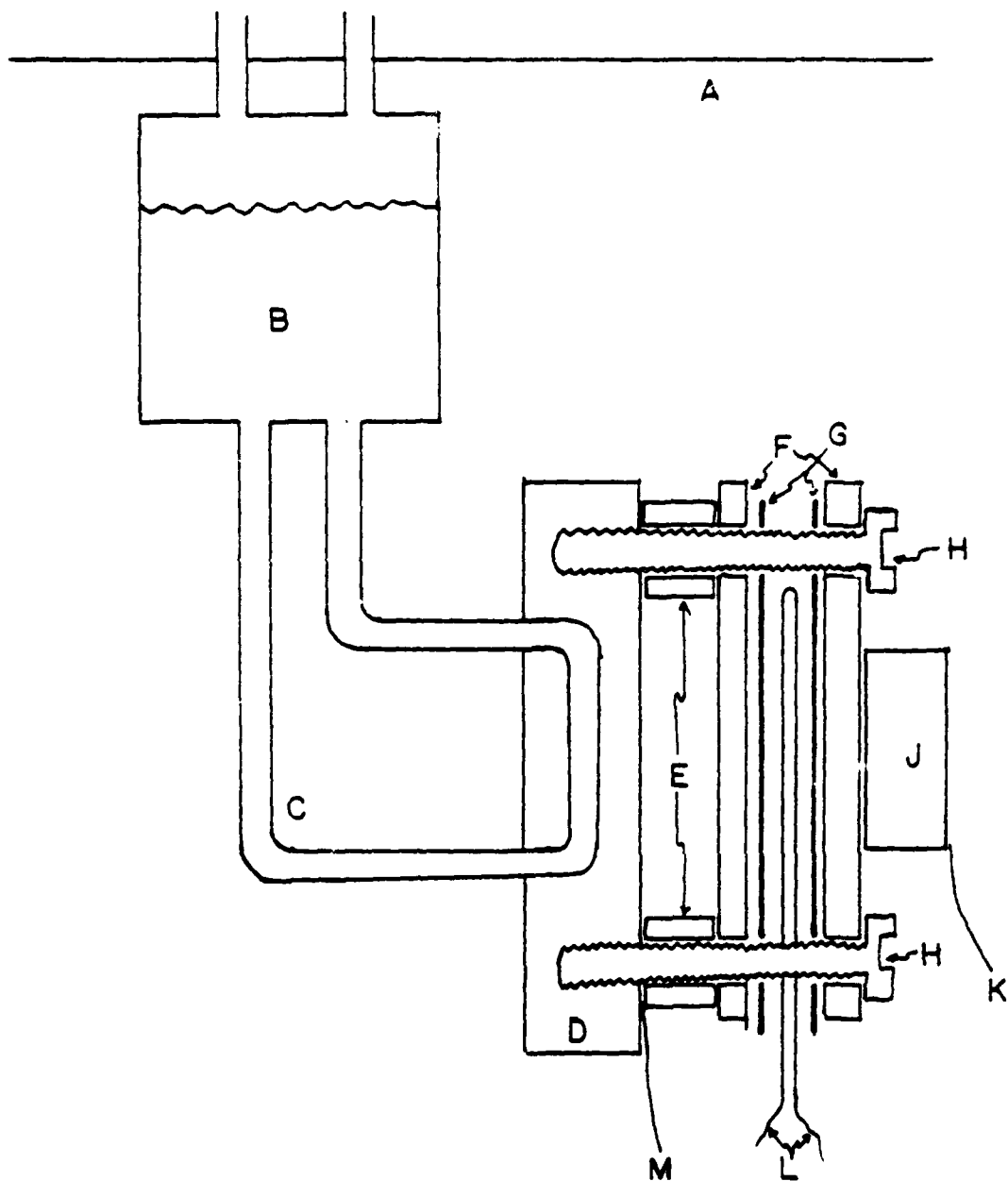


FIGURE 5. TARGET ASSEMBLY

Not to scale. Target  $\sim 2\times$  actual size, reservoir  $\sim 1/5$  actual size.  
 A - Vacuum wall; B - Liquid nitrogen reservoir; C - Flexible (stainless steel bellows) tubing; D - Liquid nitrogen-cooled copper block;  
 E - Alumina spacers; F - Copper plates; G - Mica sheets; H - Stainless steel screws; J - Target; K - Thermocouple; L - Nichrome wire;  
 M - Thermocouple.

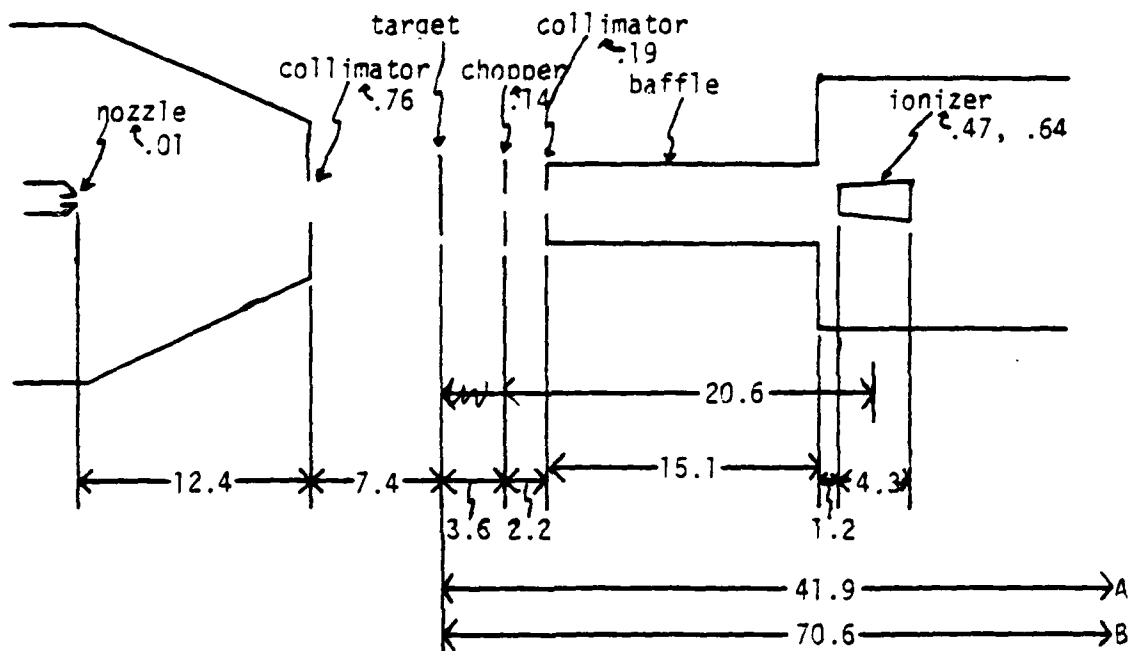


FIGURE 6. IMPORTANT DIMENSIONS OF BEAM SYSTEM, TARGET, AND TIME-OF-FLIGHT APPARATUS

All dimensions in cm. Dimensions next to labels give diameter of opening.  
 A - Mass spectrometer ionizer positioned for scattering measurements.  
 B - Mass spectrometer ionizer positioned for beam measurements.  
 Ionization region is tapered from .47 cm to .64 cm.

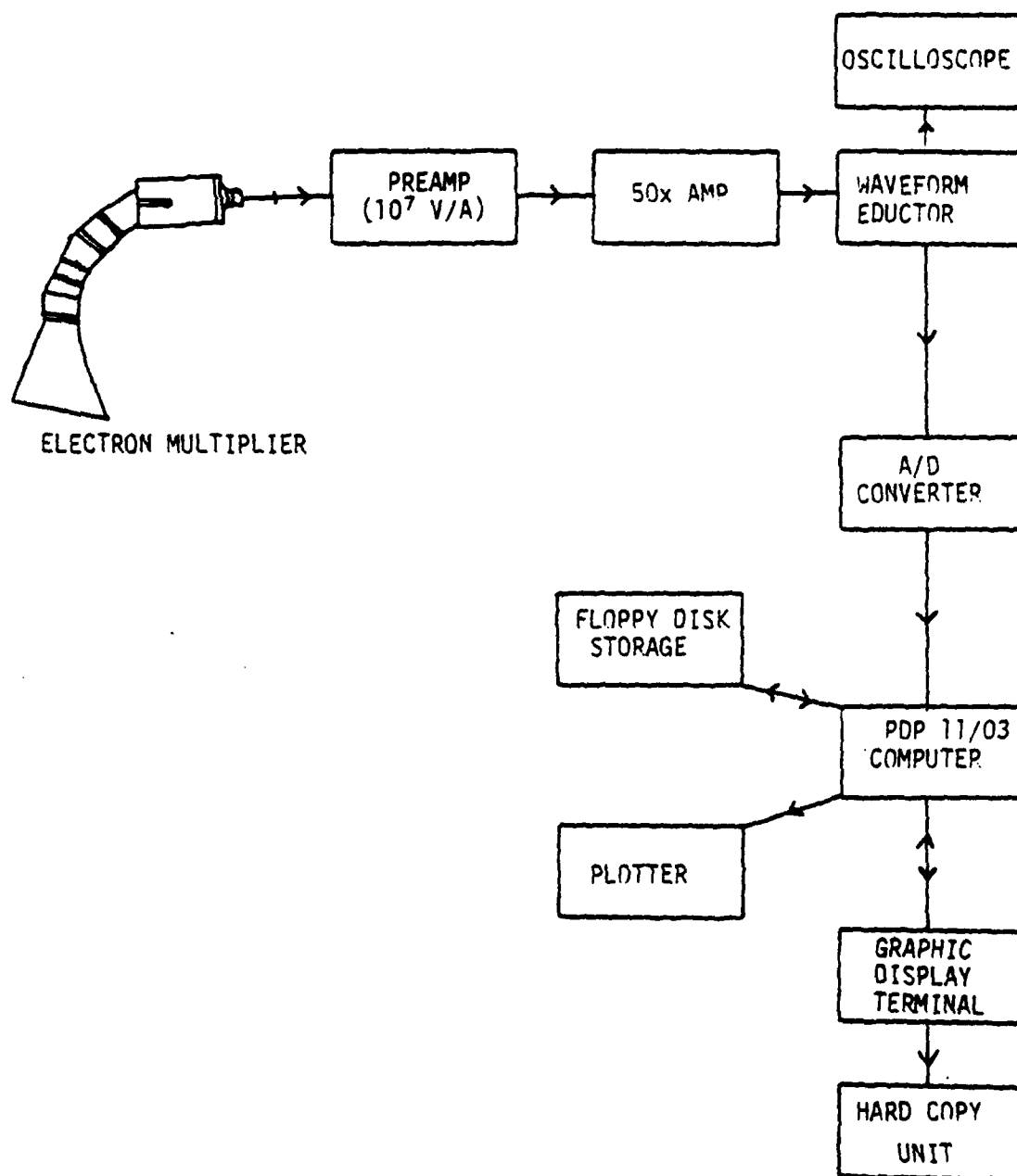


FIGURE 7. TIME-OF-FLIGHT SIGNAL PROCESSING

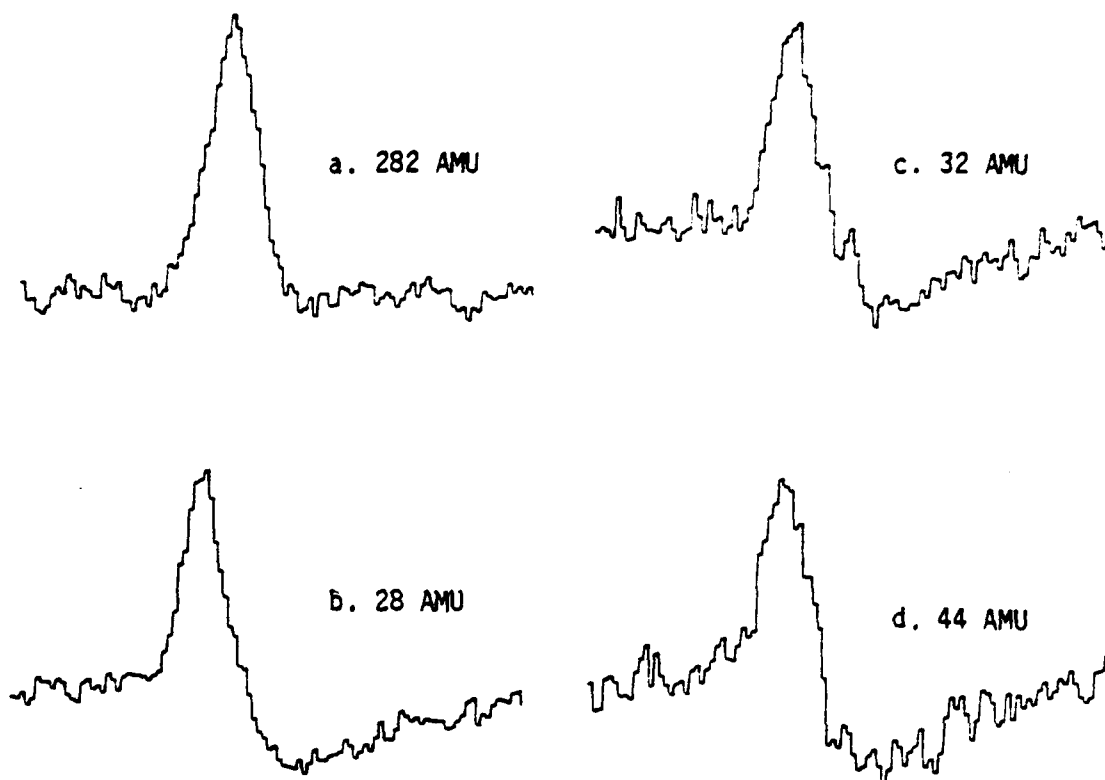


FIGURE 8. EXAMPLES OF MASS-FILTERED TIME-OF-FLIGHT SPECTRA FOR BACKGROUND SPECIES

(a)  $\text{H}_2\text{O}$  beam,  $P_0=1.1$  MPa,  $T_0=458^\circ$  K. Mass filter set at 282 AMU, flight path 70.6 cm\*, period 1.75 ms\*. Note that, although example (a) does not show a dip below zero, the shape of the curve is not typical of a velocity distribution; the steep portion is on the wrong side of the peak.  
 (b-d)  $\text{H}_2\text{O}$  beam,  $P_0=830$  kPa,  $T_0=466^\circ$  K, scattering from CuS at  $241^\circ$  K ( $\theta_i=\theta_s=72^\circ$ ). Period 1.92 ms\*, flight path 41.9 cm\*, mass filter set as marked.

\*In these and all time-of-flight spectra, time increases to the right, velocity to the left. They represent particle density in the ionizer versus time. To obtain velocity, divide the flight path by the time. There are 103 channels; each channel represents a time of  $1/103 \times$  period. The time origin is at or near the beginning of the trace and is marked on traces where a theoretical curve has been fitted. All spectra are plotted at the same amplitude (i.e. relative amplitude information is not shown).

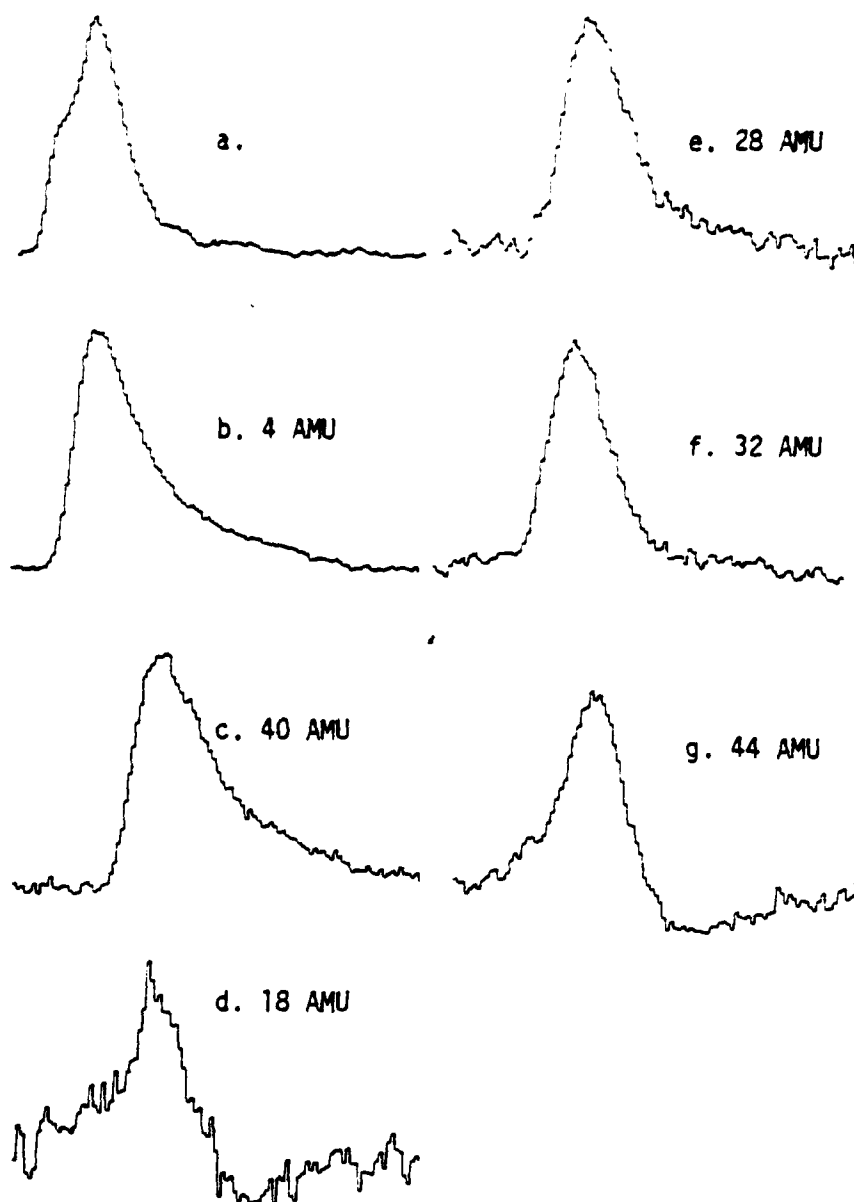


FIGURE 9. MASS-FILTERED TIME-OF-FLIGHT SPECTRA FOR MIXED Ar/He BEAM WITH  $N_2/O_2/H_2O/CO_2$  BACKGROUND

95% He + 5% Ar beam,  $P_0=7.1$  kPa,  $T_0=284^\circ$  K. (a) spectrum without mass-filtering, period 1.12 ms\*, flight path 20.6 cm\*. (b-g) mass-filtered spectra, period 2.92 ms\*, flight path 70.6 cm\*, mass filter set as indicated. Examples (e) and (f) might be mistaken for normal time-of-flight spectra, but note that the rising slope is not as steep as in (b) and (c).†

\*See footnote for Figure 8.

†The spectra could also be interpreted as an indication of air contamination in the source.

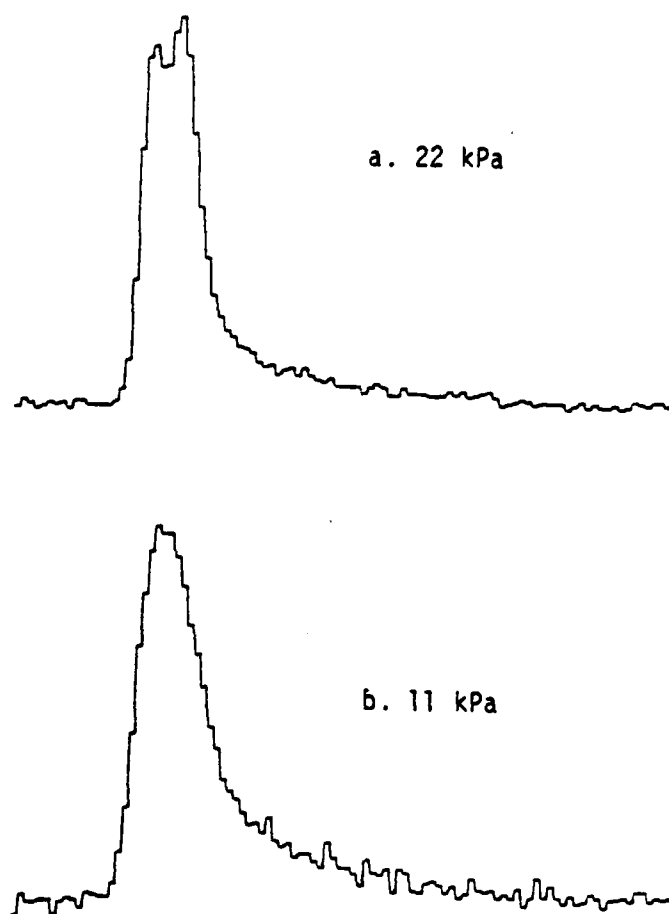


FIGURE 10. TIME-OF-FLIGHT SPECTRA OF ARGON BEAM

$T_0=308^\circ$  K,  $P_0$  as marked, period 1.62 ms\*, flight path 20.6 cm\*.

\*See footnote for Figure 8.

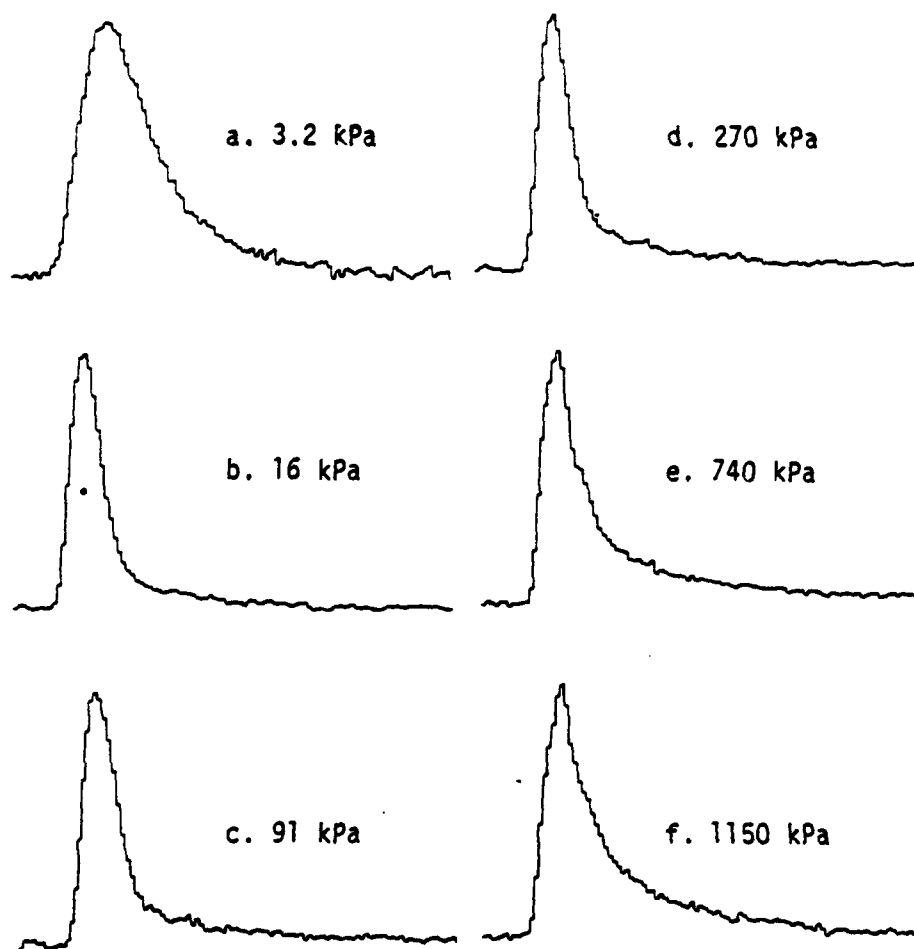


FIGURE 11. TIME OF FLIGHT SPECTRA OF WATER BEAM FOR VARYING SOURCE PRESSURE

$T_0=456^\circ \text{ K}$ ,  $P_0$  as marked, no mass filtering, periods (a,b) 1.07 ms, (c-f) .81 ms\*, flight path 20.6 cm\*. Note especially the appearance of an increasingly prominent low velocity tail at high pressure.

\*See footnote for Figure 8.



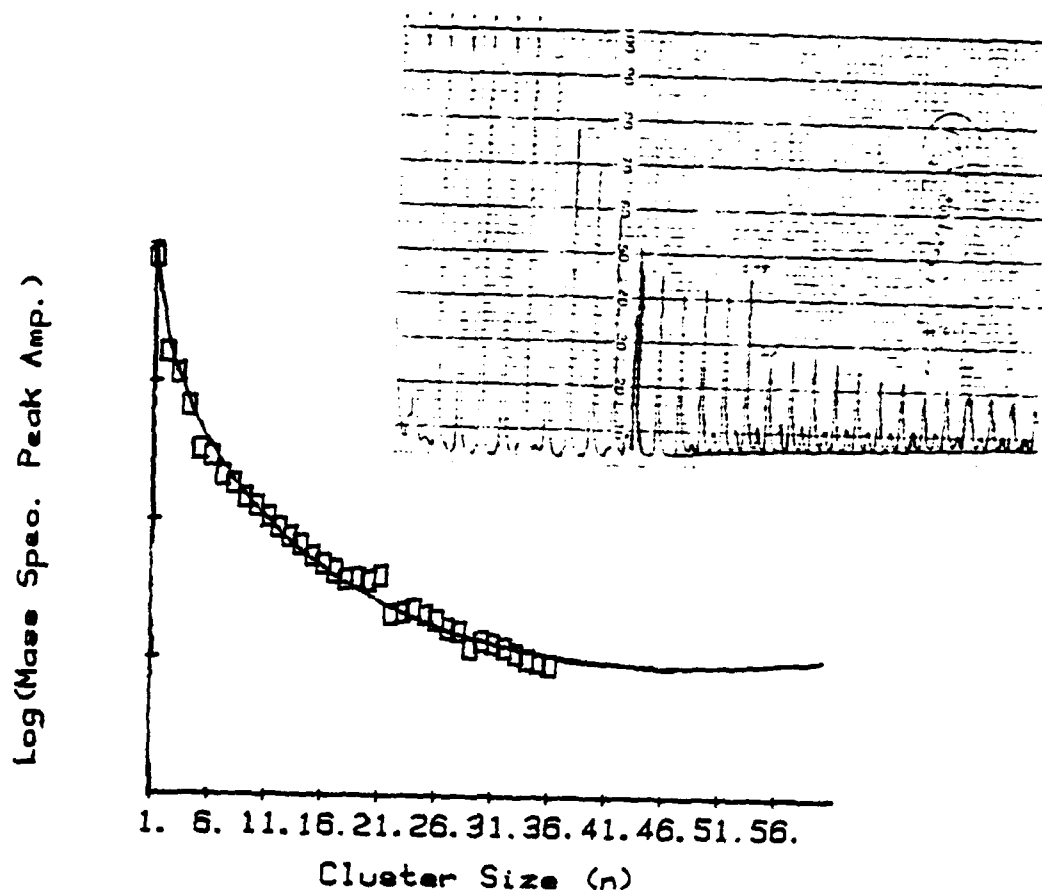


FIGURE 12. MASS SPECTRUM OF A HIGHLY-CLUSTERED WATER BEAM

$P_0=1.1$  MPa,  $T_0=458^\circ$  K. See Section 4.1 for an explanation of fitted curve. Chart recorder output illustrates peaks for half-integer cluster sizes.

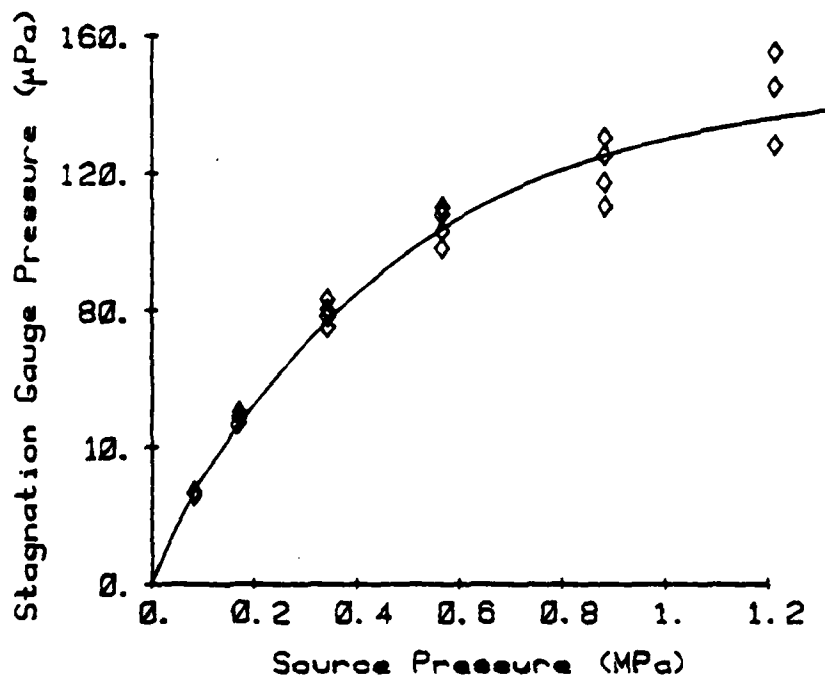


FIGURE 13. STAGNATION GAUGE INTENSITY VERSUS SOURCE PRESSURE

Range of points shown cover a temperature range of 400-500°K. The variation of intensity with source temperature is relatively small. Higher temperature results in lower intensity. Thus the lowest points at any fixed source pressure in the graph are for 500°K, and the highest are for 400°K.

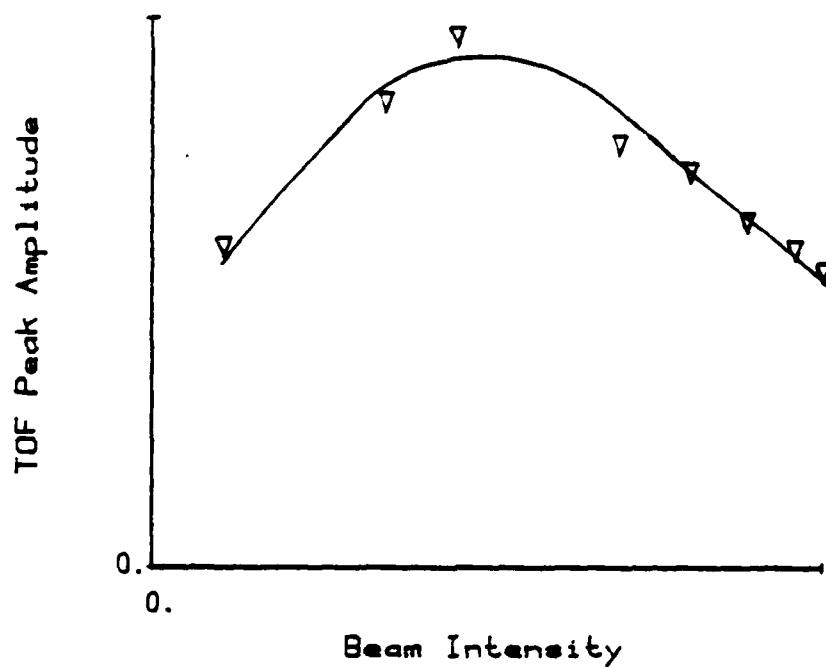


FIGURE 14. TIME-OF-FLIGHT PEAK AMPLITUDE VERSUS BEAM INTENSITY

Intensity at right corresponds to source conditions where beam appears highly clustered as indicated by the low velocity tail in the time-of-flight spectrum (Figure 11) ( $P_0=1.1$  MPa).

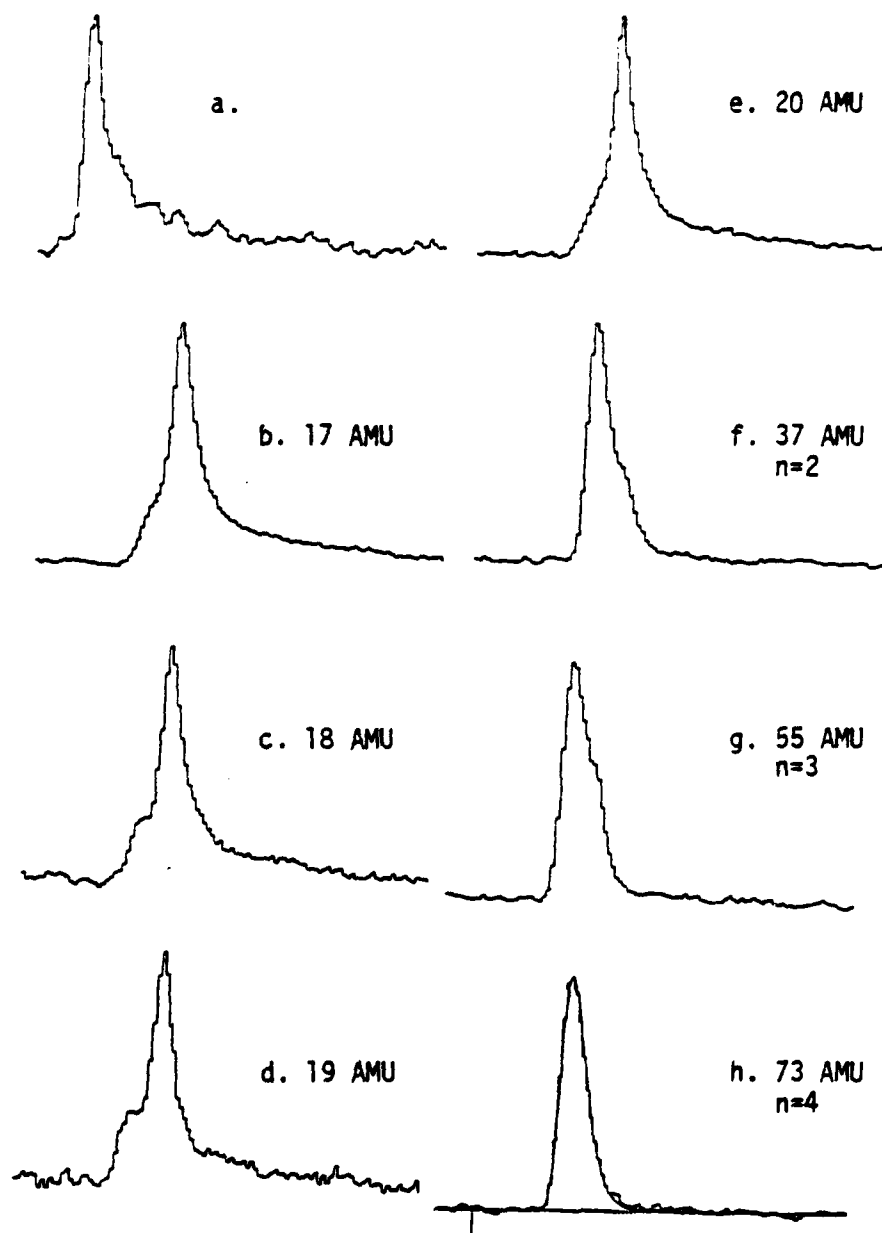


FIGURE 15. MASS-FILTERED TIME-OF-FLIGHT SPECTRA OF A CLUSTERED BEAM

$H_2O$  beam,  $P_0=1.1$  MPa,  $T_0=458^\circ$  K, periods: (a) .98 ms, (b-t) 1.75 ms, (u-ff) 1.46 ms\*, flight paths: (a) 20.6 cm, (b-ff) 70.6 cm\*. (a) no mass filtering, (b-ff) mass filter set as indicated (cluster order also indicated). (h-ff) translating Maxwellian shown fitted to data using indicated time origin (obtained with an assumed delay of 157  $\mu$ s). (a-t) data of 25-Jan-80, (u-ff) data of 31-Jan-80. (ff) uses a half-integer mass peak (see Figure 12).

\*See footnote for Figure 8.

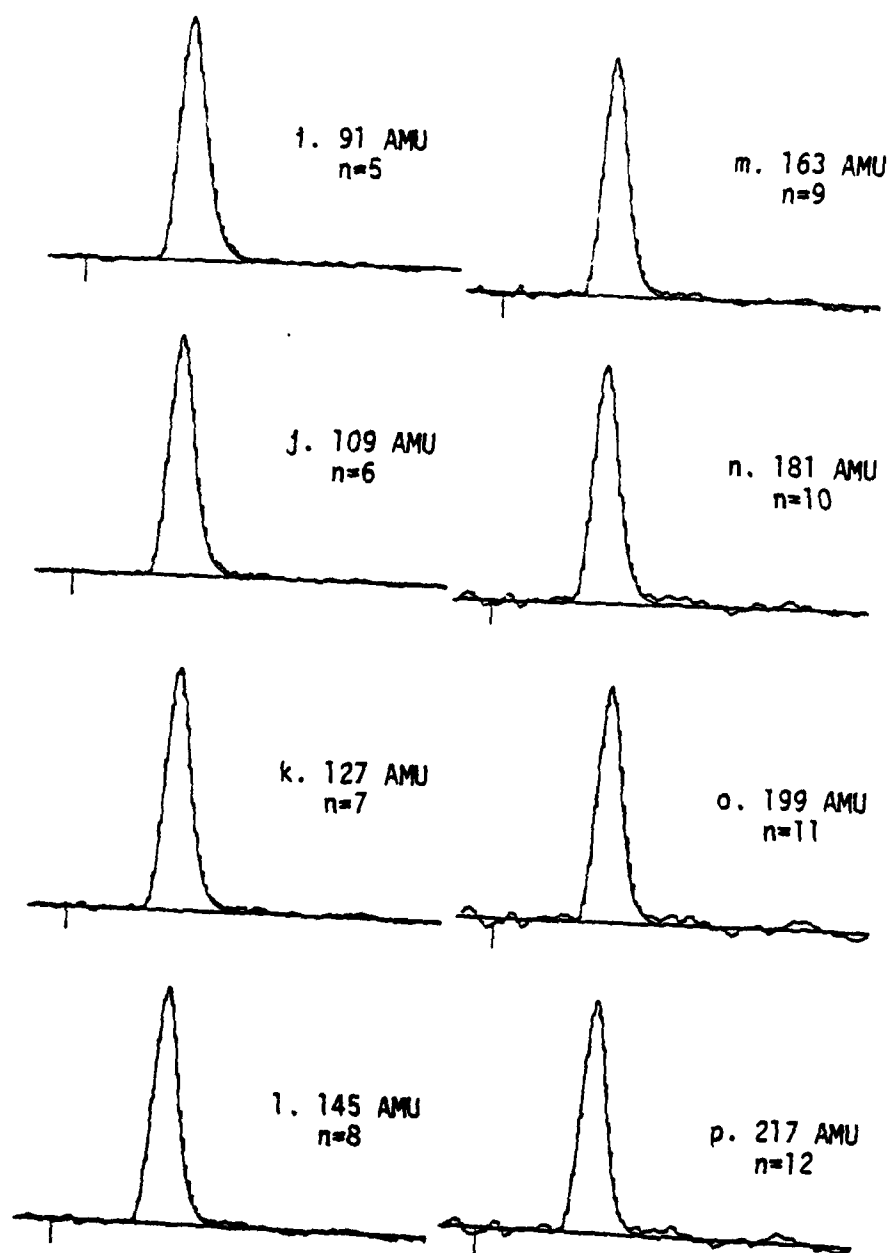


FIGURE 15 (continued).

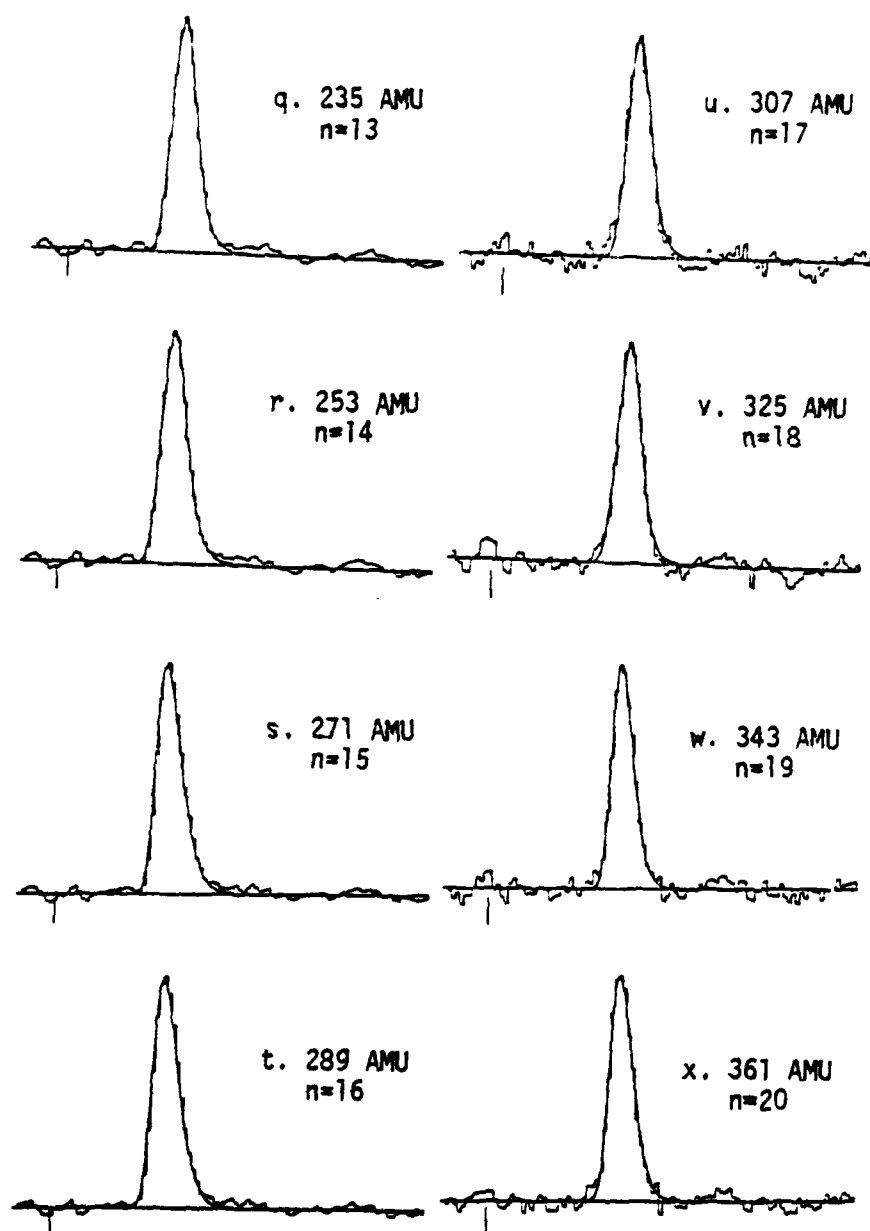


FIGURE 15 (continued).

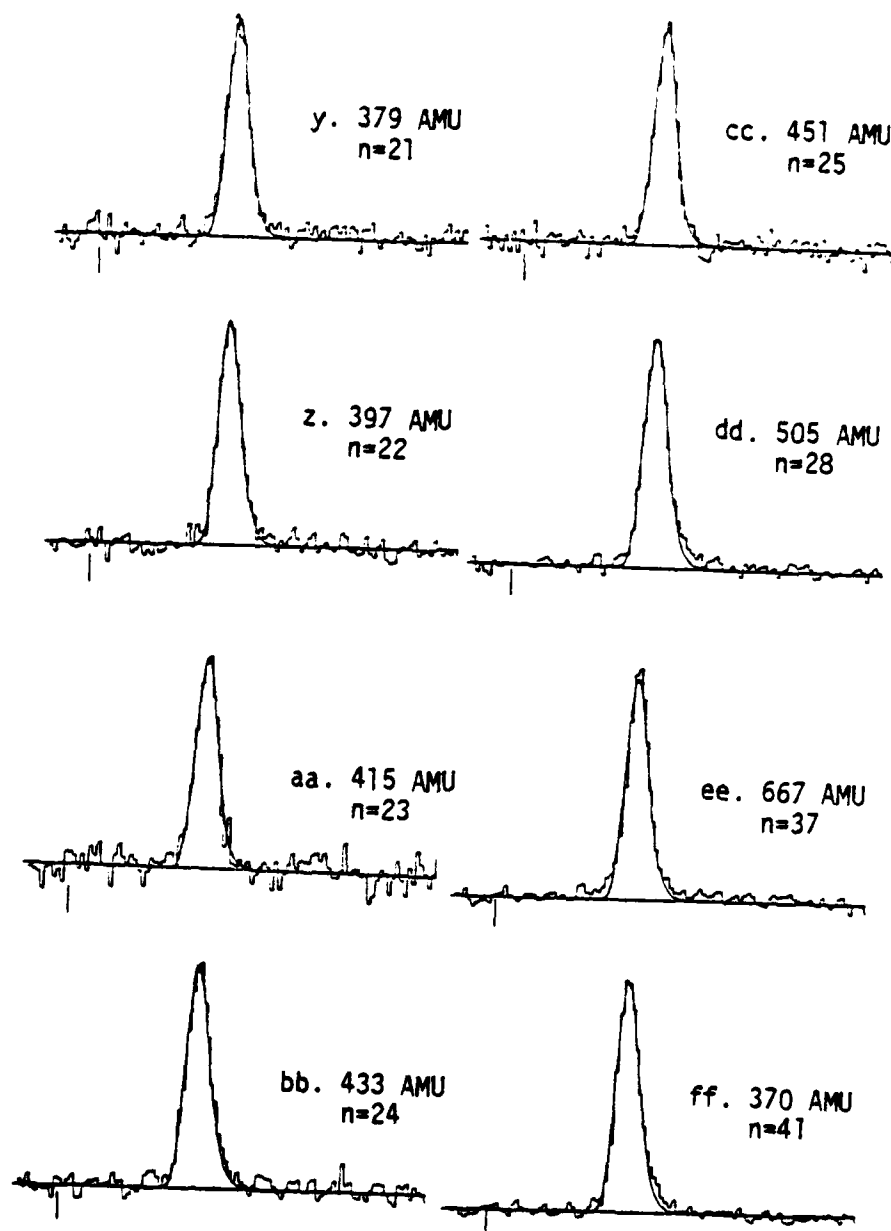


FIGURE 15 (concluded).

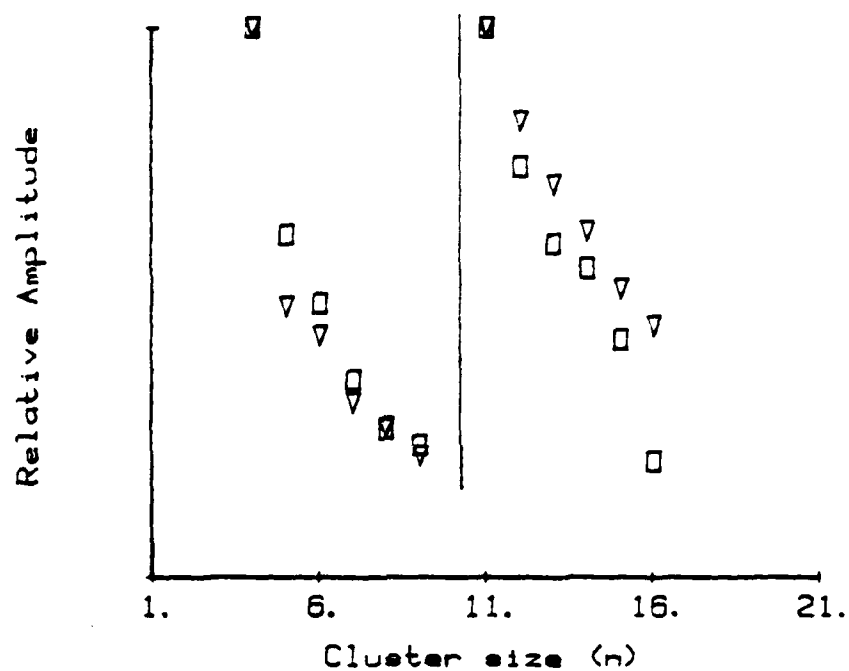


FIGURE 16. PEAK AMPLITUDE VERSUS CLUSTER SIZE FROM MASS-FILTERED TIME-OF-FLIGHT SPECTRA OF BEAM

Taken from data of Figure 15. Two short ranges shown here. Squares are peak amplitudes, triangles are amplitudes from mass spectra (Figure 12). Amplitudes are scaled so that the two amplitudes match at  $n=4$  and  $n=11$ .



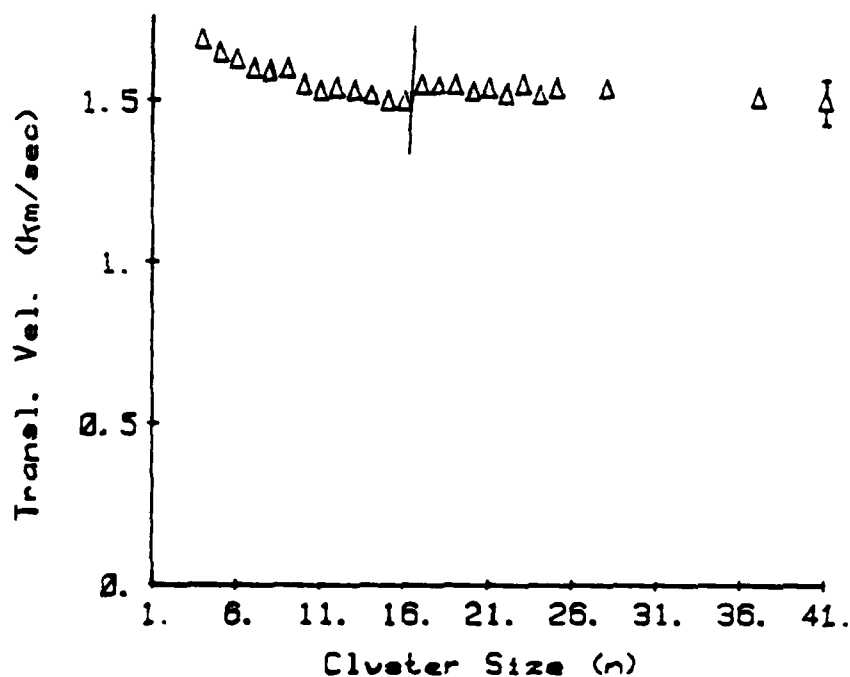


FIGURE 17. TRANSLATIONAL VELOCITY VERSUS CLUSTER SIZE FROM MASS-FILTERED TIME-OF-FLIGHT SPECTRA OF BEAM

Line after  $n=16$  divides data from separate days. Data obtained from fitted curves in Figure 15. Plotted is  $u$  from  $v^2 e^{-m(v-u)^2/2kT}$ . \*

Note that there are no points for  $n=1-3$  since it was not possible to fit a translating Maxwellian to the time-of-flight spectrum for these cluster sizes (see Figure 15).

\* Actually, since the data are time-of-flight, the fitted curve is a time distribution function determined as follows:

$$f(v)dv = f\left(\frac{L}{t}\right) \frac{L}{t^2} dt \propto \left(\frac{L}{t}\right)^4 e^{-m([L/t]-u)^2/2kT} dt$$

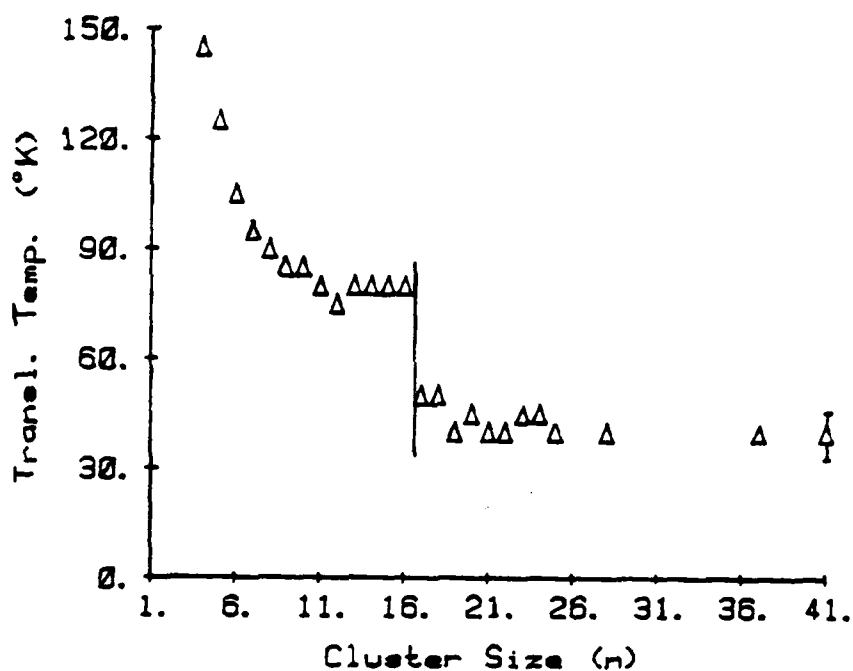


FIGURE 18. TRANSLATIONAL TEMPERATURE VERSUS CLUSTER SIZE FROM MASS-FILTERED TIME-OF-FLIGHT SPECTRA OF BEAM

Line after  $n=16$  divides data from separate days. Data obtained from fitted curves in Figure 15. Plotted is  $T$  from  $v^2 e^{-m(v-u)^2/2kT}$ , where  $m$  was taken as the monomer mass throughout. Note that there are no points for  $n=1-3$  since it was not possible to fit a translating Maxwellian to the time-of-flight spectrum for these cluster sizes (see Figure 15).

\* See footnote for Figure 17.

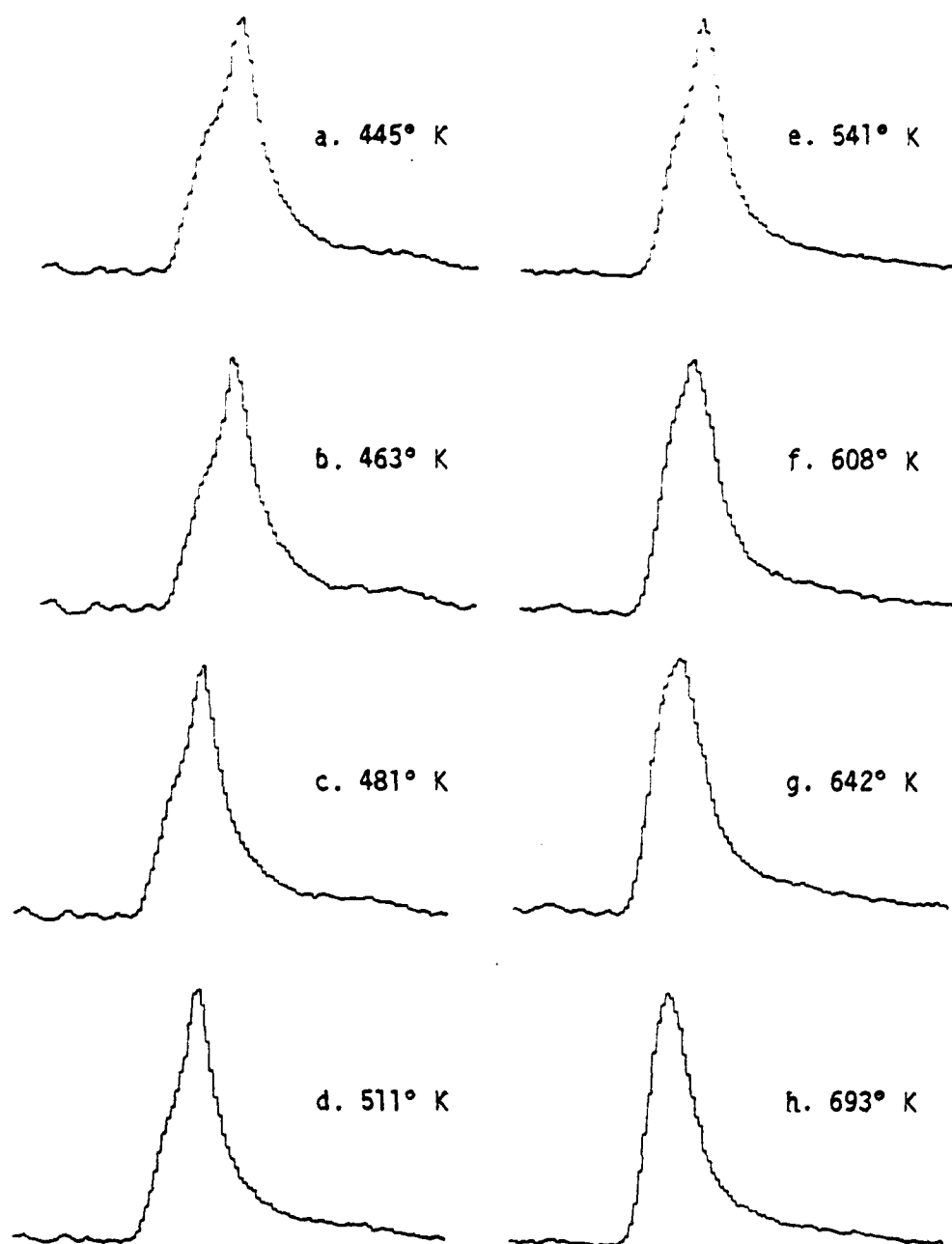


FIGURE 19. MASS 18 TIME-OF-FLIGHT SPECTRA OF BEAM VERSUS SOURCE TEMPERATURE ( $T_0$ )

$H_2O$  beam, (a-g)  $P_0=680$  kPa, (h)  $P_0=330$  kPa,  $T_0$  as marked, flight path 70.6 cm\*, period 1.45 ms\*. Note gradual disappearance of slower peak. The mass spectrum for example (h) still showed clusters to  $n=20$ .

\*See footnote for Figure 8.

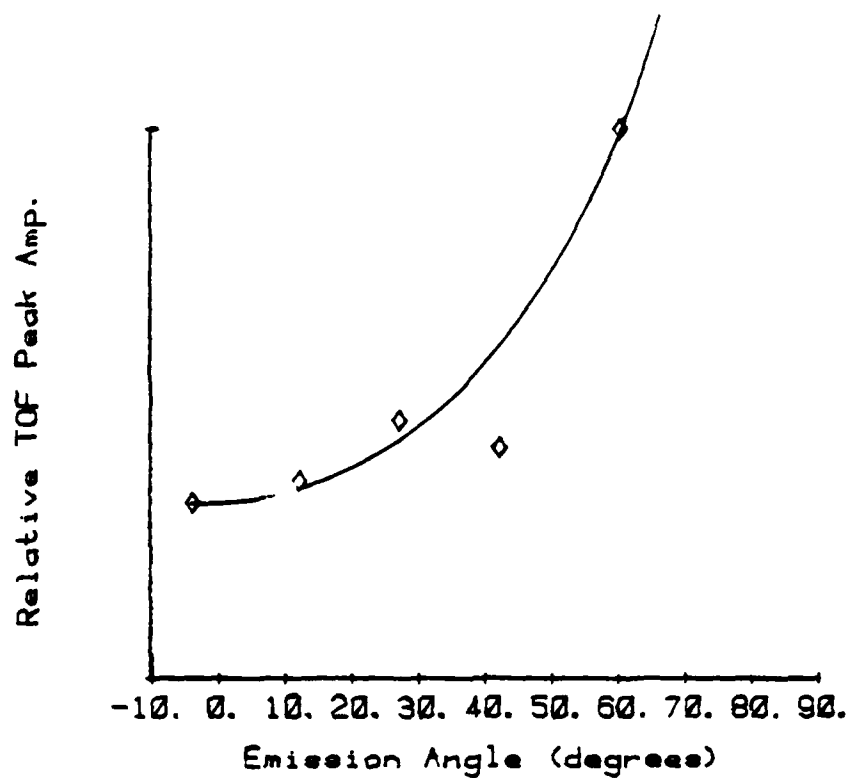


FIGURE 20. PEAK AMPLITUDE VERSUS EMISSION ANGLE FOR EVAPORATION FROM COVELLITE

No beam, CuS (1000) target. Frost-like ice layer grown from beam at  $T_s = 180^\circ \text{ K}$ . Data shown for  $T_s = 204^\circ \text{ K}$ .

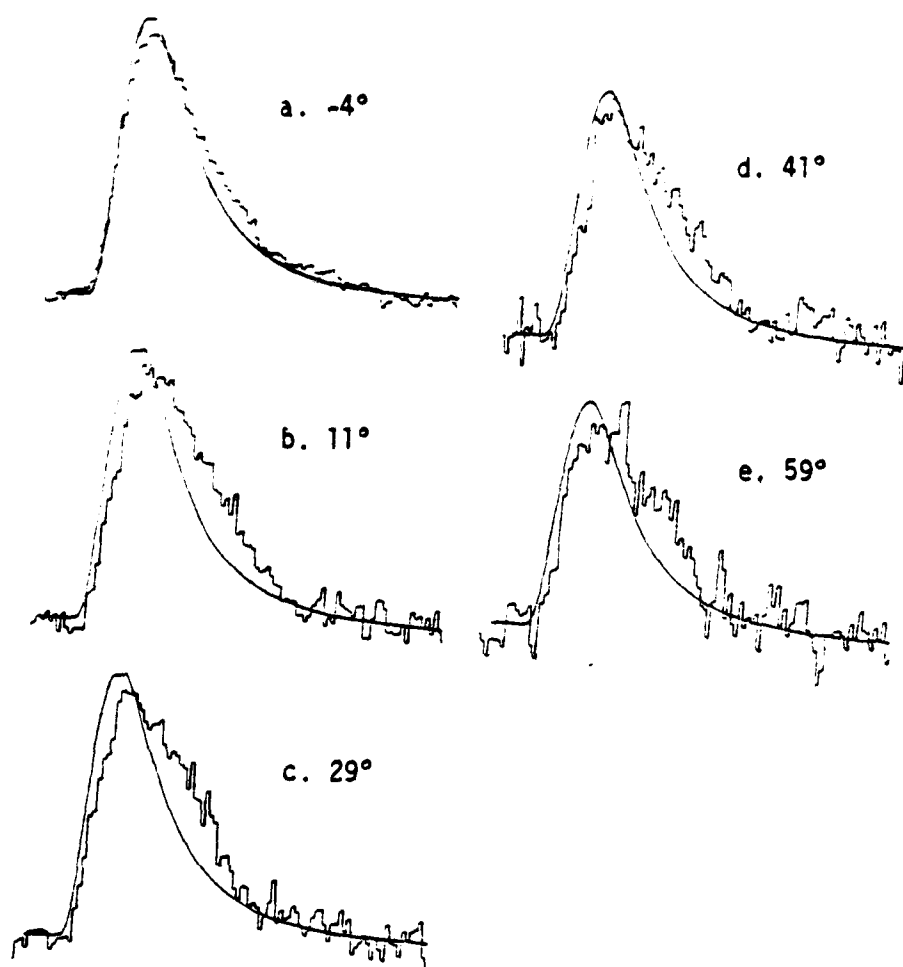


FIGURE 21. TIME-OF-FLIGHT SPECTRA VERSUS EMISSION ANGLE FOR EVAPORATION FROM COVELLITE

Same conditions as for Figure 20. Flight path 20.6 cm\*, period 1.61 ms\*. Fitted curves are static Maxwellians at 204° K. Emission angles are indicated.

\*See footnote for Figure 8.

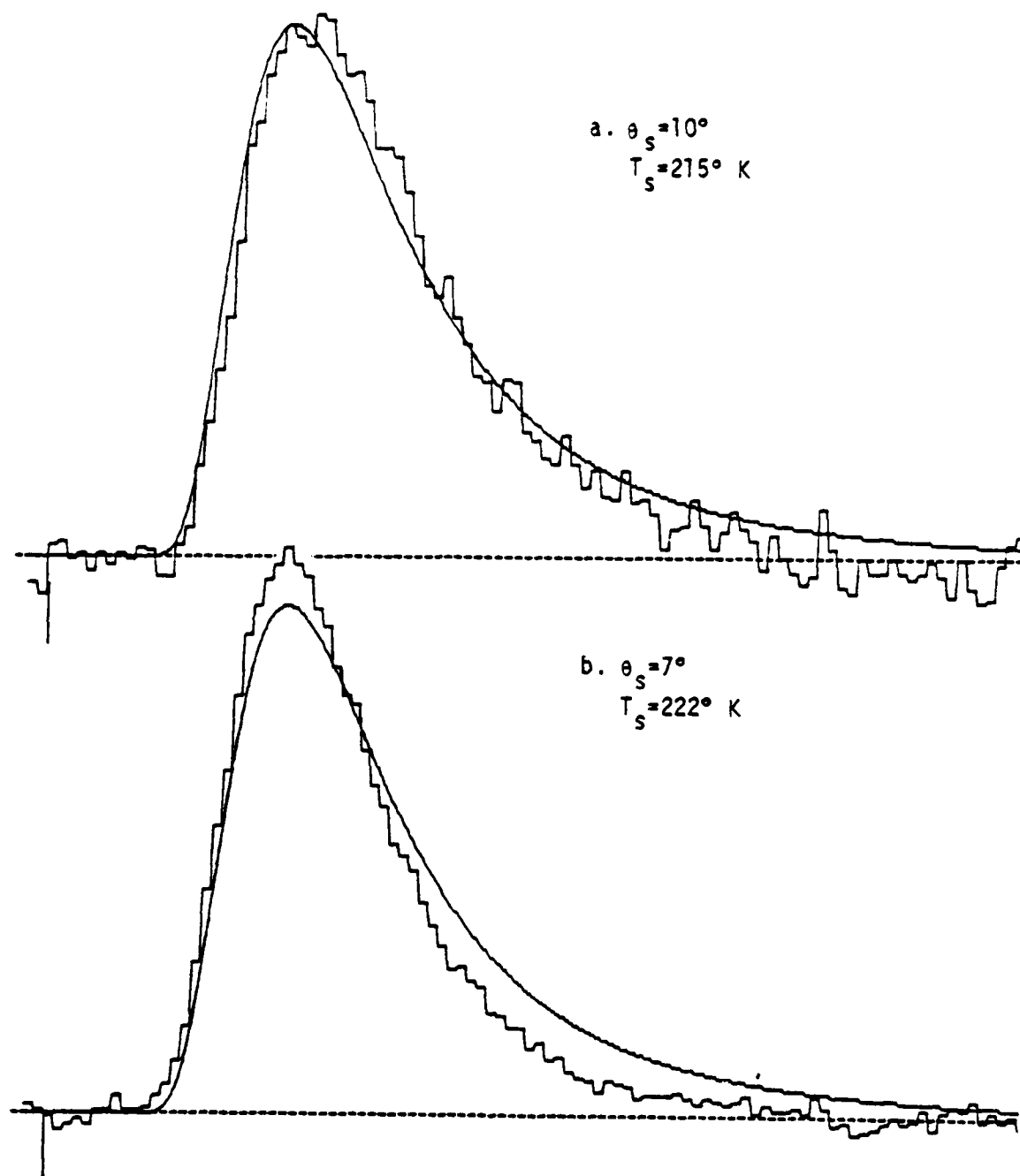


FIGURE 22. TIME-OF-FLIGHT SPECTRA FOR EVAPORATION FROM SINGLE CRYSTAL ICE

$T_s$  and  $\theta_s$  as marked. Mass-filtered spectra, mass filter set at 18 AMU. Flight path 41.9 cm\*, period 2.96 ms\*. Fitted curves are static Maxwellians at  $T_s$  using a delay of 90  $\mu$ s.

\*See footnote for Figure 8.

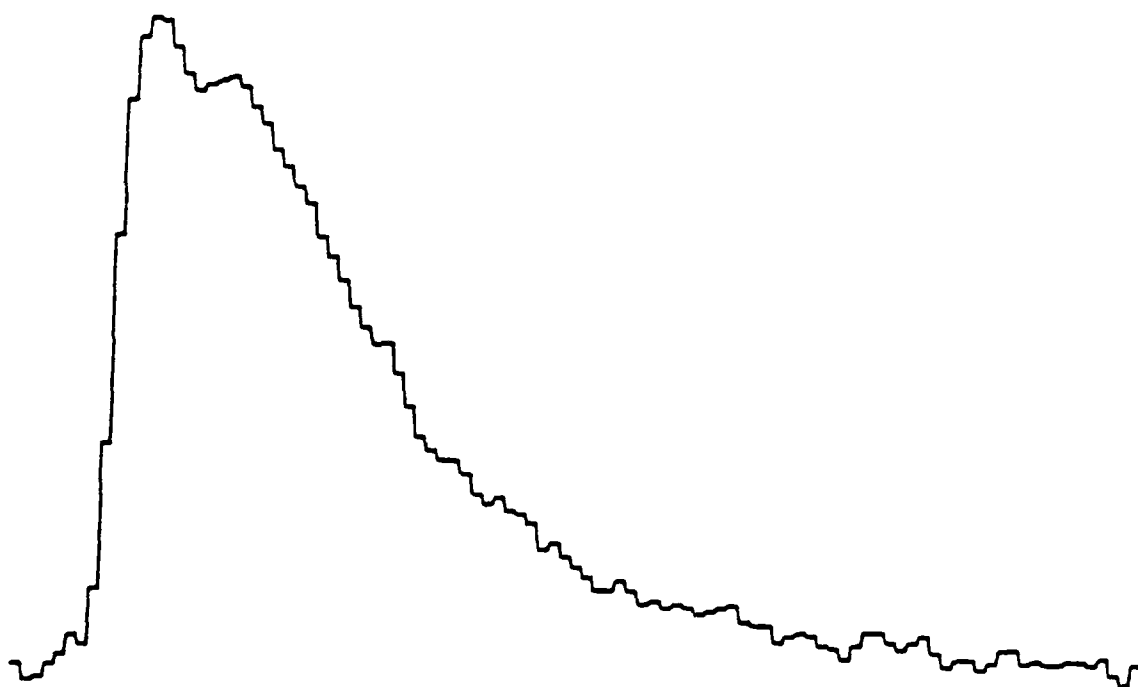


FIGURE 23. SAMPLE TIME-OF-FLIGHT SPECTRUM WITH RESOLVED FAST PEAK  
AND MAXWELLIAN PEAK.

H<sub>2</sub>O beam,  $T_0=457^\circ$  K,  $P_0=650$  kPa scattering from Pt  $241^\circ$  K,  $\theta_i=\theta_s=65^\circ$ ,  
flight path 20.6 cm\*, period 1.47 ms\*.

\*See footnote for Figure 8.

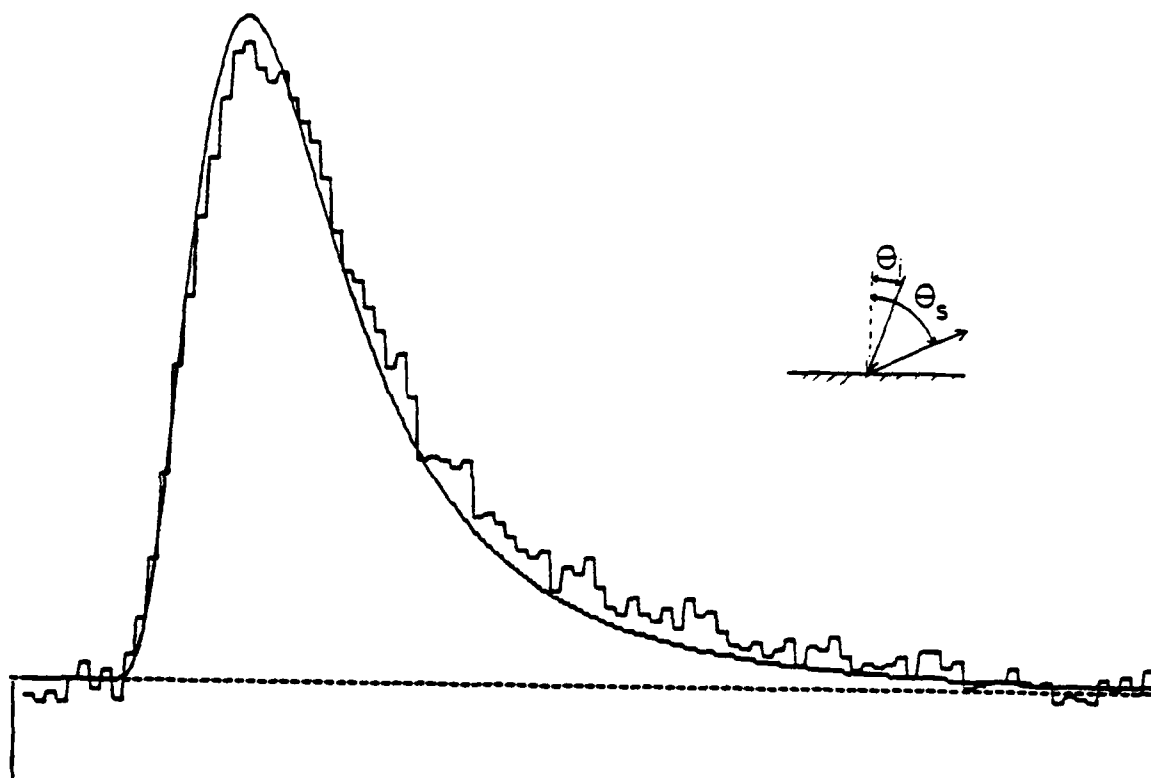


FIGURE 24. TIME-OF-FLIGHT SPECTRUM FOR BACKSCATTERING AND AMPLITUDE VERSUS SCATTERING ANGLE

a.  $\text{H}_2\text{O}$  beam,  $T_0=457^\circ \text{ K}$ ,  $P_0=880 \text{ kPa}$ , scattering from Si at  $223^\circ \text{ K}$ , flight path  $20.6 \text{ cm}^*$ , period  $1.78 \text{ ms}^*$ ,  $\theta_i=-20^\circ$ ,  $\theta_s=65^\circ$ . Fitted curve is a Maxwellian for water at  $223^\circ \text{ K}$ . Amplitude plot on next page.

\*See footnote for Figure 8.



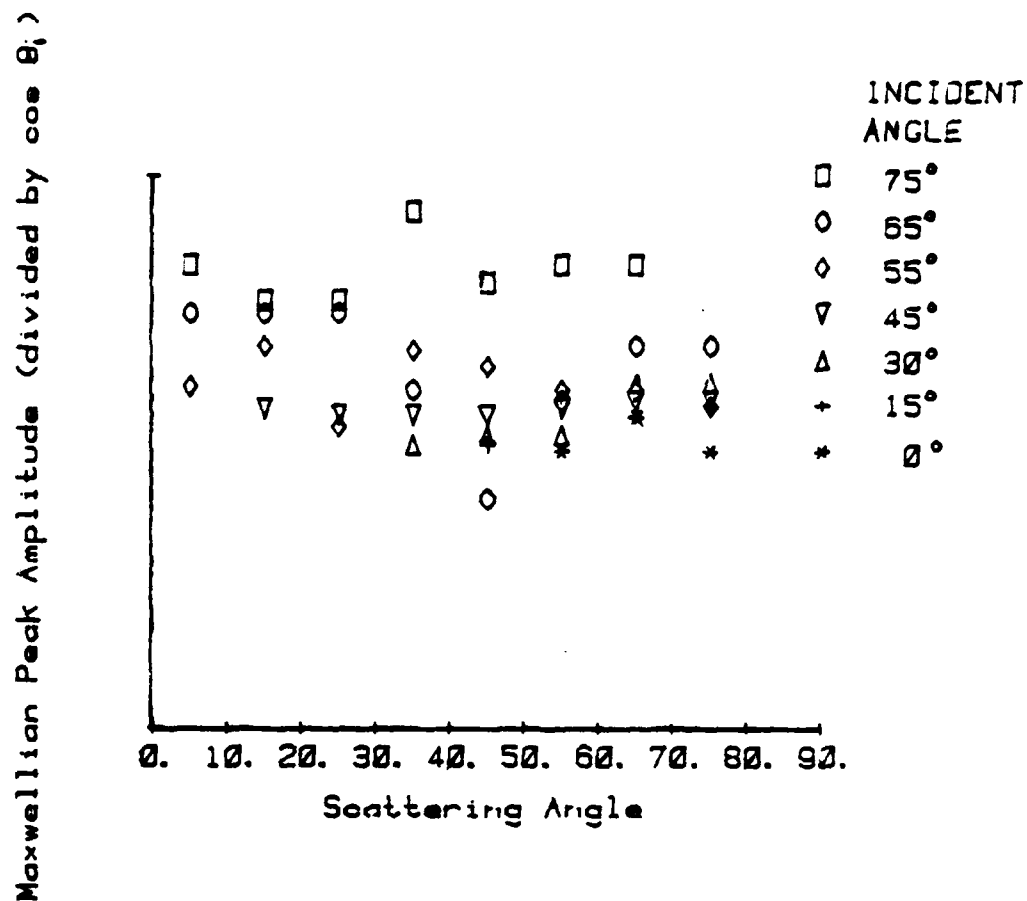


FIGURE 24. (concluded)

b. Amplitude of Maxwellian component of scattered stream.  $H_2O$  beam,  $T_0=455^\circ K$ ,  $P_0=560$  kPa, scattering from Si at  $223^\circ K$ . For the collimation geometry of the system, a cosine distribution gives a constant amplitude. The apparent variation with  $\theta_i$  is a consequence of a drift in the gain of the electron multiplier for which corrections have not been made.

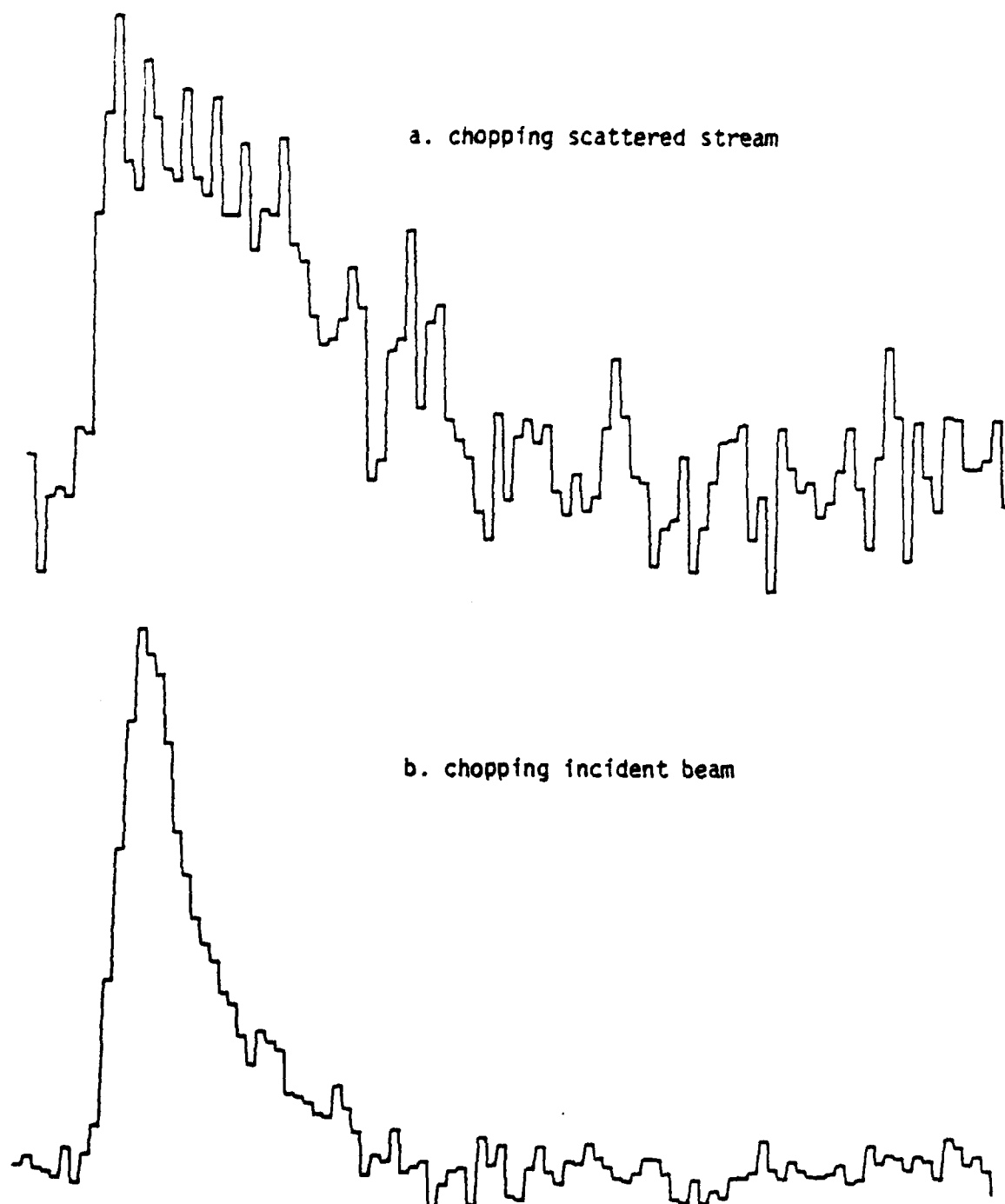


FIGURE 25. COMPARISON OF TIME-OF-FLIGHT SPECTRA CHOPPING INCIDENT BEAM VERSUS CHOPPING SCATTERED STREAM WHEN MOST OF BEAM STICKS TO TARGET

$H_2O$  beam  $P_0=880$ ,  $T_0=556^\circ$  K scattering from Si at  $212^\circ$  K,  $\theta_i=65^\circ$ ,  $\theta_s=75^\circ$ , flight path 20.6 cm\* (for chopping scattered stream), period 1.76 msec\*. Chopping position as marked.

\*See footnote for Figure 8.

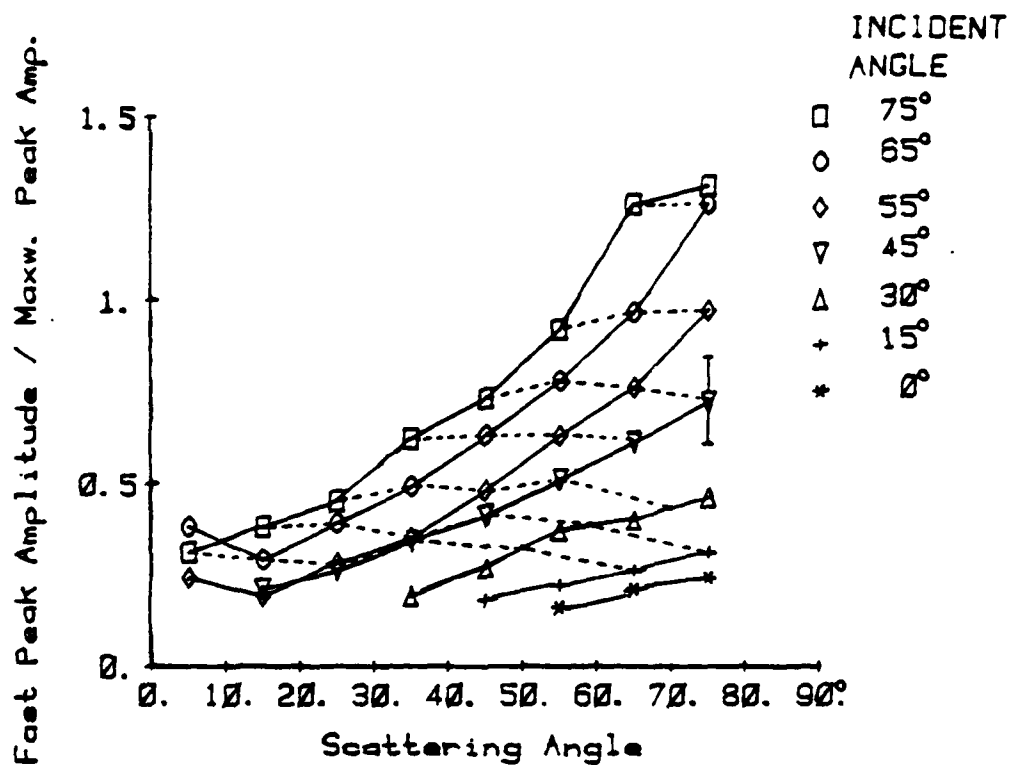


FIGURE 26. FAST PEAK AMPLITUDES

Source conditions:  $T_0=455^\circ \text{ K}$ ,  $P_0=560 \text{ kPa}$ ; Target:  $\text{Si}(111)$ ,  $T_s=223^\circ \text{ K}$ . Dashed lines connect points of constant "turning angle" ( $\theta_i + \theta_s = \text{constant}$ ). The amplitudes are normalized by dividing by the associated Maxwellian peak amplitude. This eliminates any drift effects and automatically corrects for the flux variation with incident angle.

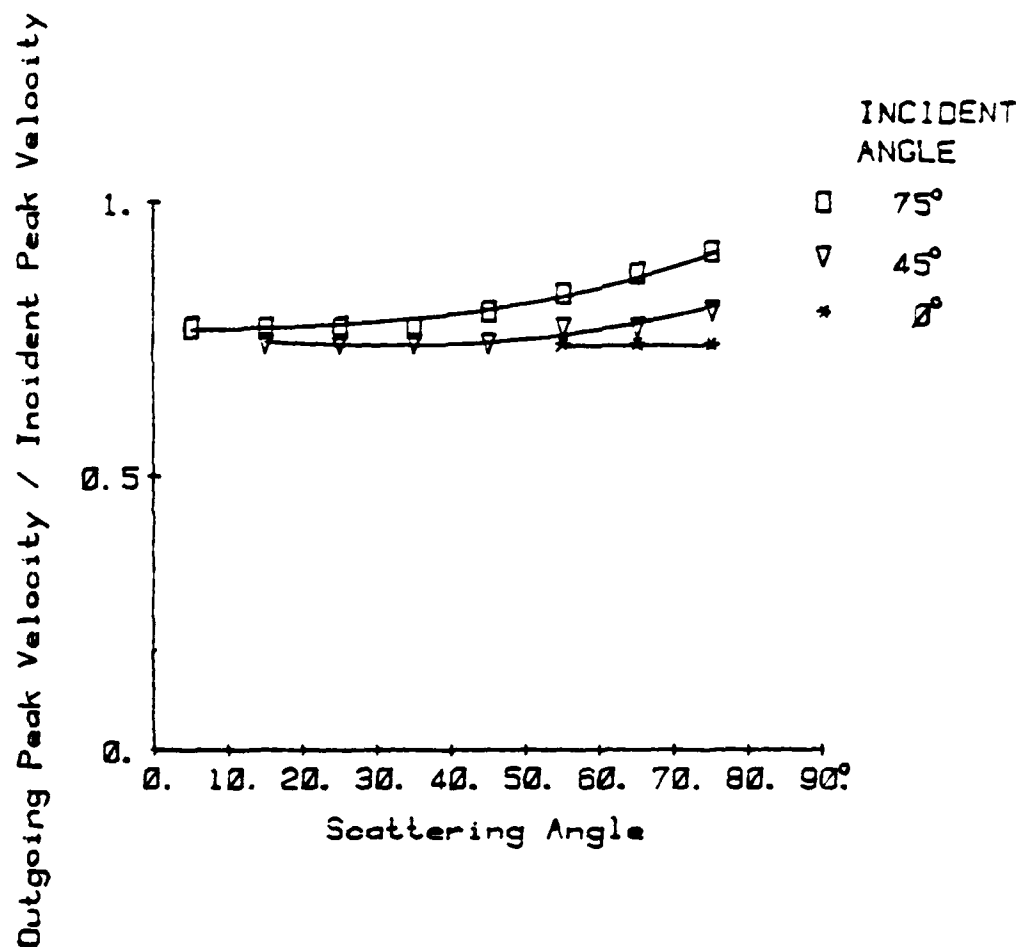


FIGURE 27. VELOCITIES AT MAXIMUM AMPLITUDES FOR THE FAST PEAK

Same conditions as for Figure 26. Data for only a few incident angles are shown for clarity. Note that the peak velocity is also constant for constant "turning angle" (see Figure 26).

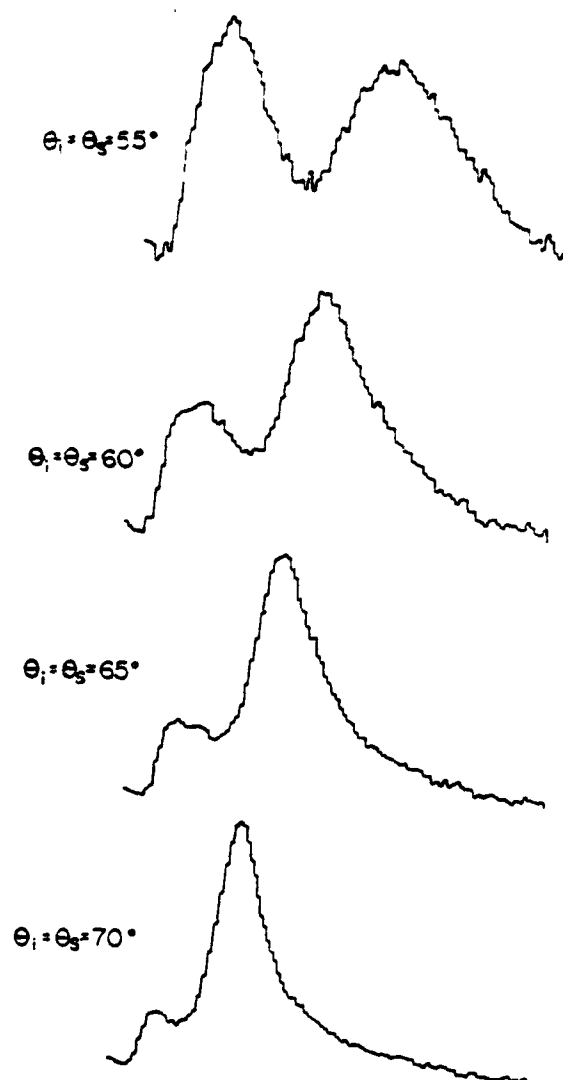


FIGURE 28. EXAMPLES OF TIME-OF-FLIGHT SPECTRA FOR THE SPECULARLY DIRECTED SLOW PEAK

H<sub>2</sub>O beam  $P_0=570$  kPa,  $T_0=456^\circ$  K scattering from Si at  $241^\circ$  K. Flight path  $20.6$  cm\*, period  $1.58$  ms\*. There are three peaks present in each spectrum: a fast peak and a Maxwellian peak (unresolved) and a slow peak. Note the large intensity of the slow peak and its variations with angle. All four spectra are scaled to the same height. The actual changes in the amplitudes of the slow peak with  $\theta_i$  can be realized by noting that the peaks on the left (Maxwellian and fast peaks) have nearly consistent amplitudes with changing  $\theta$ .

\*See Figure 8.

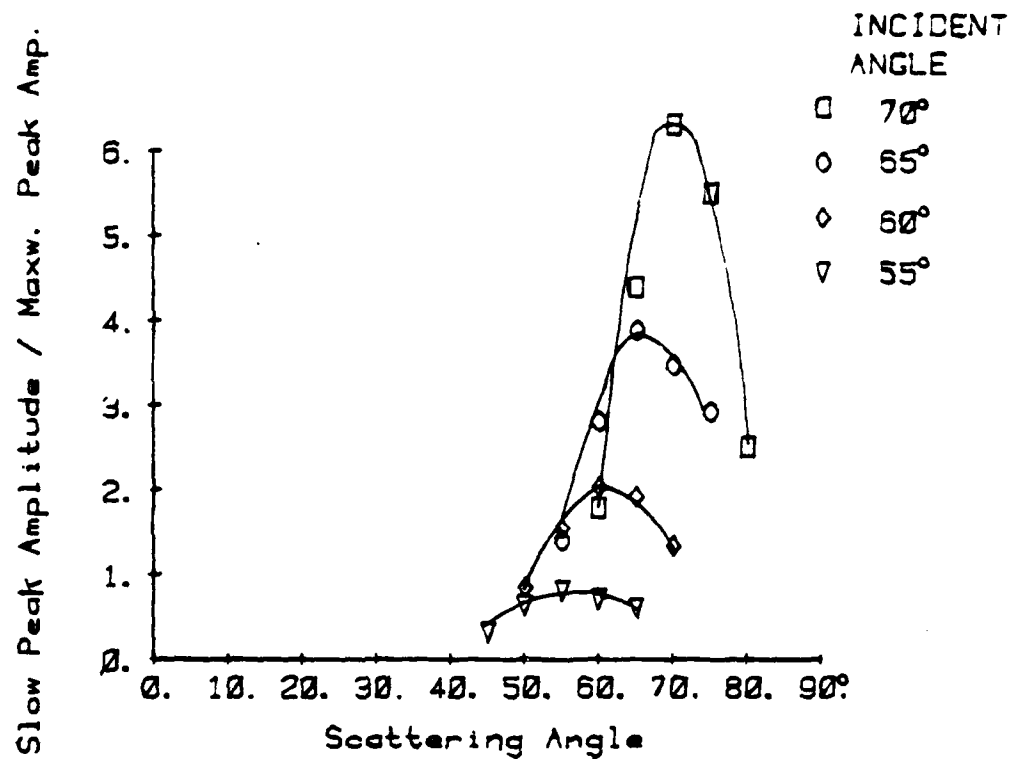


FIGURE 29. AMPLITUDES OF THE SPECULARLY DIRECTED SLOW PEAK

Same conditions as for data in Figure 28. Amplitudes are normalized by dividing by the Maxwellian peak amplitude as in Figure 26. Note specular reemission angles.

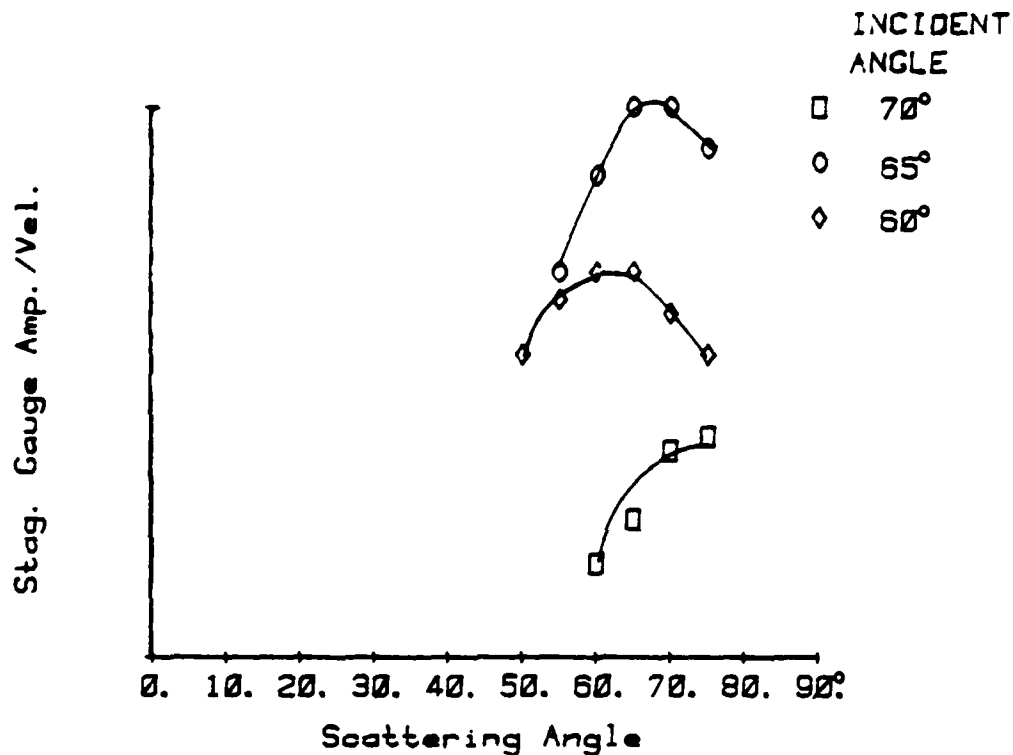


FIGURE 30. STAGNATION GAUGE AMPLITUDES FOR SPECULARLY DIRECTED SLOW PEAK

H<sub>2</sub>O beam  $P_0=500$  kPa,  $T_0=455^\circ$  K scattering from S<sub>1</sub> at  $241^\circ$  K. Stagnation gauge located at usual time-of-flight ionizer position with the same collimation. Since the stagnation gauge measures flux, amplitudes are divided by the average velocity obtained from time-of-flight data to give a density which can be compared to the time-of-flight peak amplitude data of Figure 29.

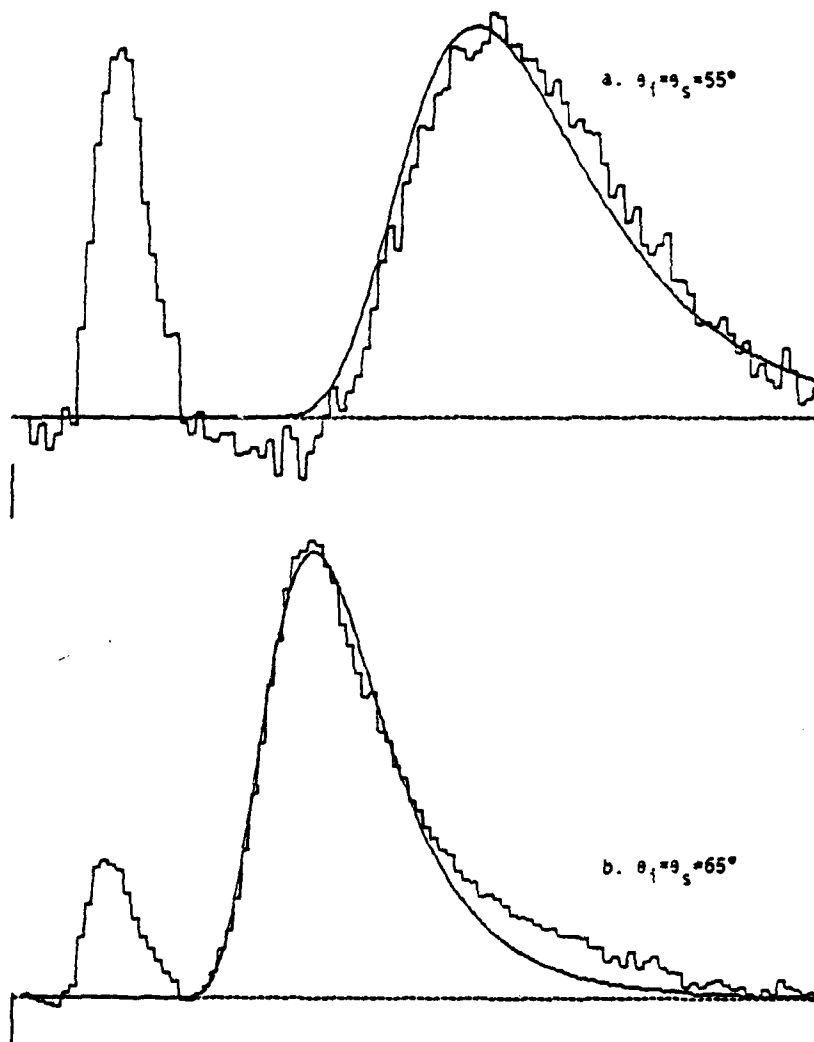


FIGURE 31. FITTING OF TRANSLATING MAXWELLIAN TO SPECULARLY DIRECTED SLOW PEAK

$H_2O$  beam  $P_0 = 560$  kPa,  $T_0 = 455^\circ$  K scattering from Si at  $241^\circ$  K, flight path  $20.6$  cm\*, period  $1.58$  ms\*. Angles as marked. Maxwellian component subtracted out. Fitted with translating Maxwellians, monomer mass, Mach number 2.2, temperatures (a)  $6^\circ$  K, (b)  $15^\circ$  K. Note that a Mach number of 2.2 also provides an approximate fit to the time-of-flight spectrum (without mass filtering) of the incident beam (Figure 11).

\*See Figure 8.



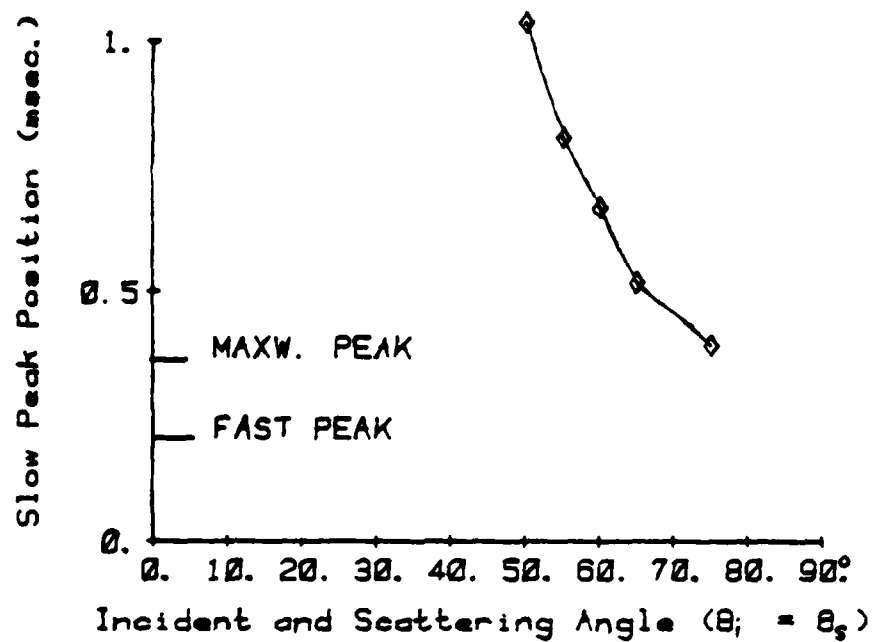


FIGURE 32. PEAK POSITIONS IN TIME-OF-FLIGHT SPACE FOR THE SPECULARLY DIRECTED SLOW PEAK

Same conditions as for data in Figures 28 and 29. The ordinate represents the shifts noted in Figure 28. The fast peak and Maxwellian peak positions are marked for comparison.

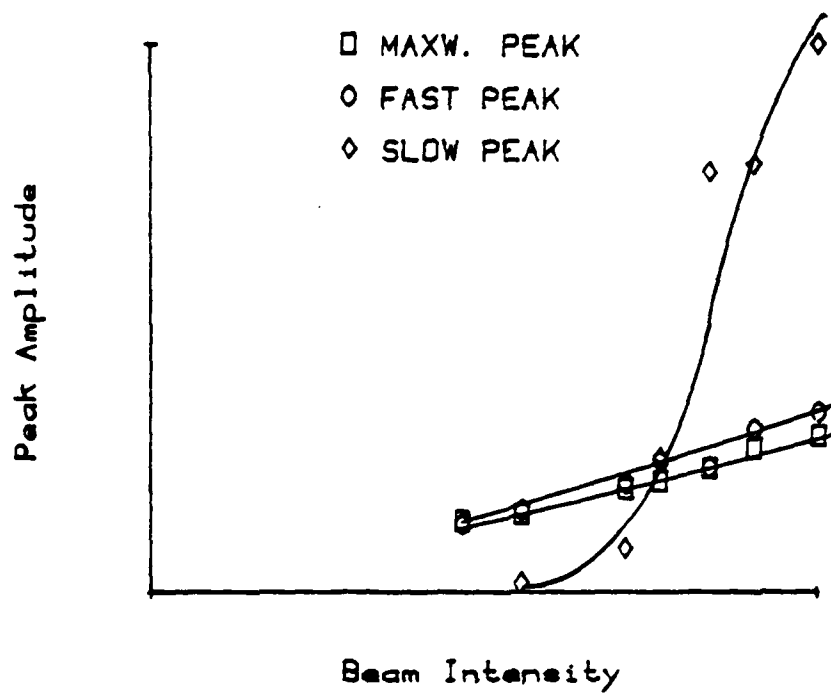


FIGURE 33. PEAK AMPLITUDES VERSUS BEAM INTENSITY

H<sub>2</sub>O beam  $P_0=250 \rightarrow 1120$  kPa,  $T_0=471^\circ$  K scattering from Si at  $239^\circ$  K.

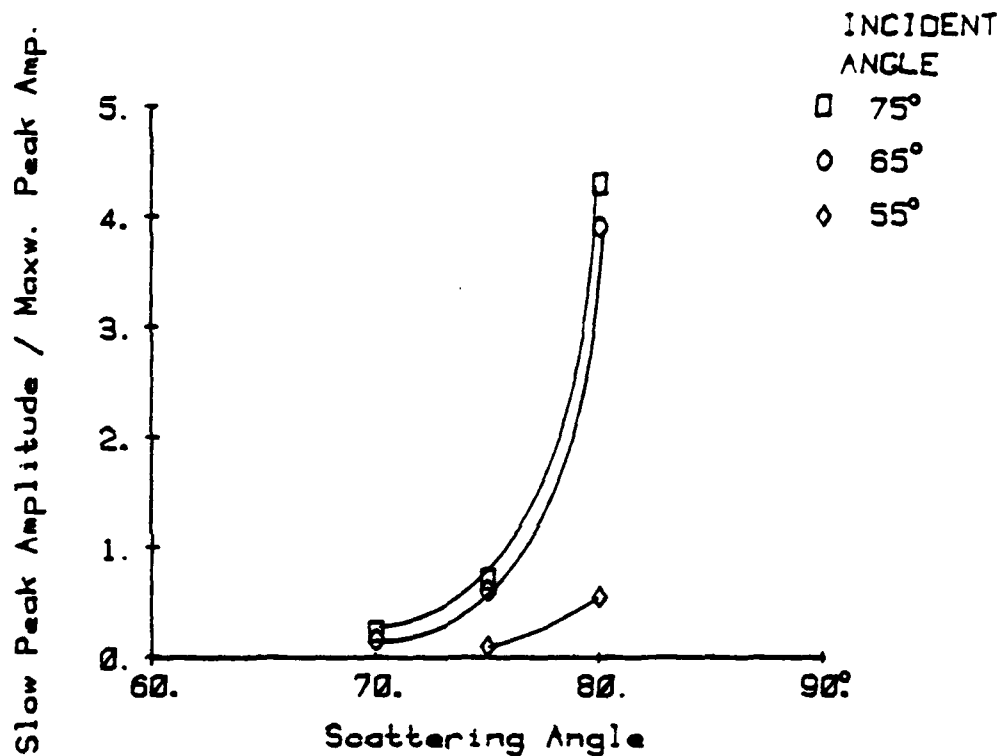


FIGURE 34. AMPLITUDES OF THE NON-SPECULAR SLOW PEAK

H<sub>2</sub>O beam  $P_0=960$  kPa,  $T_0=452^\circ$  K scattering from Pt at  $293^\circ$  K. Data for only a few incident angles are shown for clarity. Amplitudes are normalized by dividing by the Maxwellian peak amplitude as in Figures 26 and 29.

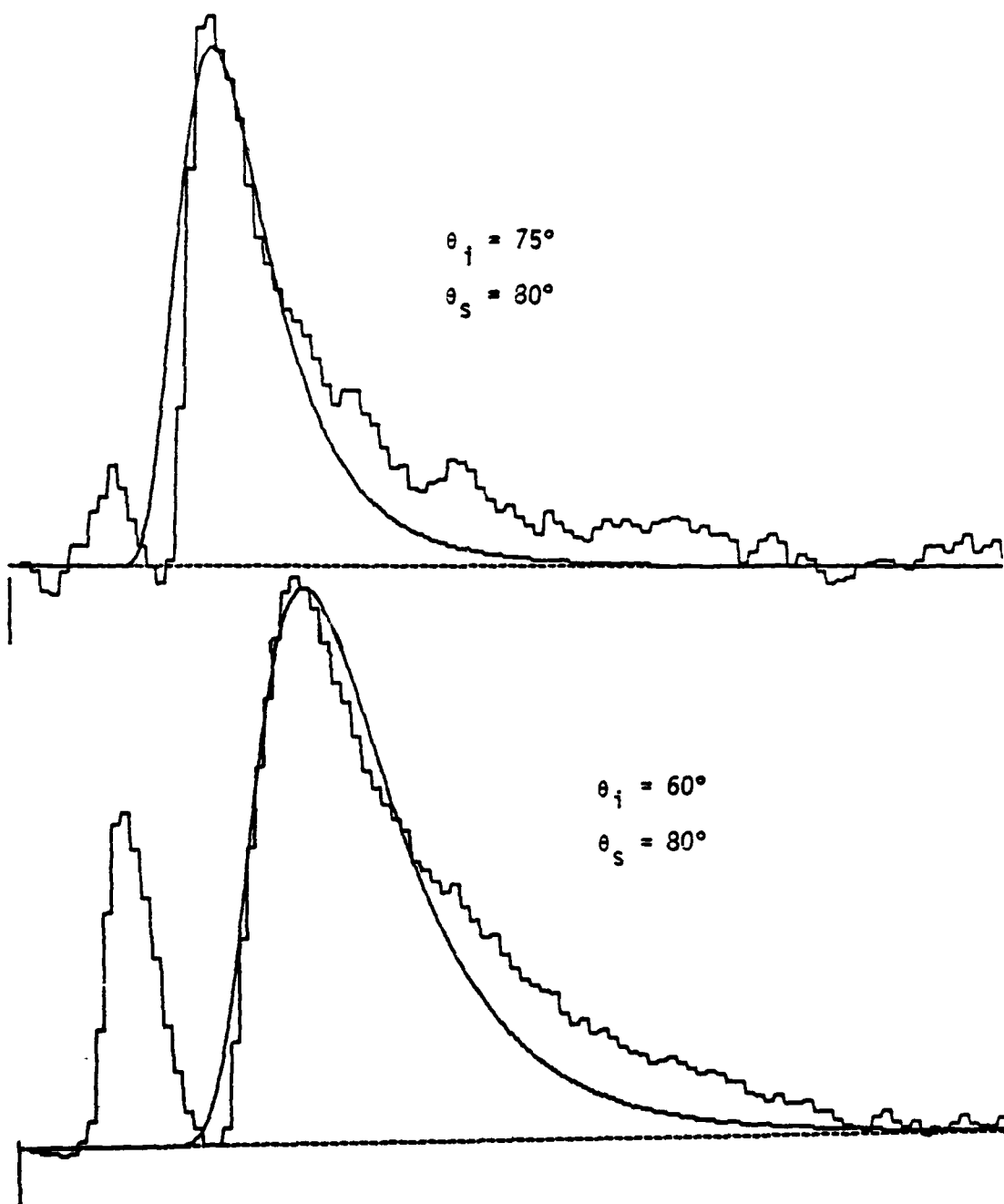


FIGURE 35. FITTING OF TRANSLATING MAXWELLIAN TO NON-SPECULAR SLOW PEAK

H<sub>2</sub>O beam,  $P_0=950$  kPa,  $T_0=452^\circ$  K, scattering from Pt at  $291^\circ$  K, flight path  $20.6$  cm\*, period  $1.58$  ms\*, angles as marked. Maxwellian component subtracted out. Fitted with translating Maxwellians, monomer mass, Mach number 1.6, temperatures (a)  $80^\circ$  K, (b)  $35^\circ$  K. Compare Figure 31.

\*See footnote for Figure 8.

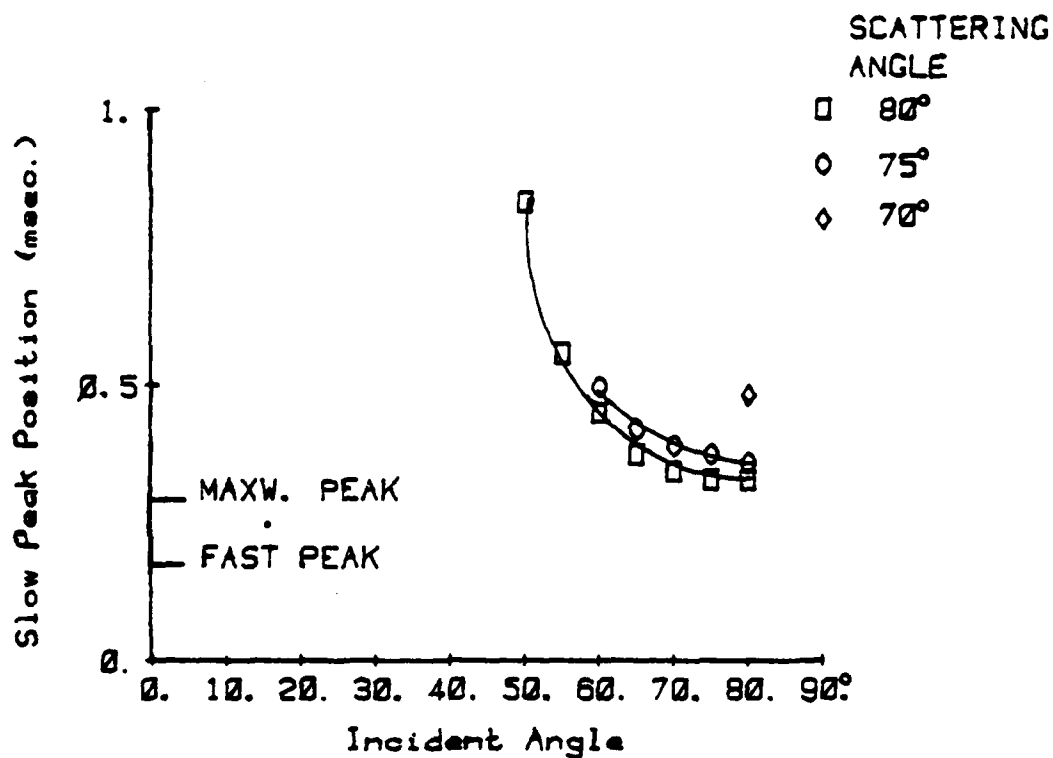


FIGURE 36. PEAK POSITIONS FOR THE NON-SPECULAR SLOW PEAK

Same conditions as for Figure 34. Plot is as a function of incident angle, since data can be obtained for only a few scattering angles. The fast peak and Maxwellian peak positions are marked for comparison.

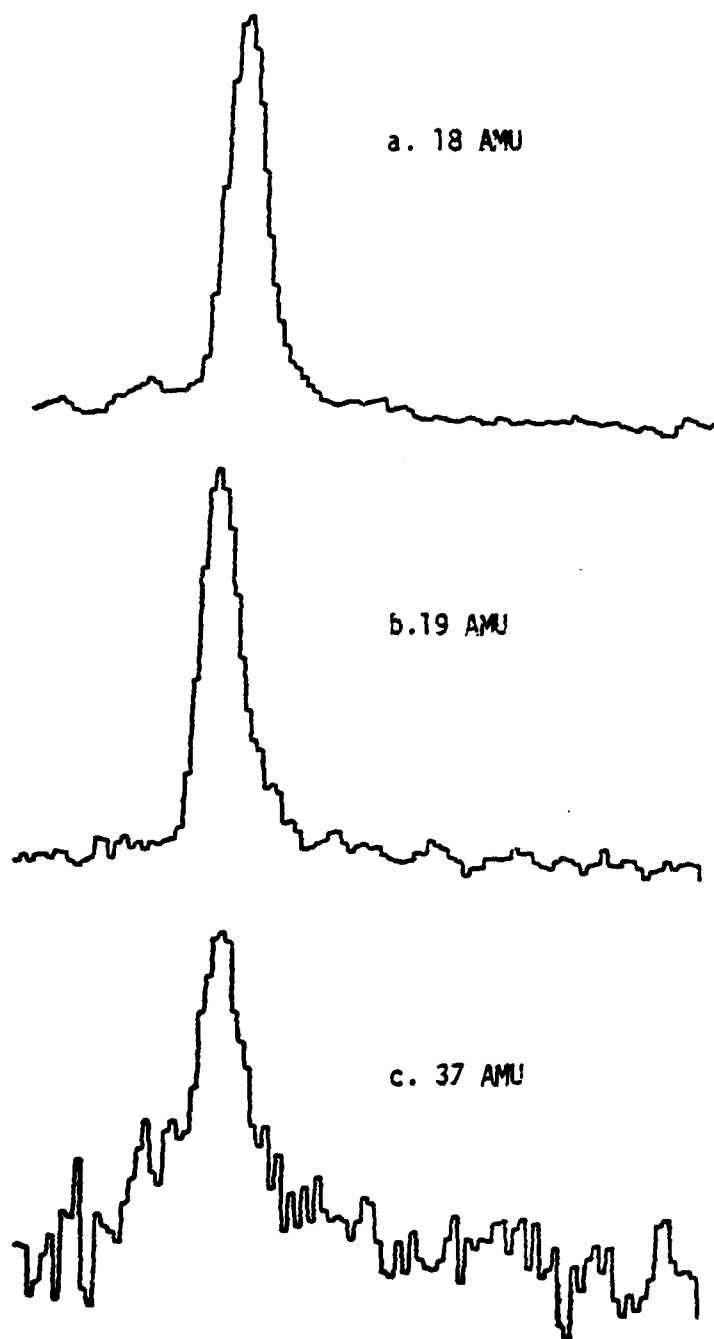


FIGURE 37. VELOCITY SPECTRA OF THE ONLY THREE WATER SPECIES FOUND IN SCATTERING FROM S1

H<sub>2</sub>O beam, T<sub>0</sub>=452° K, P<sub>0</sub>=1.0 MPa, scattering from S1 at 291° K. flight path 41.9 cm\*, period 2.99 ms\*,  $\theta_i=67^\circ$ ,  $\theta_s=79^\circ$ . No spectra could be generated for mass filter set higher than 37 AMU.

\*See footnote for Figure 8.

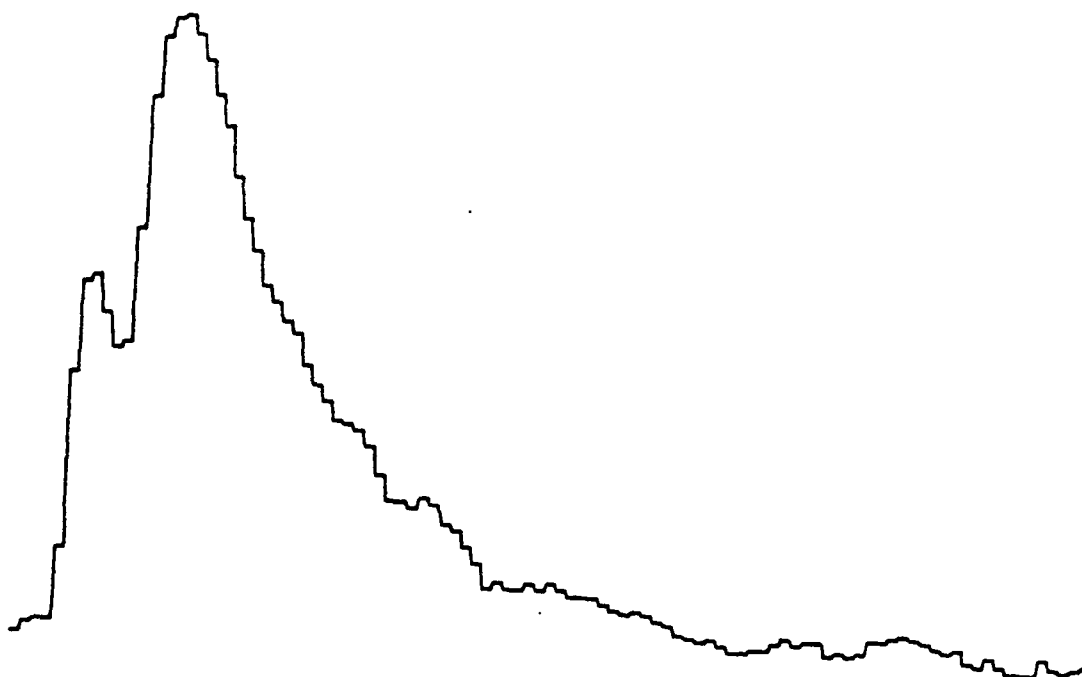


FIGURE 38. TIME-OF-FLIGHT SPECTRUM WITHOUT MASS FILTERING FOR  
CONDITIONS OF FIGURE 37

Flight path 20.6 cm\*, period 3.00 ms\*.

---

\*See footnote for Figure 8.

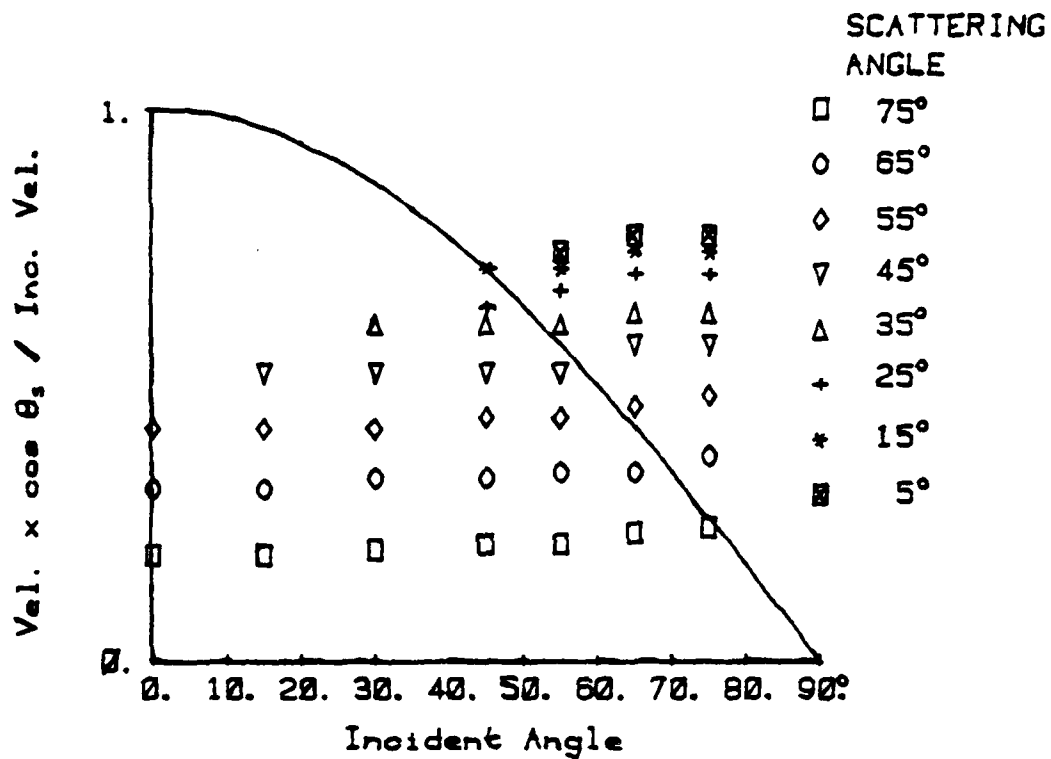


FIGURE 39. COMPONENTS OF FAST PEAK VELOCITY

Taken from data shown in Figures 26 and 27. Data are normalized by dividing by the incident velocity. For reference, the components of the incident velocity are shown as a smooth curve. Note that all points above this curve represent conditions where there has been a gain in that particular component. This page shows normal components; tangential components are on the next page.



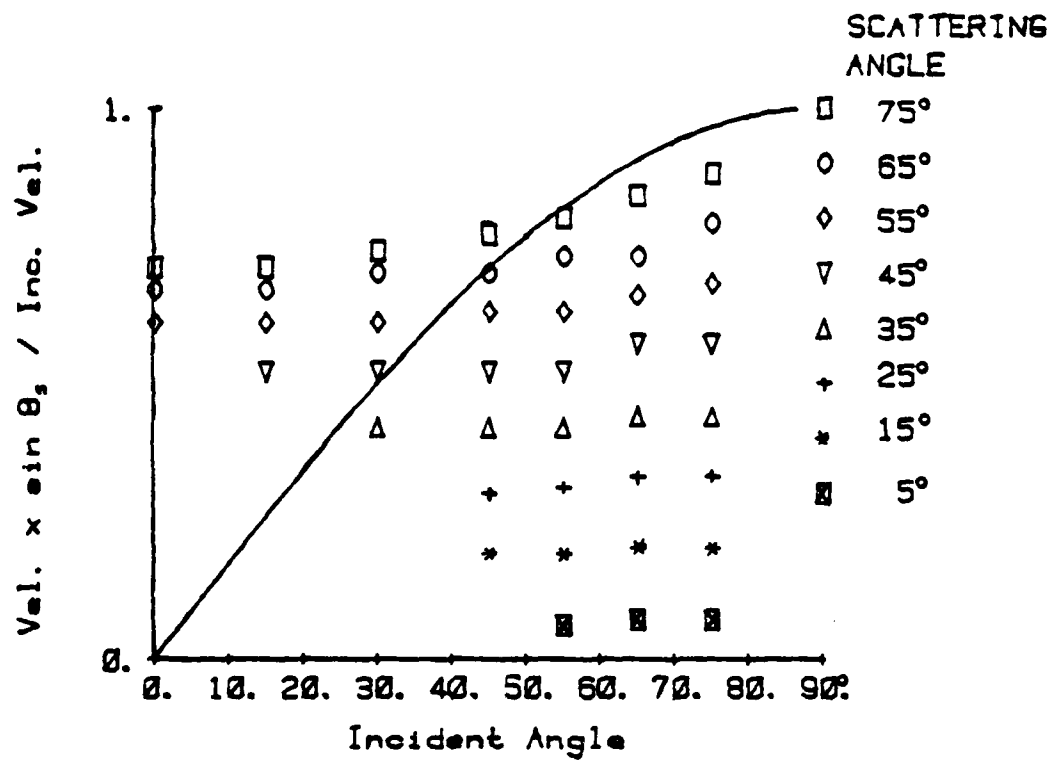


FIGURE 39 (concluded).

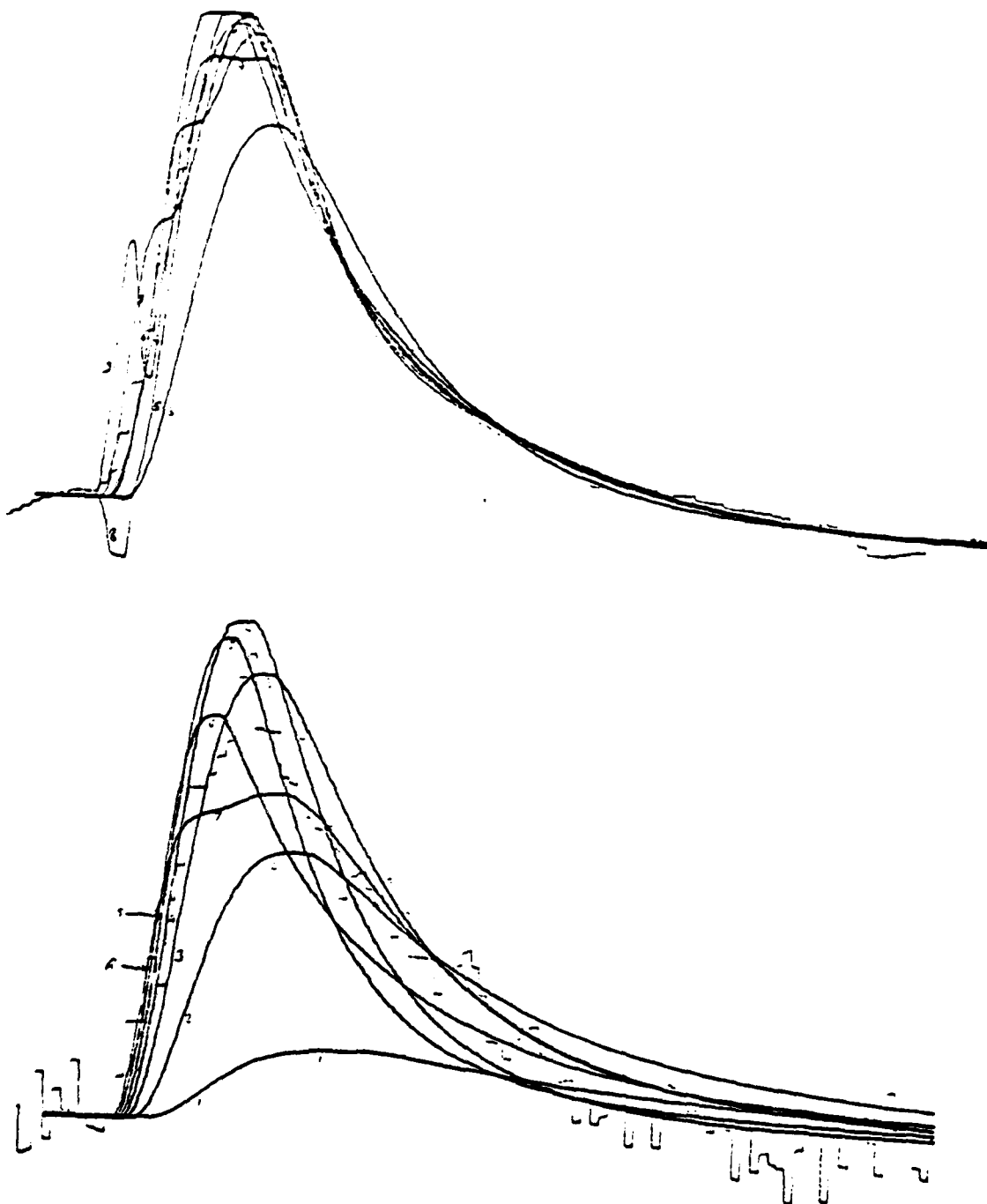


FIGURE 40. EXAMPLES OF HERMITE POLYNOMIAL FITTING TO DATA

Numbers indicate the number of terms of the expansion used. For the "good" data of example (a), six terms gives a good fit; more introduces extraneous peaks. No satisfactory fit is achieved in the noisier data of example (b).

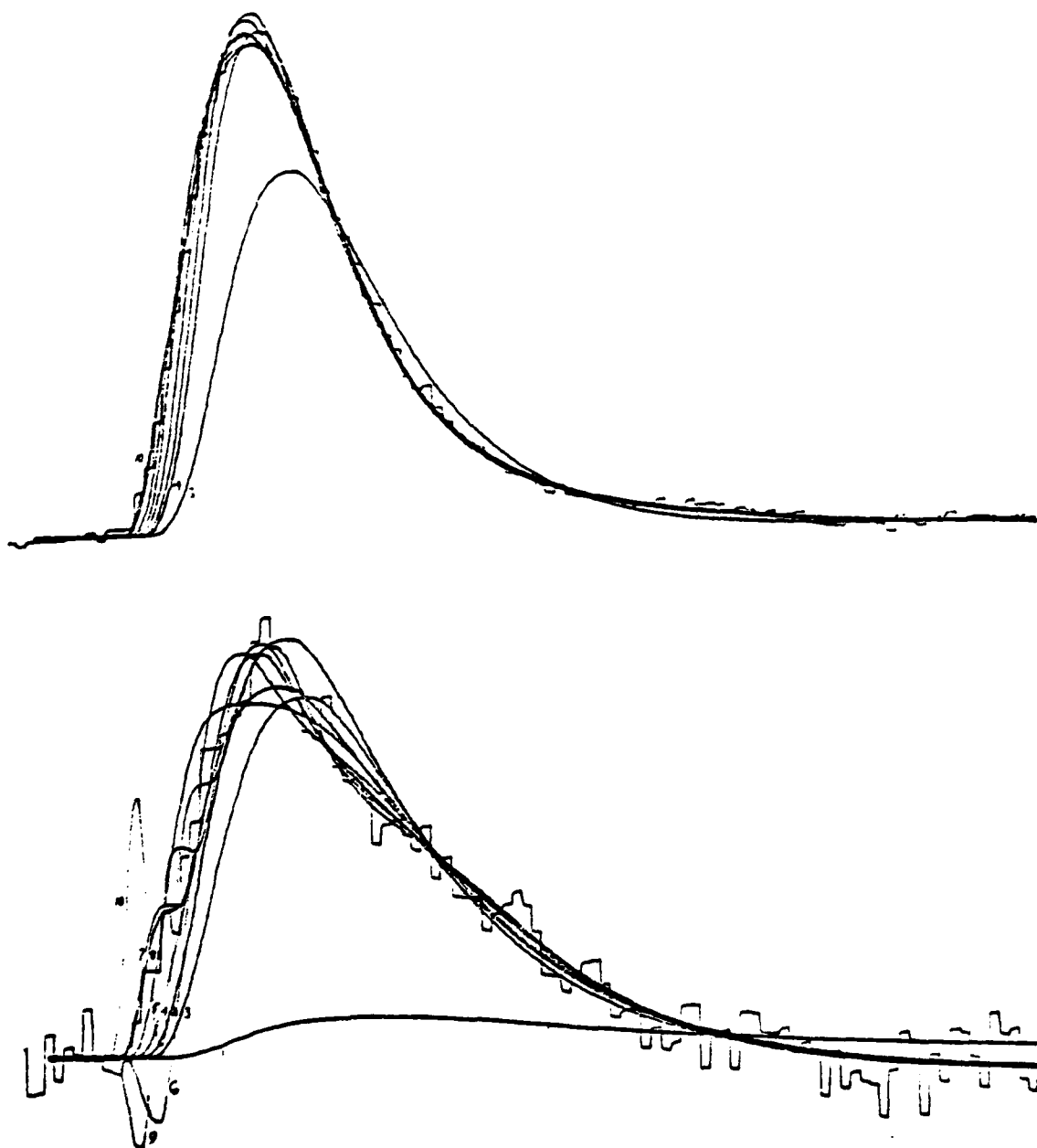


FIGURE 41. EXAMPLES OF MODIFIED GRAM POLYNOMIAL FITTING TO DATA

Numbers indicate the number of terms of the expansion used. For the "good" data of example (a), 10 terms give an excellent fit to the data. For noisier data (the same spectrum used in Figure 40b), 4 or 5 terms give a good fit. For 6 or more terms, there are again extraneous peaks.

## REFERENCES

Note: references to RGD are to Proceedings of the biennial Rarefied Gas Dynamic Symposia. Detailed information is as follows:

- RGD 9: Rarefied Gas Dynamics, R. Campargue, ed., Commissariat à l'Energie Atomique, Paris (1979)
- RGD 10: Rarefied Gas Dynamics, J.L. Potter, ed., AIAA, New York (1977).
- RGD 11: Rarefied Gas Dynamics, M. Becker & M. Fiebig, eds., DFVLR Press Porz Wahn, West Germany (1974)
- 1. Mason, B. J., Physics of Clouds, Clarendon Press, Oxford (1957).
- 2. Hobbs, P. V., Ice Physics, Clarendon Press, Oxford (1974).
- 3. Abraham, F. F., Homogeneous Nucleation Theory, Adv. Theor. Chem. Suppl. 1, Acad. Press, N.Y. (1974).
- 4. Springer, G. S., "Homogeneous Nucleation", Adv. in Heat Transfer V. 14 pp. 281-346 (1978).
- 5. A summary is given in Chapter VIII of Ref. 4 (pp. 305-312).
- 6. Plummer, P. L. M., and Hale, B. N., "Molecular Model for Prenucleation Water Clusters", J. Chem. Phys., 50:4329 (1972).
- 7. Trilling, L., "Mass Distribution of Droplets in Nucleation", RGD 11, p. 1281.
- 8. Gobbini, G., "A Contribution to the Statistical Mechanics of Homogeneous Nucleation", RGD 11, p. 1291; also "Homogeneous Nucleation of Liquifying or Sublimating Gases", S.M.Thesis, Dept. of Aeronautics and Astronautics, MIT, June, 1978.
- 9. Jones, T., "Homogeneous Vapor Droplet Distribution in the Atmosphere", S.M.Thesis, Dept. of Aeronautics and Astronautics, MIT, June, 1978.
- 10. Hale, B. N. and Plummer, P. L. M., "On Nucleation Phenomena I: A Molecular Model", J. Atm. Sci., 31:1615 (1974).
- 11. Larson, A. R. and Cantrell, C. D., "An Application of Non-Equilibrium Quantum Statistical Mechanics to Homogeneous Nucleation", RGD 11, p. 1267.
- 12. Zurek, W. H. and Schieve, W. C., "Clustering and Nucleation: A Molecular Dynamics Study", RGD 11, p. 1219.
- 13. Zurek, W. H., PhD Thesis, Univ. of Texas at Austin (1979).
- 14. McGinty, D. J., "Molecular Dynamics Studies of the Properties of Small Clusters of Argon Atoms", J. Chem. Phys., 58: 4733 (1973).

15. Abraham, F. F., "Monte Carlo Simulation of Physical Clusters of Water Molecules", J. Chem. Phys. 61: 1221 (1973).
16. Binder, K. and Stauffer, D., "Monte Carlo Study of the Surface Area of Liquid Droplets", J. Stat. Phys. 6: 49 (1972).
17. Binder, K., "Monte Carlo Simulation of Physical Clusters of Water Molecules", J. Chem. Phys. 63:2255 (1975).
18. Lee, J. K., Barker, J. A., and Abraham, F. F., "Theory and Monte Carlo Simulation of Physical Clusters in the Imperfect Vapor", J. Chem. Phys. 58: 3166 (1973).
19. Hale, B. N., Kiefer, J. "A Partition Function Model for Nucleation on Surfaces", J. Stat. Phys. 12: 437 (1975).
20. Plummer, P. L. M. and Stein, E. M., "Energetics of Water-Ice Surface Interactions: A Quantum Mechanical Study" Preprint Volume Int. Conf. on Cloud Physics, Boulder, Col., publ. Amer. Met. Soc. July, 1976.
21. Bentley, P. D. and Hands, B. A. "The Condensation of Atmospheric Gases on Cold Surfaces", Proc. R. Soc. Lond. A 359: 319 (1978).
22. Barger, M. J. and Levenson, L. L., "Molecular Beam Study of the Nucleation of Water on Gold", RGD 11, p. 1433.
23. Thanh, N. V. and Levenson, L. L., "Molecular Beam Study of the Nucleation of Water on Silver Iodide", J.Vac.Sci & Tech. 14: 471 (1977).
- 24.. Bryson, C.E. III and Levenson, L. L. "Critical Cluster Size Determination from Sticking Coefficient and Flash Desorption Measurements", Surf. Sci. 43: 29 (1974).
25. Lewis, B., "Physical Processes in Epitaxial Growth" (Review Paper) Thin Sol. Films 7:179 (1971).
26. Becker, E. W., et al (10 Authors) Institut für Kernverfahrenstechnik der Universität und des Kernforschungszentrums Karlsruhe report KFK 2016 (1974).
27. Takagi, T., Yamada, I., and Sasaki, A., "Ionized Cluster Beam Deposition", J. Vac. Sci. & Tech. 12: 1128 (1976).
28. RGD 9, RGD 10, RGD 11.
29. Bailey, A. B., "Cluster Intensity on Velocity Measurements in Condensed Flows", Arnold Eng. Dev. Center, Air Force Systems Command Report # AEDC-TR-74-38 (1974).

30. Dawson, D. B., Willson, E. J., Hill, P. G., Russell, K. C., "Nucleation of Supersaturated Vapors in Nozzles II:  $C_6H_6$ ,  $CHCl_3$ ,  $CCl_3F$ ,  $C_2H_5OH$ ", J. Chem. Phys. 51: 5389 (1969).
31. Lin, S.-S., "Quadrupole Mass Spectrometer for Direct Sampling of Atmospheric Gases and Condensation Products" Technical Report #AMMRC TR 73-9, Army Materials & Mechanics Research Center (1973).
32. Lin, S.-S., "Detection of Large Water Clusters by a Low rf Quadrupole Mass Filter", Rev. Sci. Instr. 44: 516 (1973).
33. Searcy, J. Q., and Fenn, J. B., "Clustering of Water on Hydrated Protons in a Supersonic Free Jet Expansion", J. Chem. Phys. 61: 12 (1974).
34. Friedman, L., Brookhaven National Labs, private communication (March, 1980).
35. Stein, G. D., and Armstrong, J. A. Jr., "Structure of Water and Carbon Dioxide Clusters Formed via Homogeneous Nucleation in Nozzle Beams", J. Chem. Phys. 58: 1999 (1973).
36. Armstrong, J. S. Jr., "An Investigation of the Physical Properties of Small Molecular Clusters Formed via Homogeneous Nucleation in Nozzle Beams", PhD Thesis, Mech. Eng. & Astronom. Sci. Dept., N.W. Univ. (1973).
37. Schwartz, P. "Structure des Microcristaux de Glace Formés par Nucleation Homogène dans une Detente en Jet Libre", Thèse (docteur de 3<sup>e</sup> cycle) L'Univ. de Paris VI (Physique)(1975).
38. Obert, W., "Properties of Cluster Beams Formed with Supersonic Nozzles" RGD 11, p. 1181.
39. Hagen, O. F. and Obert, W., "Cluster Formation in Expanding Supersonic Jets: Effects of Pressure, Temperature, Nozzle Size, and Test Gas", J. Chem. Phys. 56: 1733. (1972).
40. Dankert, C. and Koppenwallner, G., "An Experimental Study of Nitrogen Condensation in a Free Jet Expansion", RGD 11 p. 1107.
41. Moses, C. A. and Stein, G. D., "On the Growth of Steam Droplets Formed in a Laval Nozzle Using Both Static Pressure and Light Scattering Measurements", J. Fluid Eng., 100: 311 (1978).
42. Burghoff, H. and Gspann, J., "Bestimmung der mittleren Agglomeratgröße und des Restgasanteils kondensierter Molekularstrahlen durch Streuung eines K-Atomstrahls", Z. Naturforsch. A22: 684 (1967).
43. Gspann, J. and Kortig, K., "Cluster Beams of  $H_2$  and  $N_2$  Analyzed by Time-of-Flight Mass Spectrometry", J. Chem. Phys. 59: 4726 (1973).

44. Gspann, J. and Krieg, G., "Reflection of Clusters of He, H<sub>2</sub> and N<sub>2</sub> as Function of the Reflector Temperature", J. Chem. Phys. 61:2 4037 (1974).
45. Moran, J. P., "Experiments on Scattering of Monoenergetic Argon Beams by Heated Platinum", MIT Fluid Dyn. Res. Lab. Report #68-1 (1968), also PhD Thesis, Dept. of Aeronautics and Astronautics, MIT (1968).
46. Dreyfuss, D., "The Growth of Ice Crystals on Covellite Surfaces", S. B. Thesis, Dept. of Physics, MIT, 1975.
47. Selberg, L., "Report on Investigations of Ice Ih Crystal Growth", summer study, Fluid Dyn. Res. Lab., MIT, unpublished, 1976.
48. Lewis, G. V., "Scattering of a Helium Molecular Beam by Silicon", S.M. Thesis, Dept. of Aeronautics and Astronautics, MIT, (1971).
49. Bilgram J., Wenzl, H., Mair G., "Perfection of Zone-Refined Ice Single Crystals", J. Cryst. Growth 20:319 (1973).
50. Dreyfuss, D., unpublished (1977).
51. Knight, C. A., and Knight, N. C., "Negative Crystals in Ice: A Method for Growth", Science 150: 1819 (1965).
52. Dreyfuss, D., "Neutral Time-of-Flight Mass Spectrometry", S.M. Thesis, Dept. of Aeronautics and Astronautics, MIT,(1977).
53. Dreyfuss, D., Doak, R. B., and Wachman, H. Y., "Time-of-Flight Analysis by the Pseudorandom Chopping Technique: Calibration and Application to Mass Spectrometry", RGD 11, unpublished (1978).
54. Kaiser, J. F. and Reed, W. A., "Data Smoothing Using Low-Pass Digital Filters" Rev. Sci. Inst. 48: 1447 (1977).
55. UTI Model 100C Operating and Service Manual 1978.
56. Flaim, T. A. and Ownby, P. D. "Observations on Bayard-Alpert Ion Gauge Sensitivities to Various Gases", J. Vac. Sci. & Tech. 8: 661 (1971).
57. Biller, J., Biemann, K., Dept. of Chemistry, MIT, private communication March, 1980.
58. Van Wylen, G. J. and Sonntag, R. E. Fundamentals of Classical Thermodynamics, Wyley and Sons, Inc., N.Y. p. 683, (1976).
59. Kassner, J. L. Jr. and Hagen, D. E., "Comments on 'Clustering of Water on Hydrated Protons in a Supersonic Free Jet Expansion' " [Ref. 33 above] J. Chem. Phys. 64: 1860 (1976).

60. See chart on pp. 58-59 of Ref. 2 for summary of work on ice Ic.
61. Voronin, G. F., "Composition of Equilibrium Vapour of Antimony"  
Zh. Fiz. Khim. 37: 1616 (1963)., transl. in Russ. J. of Phys.  
Chem. (37: 869).
62. Hurst, J. E., Becker, C. A., Cowin, J. P., Janda, K. C., Wharton, L.,  
Auerbach, D. J., "Observation of Direct Inelastic Scattering in  
the Presence of Trapping-Desorption Scattering; Xe on Pt (111)"  
Phys. Rev. Lett. 43:1175 (1979).
63. Goodman, F. O., and Wachman, H. Y., Dynamics of Gas Surface Scattering  
Academic Press, N. Y. (1976).
64. Brusdeylins, G., Meyer, H.-D., Toennies, J. P. and Winkelmann, K.  
"Production of Helium Nozzle Beams with Very High Speed Ratios"  
RDG 10 p. 1047 (1977).
65. Beijerinck, H. C. W., Menger, P. and Verster, N. F., "Shape Analysis  
of Non-Maxwell Boltzmann Parallel Velocity Distributions in  
Supersonic Expansions of Noble Gases" RGD 11, p. 871.
66. Hildebrand, F. B., Introduction to Numerical Analysis, McGraw Hill,  
N. Y. p.290, (1956).



